
Phase-stabilized Ultrashort Laser Systems for Spectroscopy

Jens Rauschenberger



München 2007

Phase-stabilized Ultrashort Laser Systems for Spectroscopy

Jens Rauschenberger

Dissertation
an der Fakultät für Physik
der Ludwig-Maximilians-Universität
München

vorgelegt von
Jens Rauschenberger
aus Friedrichshafen

München, den 24.4.2007

Erstgutachter: Prof. Dr. F. Krausz
Zweitgutachter: Prof. Dr. T. W. Hänsch
Tag der mündlichen Prüfung: 11.7.2007

Contents

Zusammenfassung	VII
Abstract	VIII
1 Introduction	1
1.1 Time-resolved spectroscopy	3
1.2 Optical frequency metrology with frequency combs	5
2 Ultra-broadband oscillators	7
2.1 Few-cycle Kerr-lens mode-locked Ti:sapphire oscillator	10
2.2 Chirped mirror technology for dispersion control	17
2.3 The carrier-envelope phase of a mode-locked oscillator	21
2.3.1 Measurement of the frequency comb parameters	24
2.3.2 CE phase stabilization by difference frequency generation	28
2.3.3 Control of the frequency comb parameters	35
2.3.4 CE phase stability characterization	41
2.4 Long-cavity chirped-pulse oscillators	45
2.4.1 Double-pass post-amplifier	49
2.5 Conclusions	51
3 Few-cycle chirped-pulse amplifier systems	52
3.1 CE phase-stabilized chirped-pulse amplifier system	53
3.1.1 Origins of CE phase noise of amplified pulses	62
3.2 Conclusions	66
4 Femtosecond enhancement cavities	67
4.1 Passive optical resonators for femtosecond pulses	68
4.1.1 Dispersion control	72
4.1.2 Electronic feedback techniques	75
4.2 Vacuum enhancement cavity at 10 MHz repetition rate	81
4.3 Conclusions	87

5	Applications	89
5.1	Spectroscopy experiments with frequency combs	89
5.2	High-order harmonic generation	93
5.2.1	High harmonic generation from surfaces	96
5.2.2	High-order harmonic generation in an enhancement cavity ...	102
5.3	Above-threshold ionization	106
5.4	Conclusions	114
6	Outlook	115
A	Appendix	118
A.1	Origin of the frequency comb	118
A.2	Offset frequency dependence on group and phase velocity	119
	Bibliography	121
	Acknowledgements	132
	Curriculum Vitæ	133

Zusammenfassung

Die Erforschung der Wechselwirkung von Laserlicht und Materie erfordert laufend neue Technologien für immer kürzere Laserpulse, um atomare Prozesse in immer kleineren Dimensionen zeitaufgelöst und mit hoher Präzision verfolgen zu können. Solche Pulse bestehen meist nur noch aus einigen wenigen Zyklen des elektrischen Feldes. Daher spielt die Phase dieser Feldoszillationen mit kürzer werdender Pulsdauer eine immer größere Rolle. Ihre Stabilität liefert einen entscheidenden Beitrag für die Genauigkeit der Messung.

In dieser Arbeit werden mehrere Ultrakurzpuls-Laserquellen vorgestellt, die Pulse mit wenigen Zyklen und einem kontrollierten Verlauf des elektrischen Felds erzeugen. Zunächst wird eine Methode zur Phasenstabilisierung von Laseroszillatoren mit grosser Bandbreite diskutiert. Sie verbessert die Reproduzierbarkeit der Phase um eine Grössenordnung verglichen mit vorherigen Ansätzen.

Desweiteren wurde solch ein Oszillator in ein phasenstabilisiertes Verstärkersystem integriert. Die von diesem System erzeugten hochenergetischen phasenstabilisierten Laserpulse wurden in einer Reihe von Experimenten zur zeitaufgelösten Untersuchung von Starkfeldphänomenen eingesetzt. Beispielsweise wurde das laserinduzierte Tunneln von Elektronen aus einem Atom auf einer Zeitskala im Sub-Femtosekundenbereich beobachtet.

Eine weitere Messung, die nur durch einem kontrollierten Feldverlauf ermöglicht wurde, wird hier präsentiert: Einzelne Signaturen der elektrischen Feldhalbzyklen wurden im Spektrum von Photoelektronen identifiziert.

Die Frequenzkonversion von hochenergetischen Laserpulsen in hohe Harmonische ist ein gebräuchliches Verfahren, um kohärentes Licht im extremen ultravioletten (XUV) Spektralbereich zu erzeugen. Viele Anstrengungen wurden unternommen, um die niedrige Effizienz dieses nichtlinearen Prozesses zu steigern. Als ein potentiell möglicher Weg wird hier die Erzeugung hoher Harmonischer an einer Festkörperoberfläche anstatt in einem Gas untersucht.

Ein weiterer Ansatz ist die Plazierung des Gas-Targets in einem Überhöhungsresonator. Mit diesem Aufbau wurden Harmonische bis zur 15. Ordnung erzeugt. Abgesehen von einer gesteigerten Effizienz, kann auf diese Weise XUV-Strahlung mit der vollen Wiederholrate des treibenden Oszillators erzeugt werden, d.h. im Bereich einiger zehn bis hundert Megahertz. Hohe Wiederholraten ermöglichen die Verwendung des XUV-Lichts für die hochpräzise Vermessung optischer Frequenzen mittels der Frequenzkammtechnik. Hier wird ein Überhöhungsresonator beschrieben, der innerhalb des Resonators Pulsenergien von mehr als zehn Mikrojoule bei einer Wiederholrate von zehn Megahertz realisiert. Mit dieser hohen Durchschnittsleistung könnten bisher unerschlossene Frequenzen im XUV, wie z.B. der 1S-2S Übergang in einfach geladenem Helium um Größenordnungen genauer als bisher bestimmt werden.

Abstract

The investigation of laser-matter interactions calls for ever shorter pulses as new effects can thus be explored. With laser pulses consisting of only a few cycles of the electric field, the phase of these electric field oscillations becomes important for many applications.

In this thesis ultrafast laser sources are presented that provide few-cycle laser pulses with controlled evolution of the electric field waveform. Firstly, a technique for phase-stabilizing ultra-broadband oscillators is discussed. With a simple setup it improves the reproducibility of the phase by an order of magnitude compared to previously existing methods.

In a further step, such a phase-stabilized oscillator was integrated into a chirped-pulse amplifier. The preservation of phase-stability during amplification is ensured by secondary phase detection. The phase-stabilized intense laser pulses from this system were employed in a series of experiments that studied strong-field phenomena in a time-resolved manner. For instance, the laser-induced tunneling of electrons from atoms was studied on a sub-femtosecond timescale.

Additional evidence for the reproducibility of the electric field waveform of the laser pulses is presented here: individual signatures of the electric field half-cycles were found in photoelectron spectra from above-threshold ionization.

Frequency conversion of intense laser pulses by high-order harmonic generation is a common way of producing coherent light in the extreme ultraviolet (XUV) spectral region. Many attempts have been made to increase the low efficiency of this nonlinear process, e.g. by quasi phase-matching. Here, high-harmonic generation from solid surfaces under grazing incidence instead from a gas target is studied as higher efficiencies are expected in this configuration.

Another approach to increasing the efficiency of high-harmonic generation is the placing of the gas target in an enhancement resonator. Additionally, the production of XUV photons happens at the full repetition rate of the seeding laser, i.e. in the region of several tens to hundreds of megahertz. This high repetition rate enables the use of the XUV light for high-precision optical frequency metrology with the frequency comb technique. With such an arrangement, harmonics up to 15th order were produced. A build-up cavity that stacks femtosecond laser pulses in a coherent manner to produce intra-cavity pulse energies of more than ten microjoules at a repetition rate of ten megahertz is presented here.

With this high average power measuring hitherto uninvestigated optical transition frequencies in the XUV, such as the 1S-2S transition in singly charged helium ions may become a reality.

“La science, mon garçon, est faite d’erreurs,
mais d’erreurs qu’il est bon de commettre, car
elles mènent peu à peu à la vérité.”
(J. Verne, *Voyage au centre de la terre*)

Chapter 1

Introduction

Since its discovery, laser light has been used for the investigation of fundamental processes in matter. A plethora of light-matter interaction effects has been examined and exploited since then, from simple macroscopic ones to intricate microscopic ones. Prominent examples of the former are ablation, optical breakdown, and the formation of plasma, usually at the surface of a solid, or the alteration of the refractive index inside it. More complex effects can be studied when entering the microcosm. When atoms are exposed to laser light, the absorption of multiple photons may occur or valence electrons may be excited to Rydberg energy levels. With increasing laser intensity effects like field ionization and related phenomena such as non-sequential double ionization, above-threshold ionization, and the generation of high-order harmonics become important. Triggering these multiphoton processes demands laser intensities where the electric field strengths are comparable to the nuclear fields that bound the electrons to the ionic core. Over the last years, table-top systems have become available that can provide these peak intensities of typically 10^{13} to 10^{15} W/cm² with femtosecond laser pulses. These ultrashort pulses have the advantage of being able to steer the process in a controlled manner and even set off new effects that are not observable with longer pulses. For instance, a longer pulse will saturate the ionization yield well before the pulse maximum. In contrast, a pulse lasting only a few femtoseconds will reach the ionization threshold only close to its peak, thus the available intensities are fully exploited. This is due to the fact that these ultrashort pulses consist only of a few oscillations of the electric field, hence their name *few-cycle pulses*. At the frequently used wavelengths in the near-infrared, e.g. 800 nm for Ti:sapphire systems, one oscillation of the electric field lasts approximately 2.7 fs. Thus, sub-5 fs pulses at these wavelengths are less than two cycles long.

In contrast to the macroscopic effects, the laser-induced microscopic processes (e.g. above-threshold ionization) depend not only on the envelope of the pulse, but rather on the electric field underneath. However, the half-cycles of the electric field in an ultrashort pulse will fluctuate in position (and thus amplitude) from one pulse to the next in a pulse train due to environmental perturbations acting on the laser oscillator. These fluctuations can be characterized by the change of the phase between the pulse envelope peak and the global maximum of the electric field in this pulse, the *carrier-envelope phase* (CE phase). Hence, in order to fully control the multiphoton processes, intense laser pulses with stabilized electric field waveform are necessary. Over the last years, the joint efforts of the fields of laser stabilization and femtosecond lasers has resulted in the generation of few-cycle pulses with controlled evolution of the electric field.

The spectra of the ions, electrons, or photons generated by the aforementioned processes reveal insights to the properties of atoms and molecules. Yet, spectroscopy in its conventional form only provides information on the dynamics of fundamental phenomena on the atomic or molecular level after a-priori assumptions. In contrast, repeating the measurement over time results in a direct time-resolved observation of these rapidly evolving systems. Some fundamental aspects and experiments of *time-resolved spectroscopy* are introduced in chapter 1.1.

Femtosecond laser pulses can be employed for probing and manipulation of the dynamic evolution of a system on a sub-picosecond timescale. Changing the point of view from the time domain to the frequency domain, the global energy-level structure of an atomic system may be investigated with the broad spectral bandwidth associated with femtosecond laser pulses. Information on the separation of atomic energy levels or their fine-splitting is imprinted in the transition frequencies between them. Hence, high-precision measurements of optical transition frequencies can provide insights to the composition of matter, e.g. test the validity of predictions from quantum electrodynamics. Laser oscillators with a controlled CE phase have a spectrum that contains millions of narrow lines. These lines constitute the so-called *frequency comb*, a powerful tool for measurements of optical frequencies with high precision. The basic concept of *optical frequency metrology* with frequency combs is discussed in chapter 1.2.

During the course of this work several ultrafast laser sources for time-resolved spectroscopy and optical frequency metrology were conceptualized and constructed. The resultant publications are listed in refs. [1-7].

Three femtosecond oscillators were designed and/or set up, with varying purposes: as stand-alone system, for seeding a multi-pass amplifier system and as a front-end for a parametric amplifier. Chapters 2.1 and 2.2 present the details of these systems. Intertwined with the construction of the broadband oscillators was the development and implementation of a novel CE phase stabilization scheme which resulted in improved control over the frequency comb, verified by thorough characterization (see chapt. 2.3 and refs. [1, 2]).

One of the aforementioned phase-stabilized oscillators was integrated in a compact chirped pulse amplifier. Subsequently, a secondary phase-stabilization loop after the amplification stage was set up to obtain CE phase-stable amplified pulses (cf. chapt. 3.1 and ref. [3]) and a study on the effects from pulse picking in the amplifier on the CE phase was carried out (cf. chapt. 3.1.1 and ref. [4]).

Several phase-sensitive experiments were conducted with this amplifier system in the meantime. In the first, the electron localization in the laser-induced dissociation of

deuterium was studied [5]. With a technique similar to the previous setup, signatures of half-cycle cut-offs were observed in the spectra of photoelectrons from above-threshold ionization (see chapt. 5.3). In another experiment, the light-induced tunneling of electrons from atoms was studied on a sub-femtosecond timescale [6]. With a similar amplifier system, first experiments pertaining to the generation of high-order harmonics from surfaces were performed (cf. chapt. 5.2.1).

As a way to amplify femtosecond pulses at megahertz repetition rates, enhancement cavities (operating at 10 MHz and 1 GHz repetition rate) were designed and/or set up in close collaboration with the group of Prof. Hänsch (cf. chapt. 4.2). Conversion of intra-cavity light to the XUV region was demonstrated with a similar system, thus providing a frequency comb in this spectral region (cf. chapt. 5.2.2 and ref. [7]).

This thesis is structured as follows: the remainder of chapter 1 gives a brief introduction to the research fields motivating the construction of the laser sources. Chapters 2 through 4 present the different ultrafast laser systems, while chapter 5 discusses several applications of these sources.

1.1 Time-resolved spectroscopy

Studying processes inside an atomic or molecular system requires a ‘camera’ with a shutter speed much faster than the timescale of the processes under study. The briefness of the femtosecond laser pulses makes them an ideal tool for the investigation of light-induced processes in a time-resolved manner.

A concept for performing time-resolved spectroscopy is the *pump-probe configuration*. In this setup, a laser pulse (‘pump’) drives the atomic or molecular system to an excited state. A subsequent second pulse probes the temporal evolution of the system. Information on the evolution is extracted from the probe pulse or other products of the interaction, such as electrons or ions.

In this manner, the motion of atoms in molecules was observed and controlled. Laser pulses of ~ 100 fs duration were employed to study the breaking and forming of chemical bonds, i.e. the occurrence of chemical reactions, in real time. This laid the foundations of the research field femtochemistry, whose key proponent A. Zewail was awarded the Nobel Prize in chemistry in 1999 [8].

Penetrating deeper into matter, the time-resolved observation of electronic motion in atoms necessitates ever shorter pulses, as these processes occur on the timescale of a few femtoseconds down to attoseconds, with the atomic unit of time being 24 as.

With the optical period of near-infrared laser light being longer than a femtosecond and the fact that a pulse must contain at least one cycle, only a higher carrier frequency can reach these pulse durations. The nonlinear conversion of femtosecond laser pulses to the XUV spectral region by high-order harmonic generation can produce light bursts

that only last a few hundreds of attoseconds [9]. Due to the collinear and perfectly synchronized emission, the generated XUV pulses are together with the fundamental pulses ideal tools for pump-probe experiments. As high harmonic generation is driven by the periodic half-cycles of the fundamental pulse, a train of XUV pulses is emitted. If the CE phase of the pulses is controlled, it can be arranged that only a single half-cycle contributes to XUV photons at the maximum attainable energy and thus, with spectral filtering, a single attosecond pulse is produced [10]. In 2003, the unison of ultrafast laser science and frequency domain laser stabilization has enabled the generation of intense few-cycle pulses with a controlled electric field waveform [11] and hence isolated attosecond pulses. Employing these isolated attosecond pulses in a pump-probe experiment has recently enabled the observation of tunnel ionization dynamics in real time [6]. Laser-induced tunneling occurs near the peaks of the electric field in a pulse where the binding potential is temporarily suppressed. In the experiment, the attosecond XUV (pump) pulse excites atoms of a noble gas to a shake-up state, while the synchronized fundamental near-infrared (probe) pulse ionizes further to produce doubly-charged ions. When scanning the delay between the fundamental few-cycle pulse and the XUV pulse, it was found that tunneling depletes atomic bound states in sharp steps that last ~ 380 as.

The starting point for generating intense few-cycle pulses with uniform CE phase is a phase-stabilized laser oscillator. However, after the first demonstration of a method for the stabilization of the CE phase of a mode-locked laser in 1999 [12, 13] it was doubted that these nanojoule pulses could be amplified without corrupting the stability of the CE phase. The reasoning was that the amplification process (and the accompanying temporal stretching and compression) would introduce a large amount of phase noise. Nonetheless, with actively compensating for the phase noise introduced in the amplifier, the control over the CE phase could be preserved [14].

With these amplified phase-controlled few-cycle pulses, isolated pulses of 250 as duration were generated at photon energies of ~ 92 eV [15]. Also, 130 as pulses were produced at an energy of ~ 36 eV [16] with polarization gating. Access to a wide range of electronic dynamics in atomic core shells requires shorter and more energetic XUV/soft-X-ray pulses. As the frequency conversion by high-harmonic generation is a highly nonlinear process, it depends strongly on the peak amplitude of the half-cycles in the driving laser pulse. Consequently, CE phase jitter creates satellite pulses and introduces timing and amplitude jitter to the isolated attosecond pulse, diminishing its usefulness in pump-probe experiments. Therefore, new methods for increased control over the CE phase are still being explored to this day, for the phase-stabilization of laser oscillators [1, 17-20], as well as for amplifier systems [21-23].

The availability of intense few-cycle laser pulses whose CE phase is controlled with highest accuracy is one of the major preconditions for the generation of attosecond pulses with a duration approaching the atomic unit of time. A wealth of exciting experiments is made possible with these pulses. For instance, the observation of the quantum beating of the atomic wavepacket created by the superposition of the 1S and

2S state in atomic hydrogen with a time constant of ~ 400 as is appealing. Further, the delay between the emission of photoelectrons from valence and core states of a solid, estimated to be ~ 100 as could be probed [24]. Thirdly, the dynamics of the electron-electron correlation in the two-photon double ionization of helium could be studied with attosecond pulses in a coincidence experiment [25].

1.2 Optical frequency metrology with frequency combs

In the frequency domain, the spectrum of a pulse train from a mode-locked laser consists of a large number of evenly spaced narrow lines, the so-called *frequency comb*. This comb of modes has two degrees of freedom, the spacing between the comb lines and the position of the comb center, represented by the comb offset. Both fluctuate arbitrarily in a free-running system. Though if these two comb parameters are being stabilized, the perfectly equidistant comb lines may be utilized as a ‘ruler’ in frequency space. These can then be employed for the measurement of optical frequencies with high precision as the position of each comb line is known with high accuracy.

A measurement is only as precise as the employed definition of the physical units. Using an example of everyday life, a length measurement can only be accurate if an appropriately calibrated metering rule is utilized. As frequency is merely the inverse of time, high-precision frequency measurements need to take the definition of time into account. The second is internationally defined as the duration of exactly 9 192 631 770 periods of the radiation corresponding to two hyperfine levels of the ground state of cesium. A measurement of optical frequencies must thus be referenced to this time standard at ~ 9 GHz which leaves a frequency gap of approximately five orders of magnitude to be bridged. Frequency combs can serve this purpose and establish a phase-coherent link between the time reference in the rf region and the optical frequencies at hundreds of terahertz. The great improvement to optical frequency metrology associated with them was recognized by the Nobel Prize in physics in 2005 [26, 27]. Many measurements of transition frequencies of neutral atoms and ions have been performed in this way. A schematic overview of such an experiment is given in chapter 5.1. These measurements have allowed experimental investigation into various aspects of fundamental physics. The most striking examples may be the variation in time of fundamental constants such as the fine-structure constant [28-30] or the verification of quantum electrodynamics, e.g. through the frequency of the 1S-2S two-photon transition of hydrogen [31].

Control over the two comb parameters is of paramount importance for these applications. Yet, one of the parameters, the comb offset (the frequency domain embodiment of the CE phase) is difficult to observe and has long escaped measurement and control. Several years elapsed from the first ideas [32] to the first measurement [33] to the first demonstration of control [12, 13]. As mentioned in the

previous chapter, progress in stabilization methods is still ongoing. Increasing the degree of control over the offset frequency allows for improved measurements as smaller jitter equals narrower comb lines and thus can permit shorter averaging times for a desired level of measurement accuracy. Further, better long-term stability of the offset frequency can reduce slow drifts of the comb line positions and thus potentially increase the level of precision.

Extending the frequency comb technique to other spectral regions, e.g. the IR or the XUV is an attractive pursuit as hitherto unexplored transition lines can be measured with high precision. In contrast to the IR [34-36], no lasers exist that emit directly in the XUV region. Again, the nonlinear frequency conversion by high-order harmonic generation comes into play. However, the few-cycle pulses provided by standard laser amplifiers do not contain a usable comb structure due to the comb lines being too dense. As the comb line spacing is inversely proportional to the laser repetition period, a higher repetition rate (several megahertz) is needed to use the comb lines for spectroscopy. As a consequence, intense few-cycle pulses with high repetition rate are required. *Enhancement resonators* that coherently superpose laser pulses in a passive cavity have recently been shown to provide both [37, 7]. Several experiments have indicated that the comb structure survives the frequency conversion [38, 39]. A frequency comb in the XUV opens up new possibilities for spectroscopy of sharp resonances. As one of the exciting goals, the long series of hydrogen spectroscopic measurements could be perpetuated at higher energies. Helium ions are identical to hydrogen in their electronic structure, but carry a higher nuclear charge. Thus, on the one hand, the gross energy levels are at higher energies and more energetic photons are required to excite them. On the other hand, the corrections to the energy levels due to quantum electrodynamics scale as Z^4 (or even higher orders) with the nuclear charge Z and are therefore relatively stronger. For instance, probing the 1S-2S two-photon transition of singly-charged helium ions near 60 nm is a candidate from which a more stringent test of the validity of quantum electrodynamic predictions is expected.

Chapter 2

Ultra-broadband oscillators

Shortly after the invention of the laser in 1960 [40], the first ultrashort laser pulses were generated, already in the picosecond regime [41]. In those days, the race for ever shorter pulse widths began [42, 43]. Figure 1 shows the improvements in reported pulse duration over the last decades. Until the end of the 1980s, ultrashort laser pulses were mainly generated by dye lasers, where a record of 6 fs was achieved in 1987 [44]. Ti:sapphire lasers quickly reached and surpassed this landmark and as a consequence became the preferred devices for ultrashort laser pulse generation. Nowadays, 5 fs pulses that can be compressed externally down to 2.8 fs have been achieved [45-48].

Two different modes of pulsed laser operation have to be distinguished: *Q-switching* and *mode-locking*. Q-switching is based on a variable attenuator (e.g. an acousto-optic modulator) inside the cavity that switches from high cavity loss (low Q) to low cavity loss (high Q) after population inversion is created in the gain medium, thereby forming an intense laser pulse [49]. Compared to mode-locking, Q-switching generally results in lower repetition frequencies, higher pulse energies and longer pulse durations (typically nanoseconds). Furthermore, there is no phase correlation between subsequent pulses.

The mode-locking process on the other hand generates ultrashort pulses by establishing a fixed phase relationship between all of the lasing longitudinal modes (fig. 2a). It requires the introduction of an advantage for short-pulse operation over cw¹ operation of the laser. For passive mode-locking in its simplest form, this can be the saturation behavior of a dye or a semiconductor material [50]. A saturable absorber displays a reduced absorption for high intensities compared to low intensities. Thus, a short pulse produces a loss modulation because the high intensity at the peak of the pulse saturates the absorber more strongly than its low intensity wings. In effect, the circulating pulse saturates the laser gain to a level that is just sufficient to compensate for the losses from the pulse itself, while any other circulating low-intensity light experiences more loss than gain and thus dies out during the ensuing cavity round-trips. Hence, *self-amplitude modulation* of the light inside the cavity occurs. Figure 2b shows the (passive) mode-locking process schematically.

Ideally, mode-locking starts from normal noise fluctuations in the laser, however usually an external perturbation to increase laser noise by mechanical ‘shaking’ of an optical component (e.g. a cavity end mirror) is necessary.

¹ cw: continuous wave.

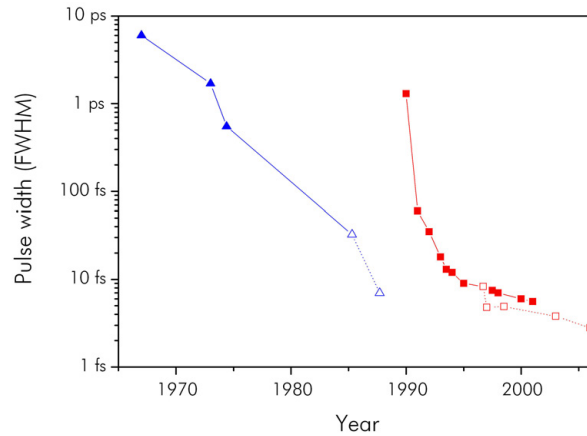


Figure 1. Improvements in ultrashort pulse generation since the first demonstration of a laser in 1960. Until the end of the 1980s, ultrashort pulse generation was dominated by dye lasers, and pulses as short as 27 fs were achieved. External pulse compression ultimately resulted in pulses as short as 6 fs. Today, Ti:sapphire lasers can generate pulses with only two optical cycles at FWHM². External compression resulted in pulses as short as 2.8 fs. Triangles (squares) denote results from dye (Ti:sapphire) lasers. The filled symbols indicate results directly achieved from a laser; open symbols indicate results achieved with additional external pulse compression.

Mode-locking produces a stable train of ultrashort pulses, though under certain conditions (e.g. high intra-cavity pulse energy), Q-switching instabilities can lead to Q-switched mode-locking, resulting in an unwanted amplitude modulation of the pulse train.

These days, mode-locking in Ti:sapphire lasers is typically accomplished by *Kerr-lens mode-locking* [51, 52]. It makes use of the intensity dependence of the index of refraction $n = n_2 I(r,t)$, where n_2 is the nonlinear refractive index and $I(r,t)$ the radial- and time-dependent intensity of a short-pulsed laser beam. By placing a Kerr-active material (e.g. the gain medium) at an intra-cavity focus, this results in a Kerr lens that is strongest at the pulse intensity peak. In combination with an aperture inside the cavity, this forms an effective saturable absorber (fig. 3). Usually, a soft aperture configuration is employed, where the reduced mode area in the gain medium improves the overlap with the pump beam and therefore the effective gain.

Currently, Kerr-lens mode-locked Ti:sapphire lasers are producing the shortest few-cycle pulses, consisting of less than two cycles at FWHM at the central wavelength of approximately 800 nm. In order to support such ultrashort pulse widths, obviously a very large spectral bandwidth is necessary.

² FWHM: full width at half maximum.

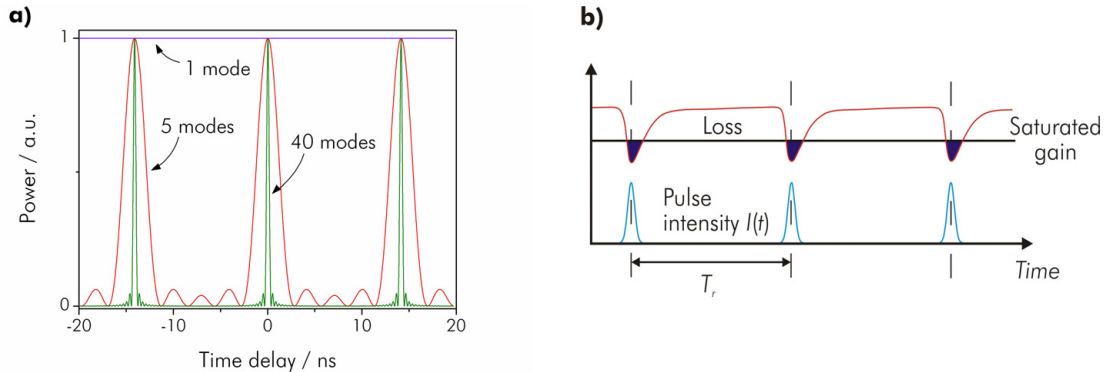


Figure 2. (a) Schematic of the pulse train being generated by phase-locking the simultaneously oscillating cavity modes. The forming pulse train is shown with 1, 5, and 40 modes contributing. The mode spacing is $1/T_r = 70$ MHz. (b) Principle of passive mode-locking. A saturable absorber is used to obtain self-amplitude modulation of the cavity light. The absorber losses are high for low intensities, but significantly smaller for the high intensities in a short pulse. Hence, a short laser pulse produces a loss modulation with rapid initial loss saturation and a slower recovery, depending on the actual absorber mechanism. The circulating pulse saturates the laser gain so that it just compensates for the losses from the pulse itself. Any other low-intensity light experiences more loss than gain and dies out accordingly.

A constantly widening range of applications in science and industry makes use of femtosecond pulses from Kerr-lens mode-locked Ti:sapphire lasers. A few exemplary areas shall be mentioned here:

In medical applications, ultrashort laser pulses have been used to improve surgical cutting precision, particularly in corneal surgery [53] and brain tumor removal [54]. Using femtosecond pulses reduces secondary damage effects, such as shock waves and cavitation bubbles in tissues [55], as the fluence threshold for optical breakdown decreases with pulse duration.

Telecom applications are mainly the focus when femtosecond pulses are used for the fabrication of optical waveguides and other optical elements, such as splitters, couplers or Mach-Zehnder-interferometers [56, 57]. This micromachining process in fused silica holds the promise of manufacturing truly 3-dimensional integrated photonics elements.

The broad spectral bandwidth associated with ultrashort laser pulses is put to use in optical coherence tomography, a non-invasive interferometric tomographic imaging technique [58]. Having found widespread dissemination in ophthalmology and other biomedical applications, it offers sub-micrometer resolution combined with penetration depths of a few millimeters in tissue. The general scheme is a Michelson-type interferometer with a scanning sample and a reference arm. The short coherence length of the broadband spectrum effects the high spatial resolution, as light outside the coherence length will not interfere.

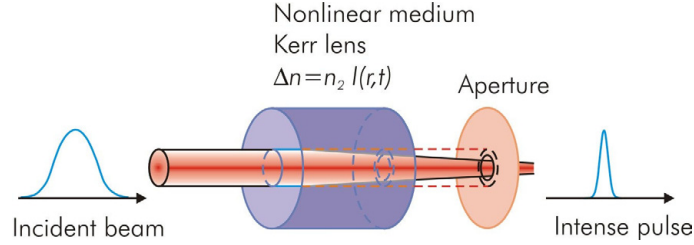


Figure 3. Principle of Kerr-lens mode-locking. A Kerr lens is obtained at the focus in the gain material, where the refractive index increases with the incident intensity $I(t)$ by means of the nonlinear refractive index n_2 . The aperture that effectively forms the fast saturable absorber is commonly implemented as a soft aperture, where the reduced mode area in the gain medium improves the overlap with the focused pump beam, and therefore the effective gain, for the peak of the pulse.

Furthermore, ultrashort oscillators are also employed as seed lasers for laser amplifier systems of all kinds. Two options for amplification of few-cycle pulses are presented in chapters 3 and 4. Ultrashort amplified pulses find application in a variety of areas, of which two are discussed in chapter 5.

2.1 Few-cycle Kerr-lens mode-locked Ti:sapphire oscillator

In this chapter the general setup and the peculiarities of a broadband Kerr-lens mode-locked Ti:sapphire oscillator will be presented.

The Ti:sapphire oscillator consists of a linear cavity in an X-folded geometry [59], as shown in figure 4. One of the end mirrors (OC in fig. 4) of this cavity is used to couple out a fraction of the intra-cavity light. The Ti:sapphire crystal ($\text{Ti:Al}_2\text{O}_3$) is optically pumped at 532 nm by a frequency-doubled Nd:YVO₄ laser. The pump light is focused by a lens to create efficient population inversion in the crystal. In order to reduce Fresnel reflection losses from its surfaces, the crystal is cut and positioned at Brewster angle. The ensuing astigmatism of the infrared laser beam may be compensated by a suitably-chosen angle of the mirrors used for focusing into the crystal (M3 and M4 in fig. 4). The astigmatism is balanced for

$$\frac{\sin^2(\theta)}{\cos(\theta)} = \frac{t}{f} \frac{\sqrt{n^4 - 1} \sqrt{n^2 - 1}}{n^4}, \quad \text{Eq. 1}$$

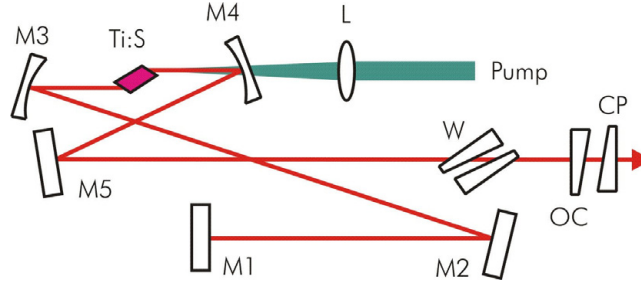


Figure 4. The schematic of the prism-less Ti:sapphire laser. Pump: frequency-doubled diode-pumped Nd:YVO₄ laser at 532 nm (Verdi, Coherent Inc.); CP: fused silica compensating plate; L: incoupling lens; M1–5: chirped mirrors; M3, M4: 50 mm ROC³ folding mirrors; OC: output coupler; Ti:S: Ti:sapphire (Ti:Al₂O₃) crystal; W: fused silica wedged plate

where $n = 1.76$ is the refractive index of sapphire at 800 nm wavelength, f the focal length of mirrors M3 and M4, θ the folding angle and t the thickness of the crystal [60].

However, in practice it is found that a slight detuning of the folding angles to smaller values results in better spatial mode quality and easier initial mode-locking, whereas adjusting the angle to marginally larger values increases the output power and vice versa.

The distance between focusing mirrors M3 and M4 has to be close to $2f + \delta$, where δ is the stability parameter. The range of values of δ for which the resonator is stable is divided in two separate regions (stability zones). Kerr-lens mode-locking occurs at the border of one of the stability zones. The width of the gap between them depends on the cavity asymmetry

$$\gamma = \frac{d_2 - f}{d_1 - f}, \quad \text{Eq. 2}$$

where d_1 and d_2 are the length of the long (mirrors M4 – OC) and short (M1 – M3) cavity arm, respectively. Larger γ represents a larger gap between the zones. Empirically, it was found that a cavity asymmetry of $\gamma \approx 2$, i.e. a length ratio of the cavity arms of around 2:1 provides the best conditions for mode-locking operation.

Apart from the gain bandwidth of the Ti:sapphire crystal and the reflectance bandwidth of the cavity mirrors, the generation of the broadband spectrum necessary for ultrashort pulses is limited by dispersion inside the cavity. Dispersion, i.e. a wavelength-dependent index of refraction $n(\lambda)$ shifts the longitudinal cavity modes from their equally spaced pattern in the frequency domain. This prevents the

³ ROC: radius of curvature. The ROC corresponds to twice the focal length.

mode-locking process from forming an ultrashort pulse. However, if a steady state pulsed operation exists, the pulse looks the same after each round-trip. This effectively dispersion-free propagation is enabled by a delicate interplay between the positive dispersion from the optical elements and several nonlinearities. The dominant nonlinearities in a Kerr-lens mode-locked oscillator are the gain of the laser medium, self-phase modulation and self-amplitude modulation. This balance between the pulse-lengthening effect of the dispersion and the nonlinearities ultimately limits the pulse duration. The pulse formed in the cavity under these circumstances is called a *dispersion-managed soliton*. The theoretical model predicts Gaussian or super-Gaussian spectral shapes [61], in contrast to secant hyperbolic for pure solitonic propagation. However, measured spectra of ultrashort pulses exhibit complex multi-peaked structures, caused by small imperfections in dispersion compensation.

Intra-cavity dispersion compensation can be achieved either by *chirped mirrors* or a prism compressor, providing negative group delay dispersion. Design considerations and other aspects of chirped mirrors are presented in detail in chapter 2.2. A prism setup that provides negative second order dispersion is shown in figure 5 [62]. A first prism disperses the beam spectrally. The second prism makes the different colors propagate collinearly. A retroreflector reverses the spatial dispersion. However, the red part of the spectrum travels a longer optical path length compared to the blue part, thus negative dispersion is realized. Prism-based dispersion compensation has the disadvantage of being highly sensitive to cavity alignment, but with the advantage of being continuously tunable in contrast to all-chirped-mirror-based systems. Furthermore, the prism setup introduces large negative third-order dispersion that unfavorably affects the pulse duration. Even with Brewster-cut prisms, a prism compressor has considerably higher overall losses than a set of chirped mirrors.

Ti:sapphire has an extremely large gain bandwidth of more than 300 nm. The Fourier transform of this spectrum already yields sub 4-fs pulse duration. Yet, additional frequency components can be generated inside the cavity by means of *self-phase modulation* (SPM), which is merely a time-domain manifestation of the Kerr effect.

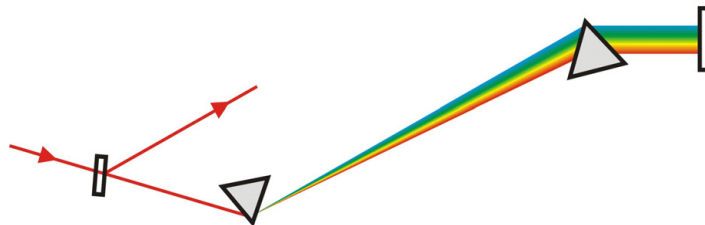


Figure 5. Sketch of a prism compressor. This setup introduces negative dispersion, as the longer wavelength components travel a longer distance in the second prism. However the magnitude and sign of the second-order dispersion is strongly dependent on the geometry.

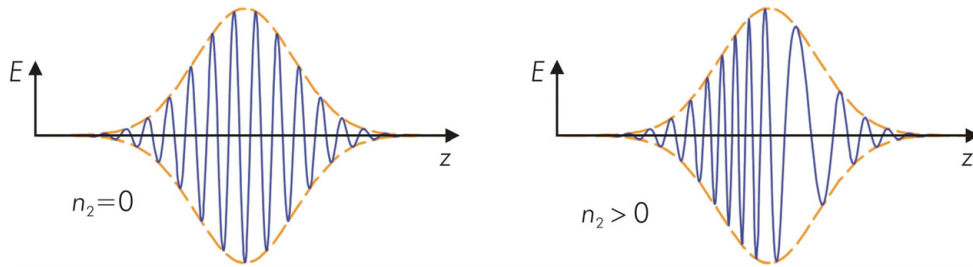


Figure 6. The longitudinal Kerr effect modulates the refractive index depending on the laser pulse intensity due to the nonlinear part of the refractive index n_2 . For $n_2 > 0$ it delays the central part of the pulse with respect to the lower-intensity wings. This causes a red shift in the leading part and a blue shift in the trailing part of the pulse.

While the spectral bandwidth sets the lower attainable limit on the pulse duration, the actual pulse duration also depends on the spectral phase of the pulse. With appropriate compensation of the arising phase distortions, this can result in shorter pulse duration. SPM applies a phase modulation, due to the nonlinear contribution of n_2 to the refractive index, to the pulse with an amplitude proportional to the peak power of the pulse. This causes, for $n_2 > 0$, a red shift at the leading edge and a blue shift at the trailing edge (fig. 6). This generates new spectral components, even outside the gain region of Ti:sapphire, leading to an overall spectral broadening of the pulse. The nonlinearity of either a sapphire plate in a tight secondary cavity focus [45] or of the Ti:sapphire gain medium itself can provide the SPM.

In this manner, several ultra-broadband oscillators spanning more than one octave⁴ were demonstrated [45, 63-66].

Self-phase modulation, along with the Kerr-lens effect and dispersive cavity elements, can bring about several problems in broadband laser oscillators. Firstly, the generated pulses may have a very complicated spectral structure, with strong distortions [45, 67]. These pulses are not easily compressed, external to the cavity, e. g. by a prism compressor. The smoothness of the spectrum is also of concern for applications such as optical coherence tomography, as spectral structures would compromise the image quality through artifacts.

Furthermore, no simple analytical function can be used to model these pulses, therefore their autocorrelation measurement becomes challenging and other methods such as spectral interferometry for direct electric field reconstruction [68] or frequency-resolved optical gating [69] have to be employed.

Additionally, strong SPM action in the laser cavity has the drawback of generating a spectrally-dependent spatial output mode profile, as different spectral components experience a different amount of phase modulation [70, 71]. For the modes that are

⁴ An octave is the interval between a certain frequency and double its frequency.

resonant in the cavity, i.e. that are within the reflectivity bandwidth of the mirrors, the cavity geometry determines the waist size and divergence at the output coupler. Gaussian beam propagation theory predicts a spot size dependence $w \sim \lambda^{1/2}$ (ref. [70]). The beam characteristics of the non-resonant modes, however, can be directly influenced by the Kerr-lensing in the crystal without the self-correcting effects of the cavity.

Several Ti:sapphire all-chirped-mirror laser oscillators were constructed in the course of this work, mainly with the purpose of seeding multi-pass or parametric amplifier systems (see chapt. 3). Requirements due to synchronization to the amplifier pump laser (for the parametric amplifier) or simply space constraints determined the repetition frequency to be in the region between 70 and 80 MHz. The energy of the generated pulses is approximately 5 nJ, with a pump power of 5 to 6 W from a frequency-doubled Nd:YVO₄ laser (Verdi V6, Coherent Inc.). This depends on the losses from the mirrors, i.e. quality of the mirror coating. The thickness of the Ti:sapphire crystal is $t = 2.6$ mm and its absorption coefficient $\alpha = 5.0$ cm⁻¹ at 532 nm. The radius of curvature of the concave mirrors (M3 and M4 in fig. 4) is $r = -50$ mm. The transmission of the output coupler is 13%. Specifically designed negatively chirped mirrors (Leybold Optics GmbH) are used to control the cavity dispersion (see chapter 2.2). A pair of thin fused-silica wedges is inserted at Brewster angle for fine-tuning the intra-cavity dispersion.

The spatial profile of the generated beam is approximately Gaussian, however due to the ultra-broad spectrum, the spatial mode profile is spectrally-dependent, as mentioned above. Figure 7 shows the spectral variations in the tangential and sagittal spot size, measured in the far-field 3.75 m from the output coupler.

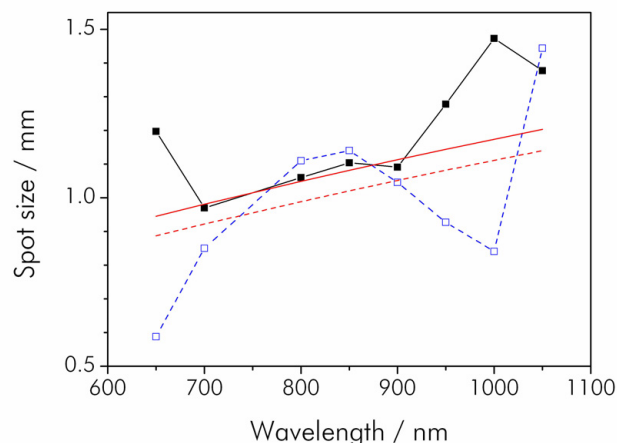


Figure 7. Measured beam spot sizes in the far-field 3.75 m from the output coupler as a function of wavelength. Filled (empty) squares denotes tangential (sagittal) plane. The solid and dashed lines are respective fits to the expected $\lambda^{1/2}$ diffraction limit divergence in the region of 700 to 900 nm.

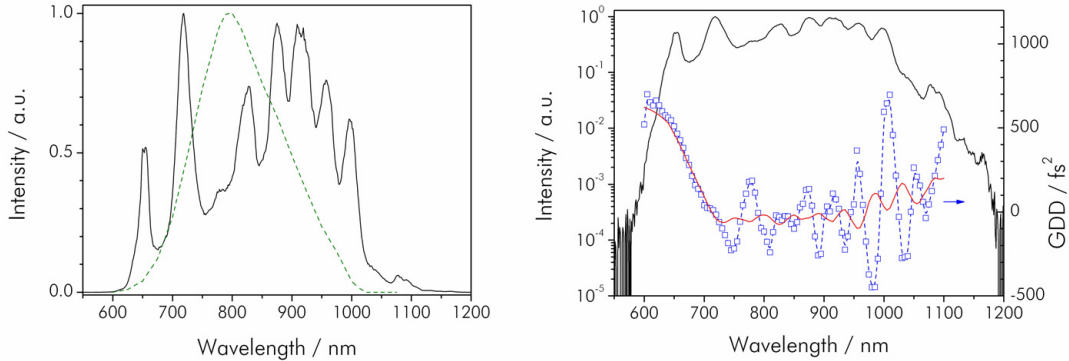


Figure 8. Spectrum from the oscillator measured with an optical spectrum analyzer (AQ-6315A, Ando Corp.). **(a)** shows the spectrum on a linear scale, including the gain profile of Ti:sapphire. **(b)** shows the spectrum on a logarithmic scale, including the sum of GDD contributions in the cavity (3.8 m of air, 2.6 mm of Ti:sapphire, a pair of thin glass wedges, 5 reflections off chirped mirrors (Leybold Optics GmbH)) and a 75 nm adjacent averaging (red solid line).

A typical oscillator spectrum is shown in figure 8 together with the net cavity dispersion. Although the gain bandwidth of the Ti:sapphire crystal extends only from 670 – 980 nm (at -10 dB below the maximum), the generated spectrum from the oscillator extends beyond this region. This means that most of the light at the wings of the spectrum is not generated through lasing but by self-phase modulation in the crystal, a phenomenon previously observed [64, 67].

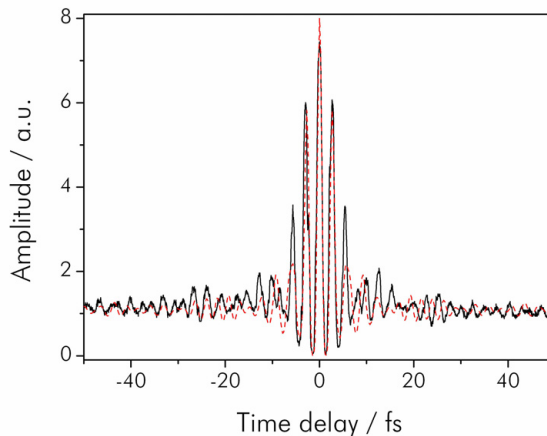


Figure 9. Interferometric autocorrelation of the oscillator pulses, measured with an autocorrelator designed for femtosecond pulses (Femtometer, Femtolasers GmbH). The frequency-doubling crystal used is a 10- μm -thick $\beta\text{-BaB}_2\text{O}_4$ (BBO) crystal. The FWHM pulse duration is 6.2 fs. The dashed line shows the transform-limited pulse as derived from the spectrum in fig. 8 with a FWHM width of 4.7 fs.

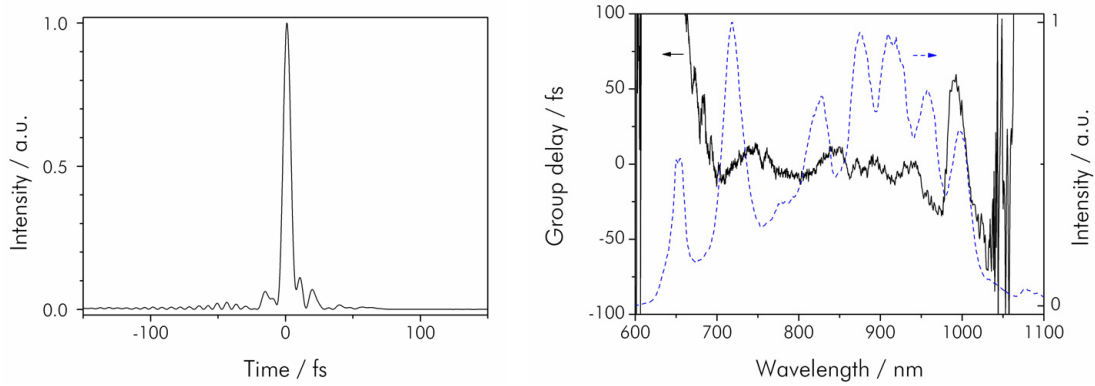


Figure 10. Pulse characterization by spectral phase interferometry for direct electric-field reconstruction (SPIDER). The SPIDER spectrum is recorded by a spectrograph (MS125, Oriel Instruments Corp.), employing a cooled CCD camera (DV420 OE, Andor Technology plc). **(a)** shows the temporal profile of the pulse. The FWHM of the intensity envelope is estimated as 6.3 fs, in accordance with the result of the interferometric autocorrelation (fig. 9). **(b)** shows the group delay and spectrum.

The spectrum spans one octave at about -30 dB below the average power level in the 800 nm spectral region.

The sharp roll-off at the short wavelength end and the strong modulation in the long wavelength region clearly do not conform to the theoretical Gaussian spectrum for soliton-like pulses. This is due to imperfect intra-cavity dispersion compensation, especially for higher-order dispersion.

After extra-cavity pulse compression by multiple reflections off of a pair of chirped mirrors (compensating the output coupler's material dispersion), the temporal characteristics of the output pulses are measured using an interferometric autocorrelator designed for ultrashort pulse diagnostics. Figure 9 shows the measured interferometric autocorrelation trace. The FWHM of the pulse intensity envelope has been evaluated as 6.2 fs.

However, as the autocorrelation technique fails to provide reliable data in the sub-10-fs regime due to the ambiguity in temporal pulse shape, pulse characterization by spectral phase interferometry for direct electric-field reconstruction (SPIDER) [68] was conducted. Temporal profile, retrieved phase and group delay are shown in figure 10. The FWHM of the intensity envelope in the time domain is estimated as 6.3 fs, in accordance with the result of the interferometric autocorrelation.

As is evident from figure 10, satellite pulses are present. However, only a fraction of 14% of the pulse energy is located in these leading and trailing pulses.

Deviation from the ideal case of the transform-limited pulse is mainly attributed to residual cubic dispersion of the cavity dispersion (see also next chapter) at short wavelengths. Its suppression with an improved mirror design will reduce the fractional energy of satellite pulses and compress the main pulse.

2.2 Chirped mirror technology for dispersion control

Chirped mirrors constitute a vital ingredient of broadband oscillators as the key tool for intra-cavity dispersion management. They are also employed for the same reason in enhancement resonators (see chapter 4). Moreover, they are employed in laser amplifiers for third-order dispersion compensation and for pulse compression external to a cavity (cf. chapter 3).

Chirped mirrors were first demonstrated in 1994 [72] and since then have enabled the generation of more and more broadband spectra and hence, shorter pulses. They can compensate the material dispersion of the crystal and other optical elements inside the laser cavity to yield a net slightly negative dispersion. The balance between negative dispersion and nonlinearities such as the Kerr effect shapes a soliton pulse inside the broadband resonator. Therefore, chirped mirrors that provide precise control over the cavity *group delay dispersion* (GDD) over a wide spectral range, combined with high reflectivity, are mandatory.

Just like all other dielectric mirrors, chirped mirrors are made up of many layers, sometimes up to 70, of alternating high-index and low-index coating materials. Available coating materials are Nb_2O_5 , TiO_2 , Ta_2O_5 , and HfO_2 , combined with SiO_2 ($n = 1.48$ at 500 nm). Nb_2O_5 is a high-refractive-index material ($n = 2.35$ at 500 nm) that was found to support the broadest spectra.

If the optical thickness of all layers is chosen equal to $\lambda_B/4$, interference of all Fresnel reflections generated by the index discontinuity at the layer interfaces will constructively add up for the Bragg wavelength λ_B . Varying the optical layer thickness along the mirror structure during deposition then results in a dependence of Bragg wavelength λ_B on penetration depth z , as shown in figure 11. Chirping the mirror structure therefore allows for the generation of any desired group delay for a specific wavelength. It is obvious that the Bragg wavelength does not have to be varied linearly with penetration depth, but any single-valued function can be used as the chirp law $\lambda_B(z)$. In principle, this enables the compensation for material second-order dispersion together with arbitrary higher-order dispersion contributions. The physical layer thicknesses are optimized by means of a genetic algorithm to match a pre-defined GDD target curve.

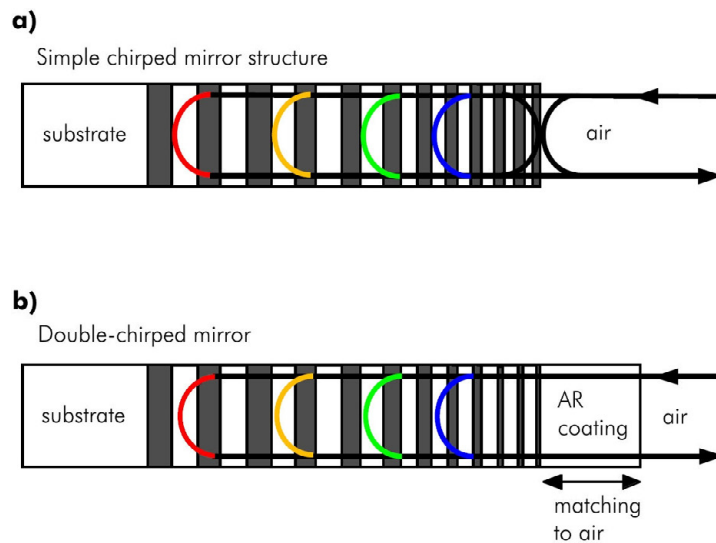


Figure 11. Chirped mirror structure schematic. **(a)** Simple chirped mirror structure. The desired effect of a wavelength-dependent penetration depth is accompanied by strong interference effects, mainly from a spurious reflection at the interface to the ambient medium. **(b)** Double-chirped mirrors provide impedance matching with an additional antireflection (AR) coating on top of the mirror stack and by a duty-cycle modulation inside the mirror stack.

Layer thicknesses of down to 5 nm occur, which makes production of these mirrors close to the design very challenging as the GDD is highly sensitive to small thickness deviations. Most of the chirped mirrors used in the presented broadband oscillators were manufactured with a magnetron sputtering machine (Helios, Leybold Optics GmbH) [73].

Usually, broadband chirped mirrors have pronounced GDD oscillations in the longer wavelength region, as they effectively constitute a Gires-Tournois interferometer. The combination of the highly reflecting chirped mirror stack and an unwanted reflection, e.g. at the interface between coating stack and ambient medium forms this interferometer. Anti-reflection coating on top of the chirped mirror stack provides only partial remedy to the problem, due to the high requirement on the transmittivity of the anti-reflection coating. These GDD fluctuations can broaden the pulse and lead to energy transfer from the initial pulse to satellite pulses. The amplitude of these ripples determines the amount of energy transferred. In order to compensate for these inevitable ripples and to obtain a smooth net dispersion curve, broadband chirped mirrors are typically used in complementary pairs (fig. 12), such that the dispersion oscillations cancel each other. As the angle of incidence shifts the GDD curve in wavelength and as manufacturing imperfections occur, this approach cannot presently avoid GDD oscillations completely.

Progress in mirror design, manufacturing and characterization over the last years has resulted in chirped mirrors with controlled dispersion (residual GDD fluctuations less than 100 fs^2) and reflectivity (higher than 94%) in the wavelength range of 450 to 1200 nm, corresponding to a bandwidth of 1.3 octaves [73]. These broadband mirrors were characterized with a white-light interferometer [74]. Future use of a cavity-based method [75, 76] will result in more accurate estimates for GDD and reflectivity and potentially better mirror designs.

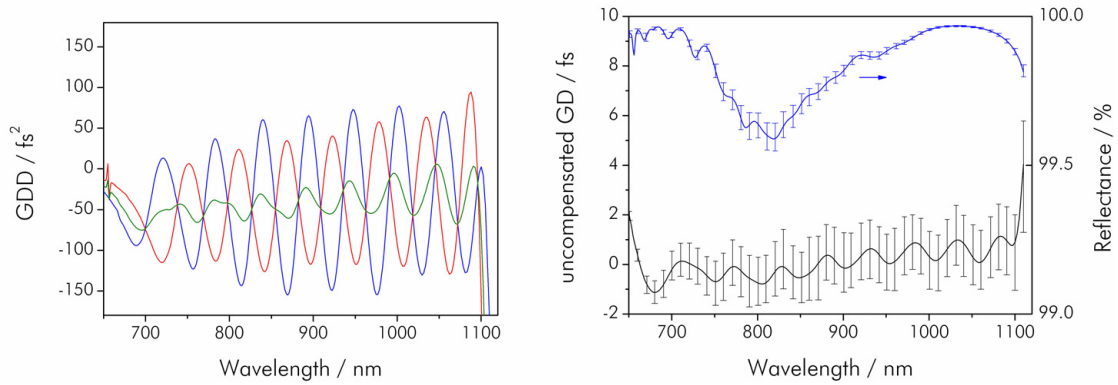


Figure 12. Calculated GDD of a broadband chirped mirror pair. **(a)** Red and blue lines refer to the GDD of the respective mirrors; the green curve shows the average of both. Increasing GDD oscillations in the long wavelength region are clearly visible. The mirrors consist of a stack of 65 alternating layers of SiO_2 and Nb_2O_5 . **(b)** shows the average mirror reflectivity and the uncompensated group delay in a sample linear cavity consisting of three chirped mirror pairs, 2.6 mm of Ti:sapphire, a pair of fused silica wedges, and $\sim 4 \text{ m}$ of air.

Despite these achievements in controlling the GDD, it was found that also higher-order dispersion (third order dispersion, etc.) plays a critical role, and may actually be even more important for the generation of smooth output spectra with minimal spectral fluctuations than a full suppression of GDD fluctuations [67].

The required negative GDD for an ideal dispersion-managed soliton can be derived from [77]

$$D = \frac{dT_g}{d\omega} = -\delta P_{peak} \left(\frac{\tau_{FWHM}}{1.76} \right)^2, \quad \text{Eq. 3}$$

where P_{peak} is the peak power of the soliton, τ_{FWHM} the pulse width (full width at half maximum) and δ the SPM coefficient,

$$\delta = \frac{4 n_2 t}{\lambda w^2}, \quad \text{Eq. 4}$$

where n_2 is the nonlinear index of refraction of the crystal, t its thickness, λ the center wavelength, and w the focus radius inside the crystal [78]. For a typical SPM coefficient on the order of 0.9 rad/MW, an intra-cavity peak power of approximately 7 MW and a pulse width of around 6 fs, this yields a required GDD of $D \sim -75 \text{ fs}^2$.

For the optimum Kerr-lensing in the crystal and therefore the shortest pulses, it was found that an approximately equal distribution of the GDD in both cavity arms is beneficial (fig. 13). Assuming perfect dispersion compensation for the moment, equal GDD distribution results in a transform-limited pulse in the center of the gain crystal and at the resonator end mirrors. This yields the highest peak intensity in the crystal, thus the strongest self-phase modulation, the broadest spectrum and therefore the shortest pulses.

Experimentally, it has been observed that a minimum in the GDD curve at around 795 nm facilitates starting the mode-locking process.

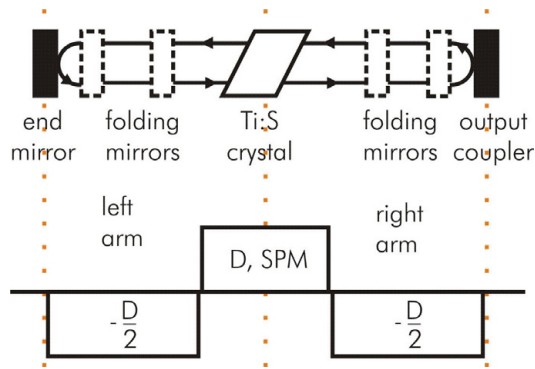


Figure 13. Second-order dispersion map of the cavity. The positive dispersion of the laser crystal D is balanced by the chirped mirrors. In the middle of the dispersion cells (dotted lines), the pulse is chirp free. Additionally, the pulse is modified by SPM in the crystal.

Also the output coupler plays a crucial role in the generation of ultra-broadband spectra. In combination with pump power, mirror losses and other factors, the out-coupling ratio determines the intra-cavity pulse energy and the available output power. It was found that a transmission of around 13% yields the broadest spectra (fig. 14). The spectral extremes are not resonant in the cavity, as they are transmitted by the output coupler. In particular in the long wavelength range, at 10 and 20 dB below the intensity maximum, corresponding to 1029 and 1115 nm, the transmission is 81% and 99%, respectively. The equivalent transmission ratios in the short wavelength range are 26% (-10 dB) and 37% (-20 dB). As the wings of the spectrum are not produced by stimulated emission in the Ti:sapphire crystal but rather through nonlinear phase modulation, the gain in these wavelength regions is much lower. To fulfill the resonance condition (impedance matching), this requires a lower out-coupling ratio. In order to take this into account, a special output coupler design was developed that has

lower transmission in the spectral wings (fig. 14). However, the increased spectral bandwidth is traded in for increased pedestals and satellites to the pulse. The output coupler is slightly wedged to prevent out-of-phase back-reflections into the cavity.

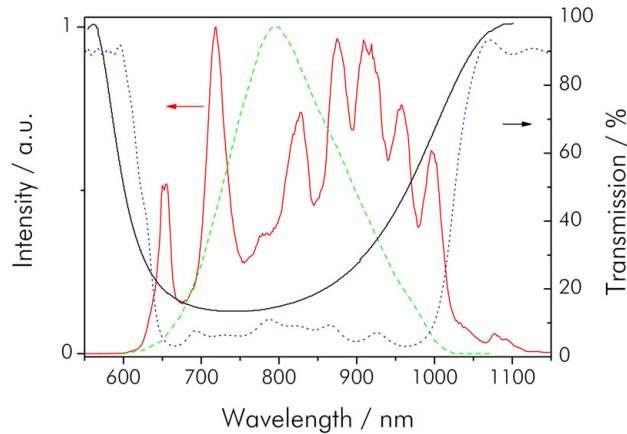


Figure 14. Transmission design curve of a 13% broadband output coupler (black solid line) and corresponding output spectrum (red solid line). The gain curve of Ti:sapphire (green dashed line) is shown for reference. The blue dotted line shows the transmission design curve for a broadband output coupler. In the spectral wings, a lower transmission ratio (~3%) helps to make these components resonant in the cavity.

2.3 The carrier-envelope phase of a mode-locked oscillator

One of the peculiar properties of a mode-locked laser is the intact phase relationship of the optical carrier wave between subsequent pulses. This justifies the definition of a phase of the carrier with respect to the peak of the pulse envelope, the so-called *carrier-envelope phase* φ (CE phase). Without additional measures, the CE phase is not constant, but advances by a random amount from pulse to pulse. Therefore, commonly a *pulse-to-pulse CE phase shift* φ that includes noise terms is also defined (fig. 15).

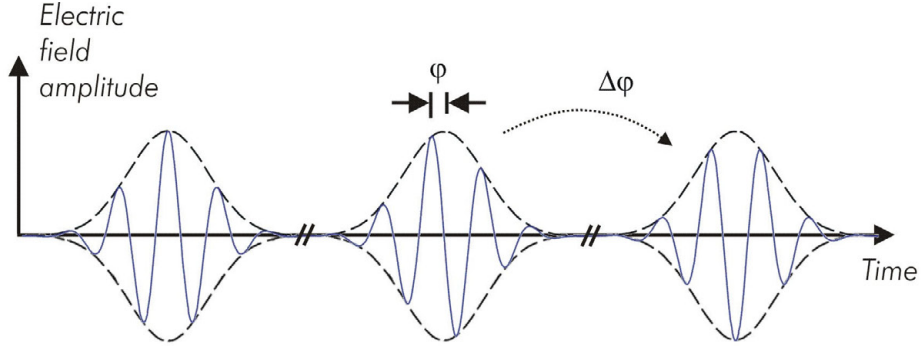


Figure 15. In the time domain, the relative phase between the carrier and the envelope φ evolves from pulse-to-pulse by the amount φ . In an unstabilized laser, φ contains noise contributions.

Here, the electric field of the pulse train is assumed to be represented by

$$E(t) = \sum_n \hat{E}(t - n\tau) \exp(i(\omega_c t - n\omega_c \tau + n\Delta\varphi + \varphi_0)), \quad \text{Eq. 5}$$

where $\hat{E}(t)$ is the envelope function of a single pulse, ω_c the carrier frequency, τ the time between pulses ($\tau = 1/f_{rep}$), and φ_0 a phase offset, so that $\varphi = m\varphi + \varphi_0$ for pulse m . Obviously, the duration of $\hat{E}(t)$ has to be smaller than τ . Furthermore, the definition of φ only makes sense for pulses that are sufficiently short compared to the time for a single optical cycle. Otherwise, if the shot noise uncertainty of the electric field maxima is larger than the difference between adjacent field maxima, the well-defined designation of a ‘pulse peak’ becomes impossible. For nanojoule near-infrared pulses, this limit is at a pulse duration of ~ 370 fs.

As equation 5 is periodic with period τ , it can be represented as a Fourier series. Simple algebra (see appendix A.1) shows that its spectrum consists of discrete frequencies, spaced by the repetition rate f_{rep} . These so-called *comb lines* can be addressed by

$$f_n = n f_{rep} + f_{CEO}, \quad \text{Eq. 6}$$

where n is a large integer ($n \sim 10^6$) and the *carrier-envelope-offset frequency* f_{CEO} is defined by

$$f_{CEO} = \Delta\varphi \frac{f_{rep}}{2\pi}. \quad \text{Eq. 7}$$

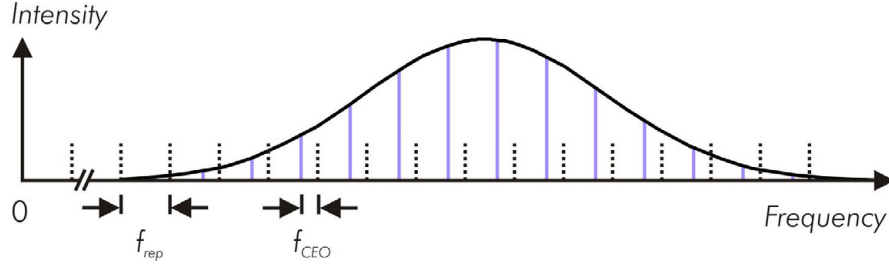


Figure 16. In the frequency domain, the elements of the frequency comb of a mode-locked pulse train are spaced by f_{rep} . The entire comb is offset from integer multiples of f_{rep} by an offset frequency $f_{CEO} = \varphi f_{rep}/2\pi$. Without active stabilization, both comb parameters are dynamic quantities, which are sensitive to perturbation of the laser.

Therefore, in the frequency domain, the spectrum of a train of pulses from a mode-locked oscillator consists of millions of narrow comb lines (fig. 16). This *frequency comb* is thus characterized by two properties: (1) the repetition frequency f_{rep} of the pulse train that determines the distance between adjacent comb lines and (2) the carrier-envelope-offset frequency f_{CEO} , which introduces a shift of the general comb position.

Another, equivalent way of describing the frequency comb and its two degrees of freedom is by (1) a central carrier frequency $f_{carrier}$ and (2) the spacing between the comb lines f_{rep} . Here, the comb lines are addressed by $f_m = m f_{rep} + f_{carrier}$, where m is an integer that may become negative. Recent studies [79, 80] indicate that this model may describe reality more accurately, as the fixed point of the comb lines, when changing the pulse energy (see chapt. 2.3.3), is close to the carrier frequency at the comb center.

The exact regularity, i.e. the equidistance of the comb lines has been verified to a very high degree (better than 10^{-16}) [81]. However, without active stabilization measures, both quantities are subject to perturbation of the laser. Environmental perturbations, such as air currents, mechanical vibrations and other noise sources will be reflected in the fluctuation of f_{rep} and f_{CEO} , as they result in pointing and other instabilities inside the laser cavity. Such instabilities effectuate a change in the net intra-cavity dispersion and also in amplitude-to-phase conversion inside the laser crystal due to the high intra-cavity peak power [82]. Consequently, also φ fluctuates from pulse to pulse in a non-stabilized laser and active control of the comb parameters is necessary to make the laser oscillator a source of phase-stable pulses and of a frequency-stable comb.

Experimentally it was found that fluctuations of f_{CEO} occur on a slower time scale than those of f_{rep} [34, 83].

The CE phase, and its frequency domain manifestation f_{CEO} originate from the difference between group and phase velocity inside the oscillator cavity, implying that

there is dispersion in the net index of refraction n . Assuming perfect dispersion-compensation by nonlinear effects inside the resonator yields (see appendix A.2)

$$f_{CEO} = \omega_c \frac{v_g}{2\pi} \left(\frac{1}{v_g} - \frac{1}{v_p} \right), \quad \text{Eq. 8}$$

where v_p and v_g are phase and group velocities (averaged over the resonator round-trip), respectively, and ω_c the center frequency.

This chapter is subdivided as follows: in 2.3.1 measurement of the two comb parameters is discussed in a general way, whereas 2.3.2 presents the details of a novel detection method for f_{CEO} . Chapter 2.3.3 illustrates how to control the comb parameters, i.e. how to give feedback to the laser oscillator. In 2.3.4 the degree of control over f_{CEO} through the detection method presented before is discussed. Exemplary applications of a phase-stabilized frequency comb are presented in the succeeding chapter.

2.3.1 Measurement of the frequency comb parameters

Based on this discussion it is evident that measurement and control of the comb parameters f_{rep} and f_{CEO} is desirable. In this way it is not only possible to position the comb lines in frequency space, but also to gain control over the CE phase and as such the electric field waveform underneath the pulse envelope in the time domain (see fig. 15).

Detection of the repetition frequency, i.e. the comb spacing is straightforward: shining the pulsed laser beam (or parts thereof) onto a fast photodiode will provide the corresponding signal. Given that in the frequency comb errors in f_{rep} are scaled by n , which is on the order of $\sim 10^6$, it is imperative to detect phase noise on f_{rep} with high sensitivity. This is accomplished by using a harmonic of f_{rep} for detection and stabilization. As phase noise power scales as the square of the harmonic number, in principle, the higher the harmonic the better the phase sensitivity obtained.

On the other hand, measurement of the carrier-envelope-offset frequency is more intricate. Generally, this is due to the fact that the phase of the oscillating electric field usually remains hidden in measurements, as they only depend on the intensity. Only relative phases between optical fields, e.g. in an interferometer can be measured. Consequently, in optics, the complex electric field amplitude remains unknown.

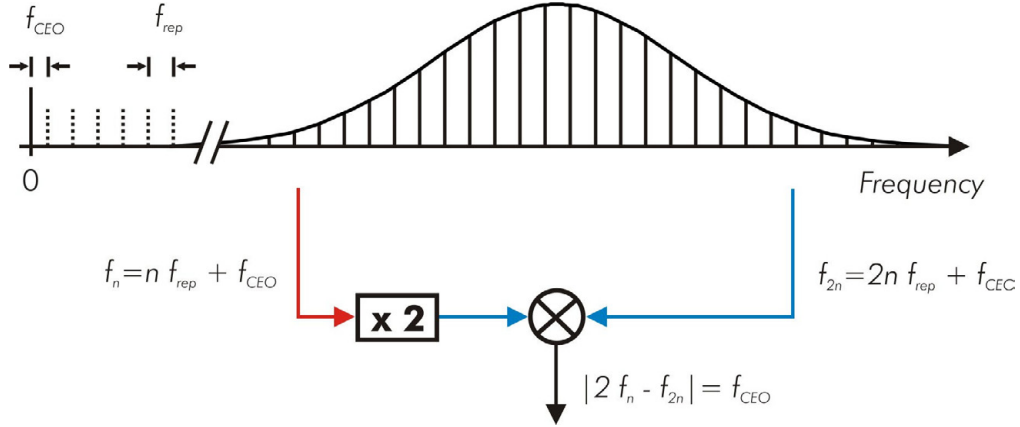


Figure 17. The principle of the self-referencing technique for detection of the offset frequency f_{CEO} . A comb line with mode number n at the red wing of the comb, whose frequency is f_n , is frequency doubled in a nonlinear device. If the frequency comb covers a full optical octave, a line with the number $2n$ exists simultaneously at frequency f_{2n} . The beat note between the frequency-doubled line and the comb line at $2n$ yields the offset frequency f_{CEO} .

It was not before the 1990s when the idea emerged to use the comb as its own reference for determining the offset frequency in an interferometric manner [12, 13, 32]. This *self-referencing technique* uses frequency-doubled spectral components from the long wavelength ('red') side ($2(n f_{rep} + f_{CEO})$) and mixes them with spectral components from the short wavelength ('blue') side ($m f_{rep} + f_{CEO}$). If the two components overlap spectrally ($m = 2n$), optical interference produces a heterodyne beating signal that contains information on f_{CEO} (fig. 17).

The underlying fundamental relationship is

$$f_{beat} = \pm |2f_n - f_m| = \pm |2(n f_{rep} + f_{CEO}) - (m f_{rep} + f_{CEO})| = k f_{rep} \pm f_{CEO}, \quad \text{Eq. 9}$$

where f_{beat} corresponds to the beating signal, and n , m and $k = 2n - m$ are integers. The detected heterodyne beating signal f_{beat} contains f_{CEO} pair-wise around multiples of the repetition frequency and at dc. Appropriate electronic bandpass-filtering will extract f_{CEO} itself.

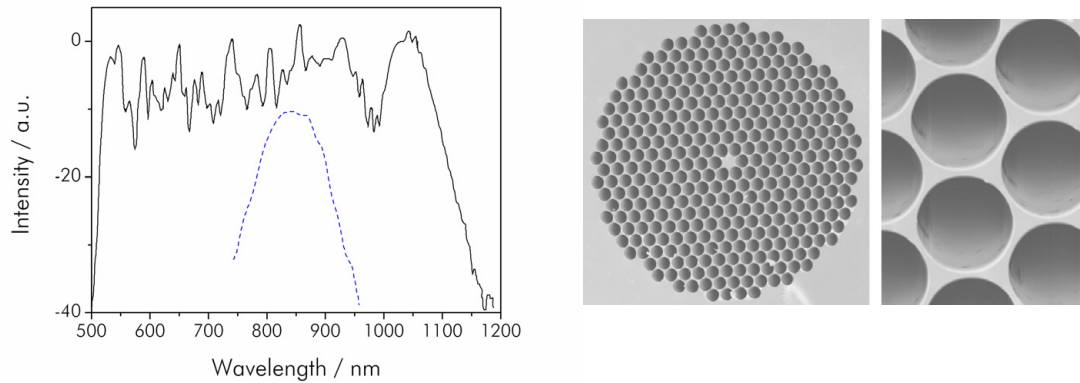


Figure 18. (a) Continuum generation by air-silica microstructure fiber. Self-phase modulation in the microstructure fiber broadens the output of the laser so that it spans more than one octave (solid line). The dashed line shows the original power spectrum entering the microstructure fiber. The spectra are offset vertically for clarity. (b) Scanning electron micrograph image of the input facet of a microstructure fiber. The structure consists of a $2.6\ \mu\text{m}$ diameter core, centered in a hexagonal lattice.

Obviously, this scheme intrinsically requires a comb spectrum spanning at least one octave. Before the recent demonstration of mode-locked oscillators that directly provide an octave-spanning spectrum, spectral broadening external to the laser cavity was employed.

Self-phase modulation in a highly nonlinear medium, usually an optical fiber was found to produce ultra-broadband spectra, especially when a microstructure fiber (photonic crystal fiber, holey fiber) is used to confine the light to a smaller core area and thereby increasing the intensity and the self-phase modulation effect [84, 85].

Microstructure fibers consist of a small fused silica core ($2 - 5\ \mu\text{m}$ diameter) surrounded by a honeycomb structure of air holes (fig. 18b). This results in a waveguide with a very high contrast of index of refraction between core and cladding. Thus, single mode propagation for a very large bandwidth is enabled which increases the interaction length tremendously. The design permits shifting the zero point of the GDD (customarily at $\sim 1.3\ \mu\text{m}$) to the center of the Ti:sapphire laser spectrum which keeps the pulse from dispersing and again increases the interaction length. By these measures, microstructure fibers maintain high intensities over a long distance, thereby leading to the strong broadening of the spectrum as shown in figure 18a.

The output spectrum from these microstructure fibers, however, is characterized by strong third- and higher-order chirp. This chirp stems from additional processes inside the fiber such as cascaded Raman effects, fission of higher-order solitons and possibly other incoherent processes [86]. These cannot be compensated easily [48, 87] and makes further use of the pulses impossible.

Higher-order variations of the self-referencing scheme, employing for instance the frequency-tripled long wavelength end and the frequency-doubled short wavelength end of the spectrum also exist [88]. On the one hand, bandwidth requirements are relaxed (less than one octave is required, e.g. the $2f$ -to- $3f$ scheme just mentioned needs f and $1.5 f$), but on the other hand the complexity of the scheme increases due to the additional nonlinear mixing steps. Typically, also the signal-to-noise ratio of the beating signal will become worse.

As the self-referencing scheme makes use of an interferometer of some sort, it is important in the implementation to pay attention to the spectral, temporal, polarization and spatial overlap of the interfering components. Spectral overlap, as the fundamental prerequisite was mentioned already above. Temporal overlap is typically accomplished by a retarding element, e.g. an adjustable block of glass that provides the group delay in one arm of the interferometer.

A variety of technical implementations of this self-referencing technique for the measurement of the CE phase has emerged over the last couple of years. For instance, the interference between different quantum paths in a semiconductor [20] or in optical poling [17] has been shown to contain information on the CE phase. A straightforward method that makes use of a single nonlinear crystal and provides a high degree of CE phase control will be presented in the next chapter.

At present, the most widely used implementation of the self-referencing technique for measurement of the offset frequency makes use of a so-called f -to- $2f$ interferometer [13, 89-91] (fig. 19). Prior to the interferometer, a fraction (typically 50:50) of the light from the output of the laser oscillator is branched off and spectrally broadened to an octave in a microstructure fiber. The continuum is then coupled into a Mach-Zehnder interferometer, where a dichroic beam splitter separates the long wavelength ('red') part from the short wavelength ('blue') part of the spectrum.

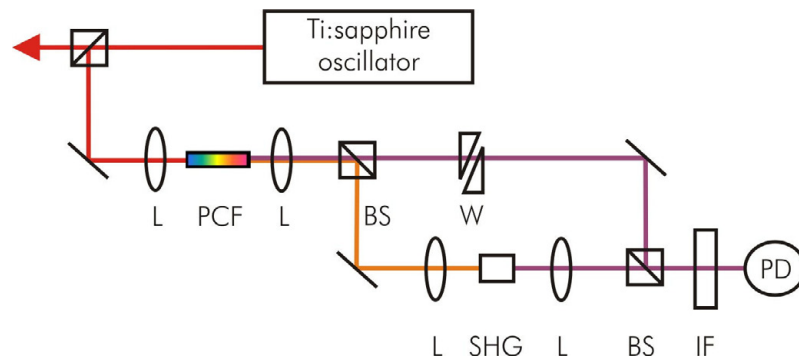


Figure 19. Schematics of a fiber-based f -to- $2f$ interferometer. L: focusing lens; PCF: photonic crystal (or microstructure) fiber; W: wedges for delay adjustment; SHG: frequency doubling crystal (KNbO_3); BS: beam splitter; IF: interference filter; PD: photodiode.

The interferometer arm for the long wavelength light contains a KNbO_3 frequency-doubling crystal. Several waveplates in the interferometer rotate the polarization such that second harmonic generation in the crystal and recombination of the beams in the second beamsplitter is optimized. The long wavelength interferometer arm contains adjustable fused silica wedges that control the delay between the two arms and ensure correct temporal overlap. In order to reduce unwanted light at the detection photodiode, the region of spectral overlap is selected by means of an interference filter (or, alternatively, a grating combined with a slit). This improves the signal-to-noise ratio, as the beating signal is contained only in a narrow spectral range.

This scheme, although widely used, has several technical and fundamental drawbacks: (1) the interferometer is alignment-sensitive, (2) in particular, coupling into the tiny core of the microstructure fiber is a tedious task. Fundamentally, the scheme sets limits to the quality of the offset frequency detection and stabilization, as (3) the fact that a beam branched off from the main beam is used for f_{CEO} detection. Relative phase fluctuations and drifts compromise the achievable offset frequency stability. Hence, any phase jitter accumulating between the laser output and the output of the phase control setup appears in the usable laser output, even if the electronic feedback loop works perfectly. Furthermore, (4) the auxiliary setup for f_{CEO} stabilization introduces excessive dispersion, preventing the broadband output from being compressed to a few-cycle pulse. The microstructure fiber also poses a limit to the phase-locking quality, as (5) the fiber-coupling induces amplitude fluctuations. These amplitude fluctuations are written via amplitude-to-phase conversion, mostly due to the Kerr effect, onto the CE phase (conversion coefficient $C_{AP} = 3784 \text{ rad/nJ}$). An intensity fluctuation of 1% for a 6 nJ Ti:sapphire oscillator would already result in a phase shift of 227 rad [92].

2.3.2 CE phase stabilization by difference frequency generation

As an alternative to the microstructure fiber-based f -to- $2f$ interferometer, a simple, yet highly effective scheme for stabilization of the CE phase is presented here. It avoids the downsides of the previously mentioned scheme, as it allows for CE phase stabilization directly in the usable laser output. Thus, the CE phase is controlled directly in the beam that is used for applications. Due to the moderate dispersion of the employed nonlinear medium, the transmitted laser pulses are re-compressible. As a consequence, the full laser power is used for inducing the nonlinear processes, resulting in an enhanced beating signal. Also, as no branching off for phase-stabilization is needed, almost the entire laser power is available for application. Furthermore, it relies on the integration of the interferometer into a single monolithic crystal, thereby obviating complex alignment-sensitive setups and improving the

achievable CE phase stability. Improved spatial overlap between the two interfering waves, due to the absence of walk-off effects, results in an increased signal-to-noise ratio of the beating signal at f_{CEO} . The absence of a microstructure fiber avoids instabilities (in amplitude and phase) associated with coupling into its tiny core.

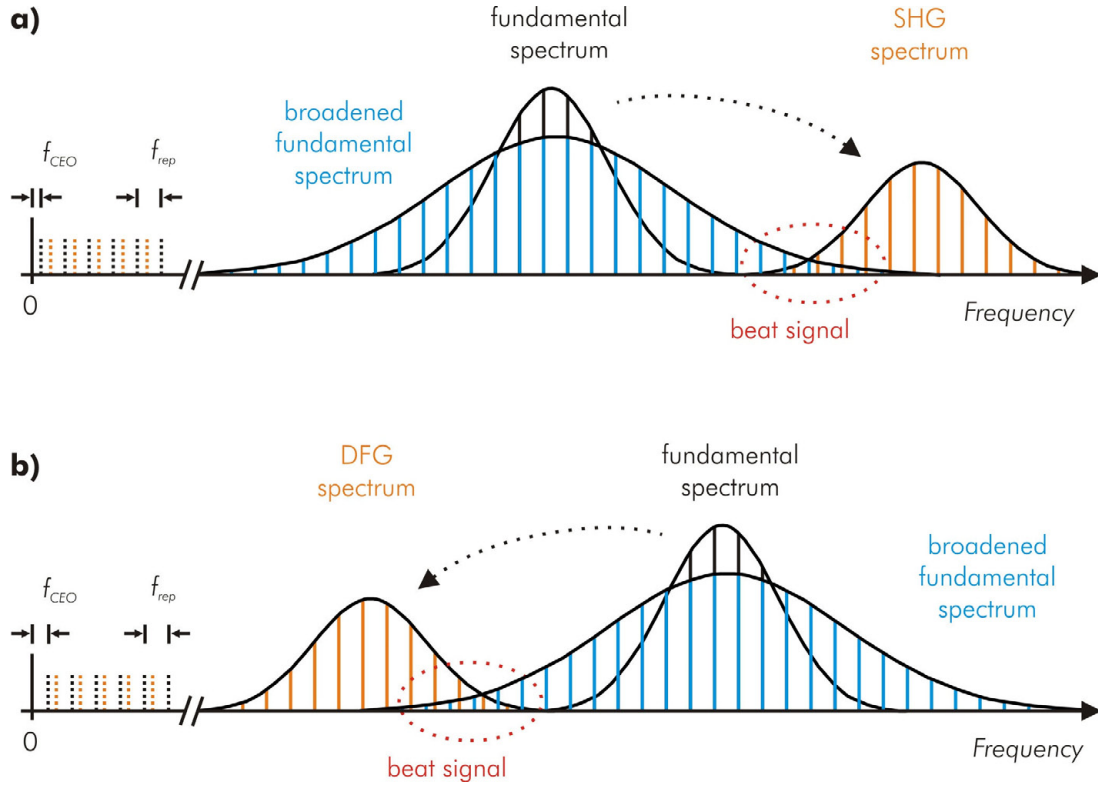


Figure 20. Principle of f_{CEO} detection: an additional frequency comb, $f_m = m f_{rep} + 2 f_{CEO}$ ($f_k = k f_{rep}$), is created in a nonlinear crystal by SHG, top panel (DFG, bottom panel). The frequency comb of the laser $f_n = n f_{rep} + f_{CEO}$ is spectrally broadened by SPM. With k , n and m being integers, the generated combs partially overlap to produce a heterodyne beat note at f_{CEO} .

When the peak intensity of the pulses and the nonlinearity in a frequency-mixing crystal are large enough, both nonlinear frequency mixing and self-phase modulation (SPM) occur at the same time. Second-order nonlinear frequency mixing can result in *second-harmonic generation* (SHG) or *difference frequency generation* (DFG), depending on the phase-matching in the crystal. Previously, beating at f_{CEO} was observed in thin BBO [91] or ZnO [93] crystals, phase-matched to generate second harmonic light.

The self-referencing scheme is implemented here in the following way: through nonlinear interaction in a crystal, a second frequency comb is generated by frequency-

doubling the short wavelength end of the original frequency comb (fig. 20a), or by generation of the difference frequency between the wings of the spectrum (fig. 20b). Effectively, the crystal acts as a common-path f -to- $2f$ interferometer. At the same time, the original frequency comb is spectrally broadened by self-phase modulation. If the original frequency comb is wide enough, in the region of spectral overlap, a beating signal at f_{CEO} can be detected. It should be noted that a frequency comb generated by DFG is intrinsically phase-stabilized, as

$$f_{DFG,k} = f_m - f_n = m f_{rep} + f_{CEO} - (n f_{rep} + f_{CEO}) = k f_{rep} \quad (k = m - n). \quad \text{Eq. 10}$$

In principle, such self-phase-stabilized difference-frequency light could be used for phase-sensitive applications. However, the resulting pulse train is weak and located in a shifted wavelength region, the infrared [94, 95].

After compression by several bounces from chirped mirrors, the 6-fs pulses from an ultra-broadband Ti:sapphire oscillator (see chapter 2.1) are focused in a highly nonlinear periodically poled lithium niobate crystal (PP-MgO:LN, HC Photonics Corp.) to induce SPM and SHG, respectively DFG (fig. 21). In the desired wavelength range, PP-MgO:LN has a higher effective nonlinear coefficient than other customarily used crystals such as PPKTP or LBO. The crystal is doped with magnesium-oxide to prevent damages due to photorefractive effects (so-called gray-tracking). Undoped lithium niobate crystals have to be heated to $\sim 180^\circ \text{C}$ for this reason, whereas MgO-doped crystals can be operated at room temperature. The peak intensity inside the crystal is estimated to be several tens of gigawatts per cm^2 . Tests with infrared picosecond pulses have shown that at intensities of approximately 10 GW/cm^2 (curable) damage due to photorefractive effects occurs [96]. The spot size inside the crystal, w_0 , is estimated at $\sim 15 \mu\text{m}$.

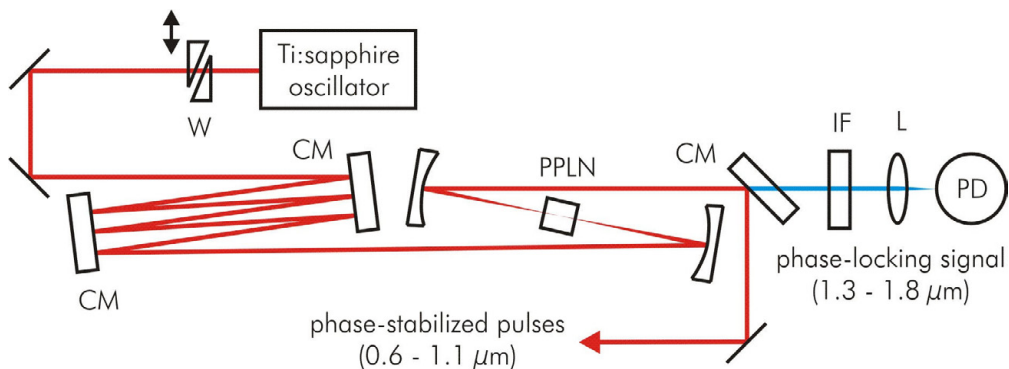


Figure 21. Experimental realization of the monolithic CE phase-stabilization scheme. CM: chirped mirror for pulse compression; W: fused silica wedge for fine adjustment of chirp; IF: interference long-pass filter (cut-off 1400 nm); PPLN: periodically-poled MgO-doped lithium niobate crystal; L: achromatic lens; PD: InGaAs photodiode.

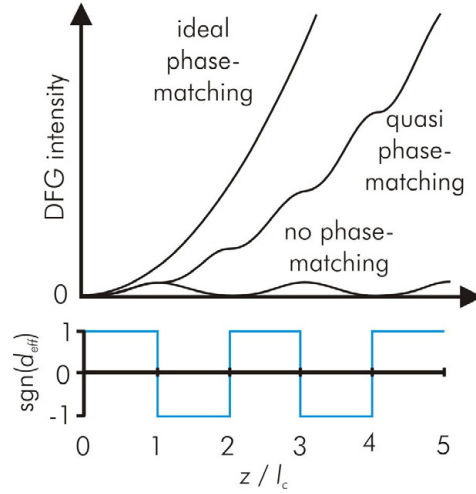


Figure 22. Growth of the difference frequency light intensity along the axis of propagation for ideal birefringent phase-matching, quasi-phase-matching, and without phase matching (top). The sign of the corresponding nonlinear coefficient d_{eff} of the periodically-poled crystal for quasi-phase-matching is shown at the bottom.

Both end facets of the crystal were broadband antireflection-coated to reduce Fresnel losses. It was found that crystal lengths between 2 and 5 mm show optimum nonlinear interaction and therefore the strongest beating signal.

The periodical poling of the crystal enables phase-matching of type 0 ($e + e \rightarrow e$). Quasi-phase-matching circumvents the problem of the back-conversion from the newly generated light to the fundamental in the interval from l_c to $2l_c$ by flipping the sign of the nonlinear coefficient accordingly (fig. 22).

Depending on the poling period Λ either the second harmonic or difference frequency is generated ($\Lambda = 11.21 \mu\text{m}$ for DFG, $\Lambda = 9.07 \mu\text{m}$ for SHG). The poling period is determined according to

$$\Lambda = \frac{2\pi}{\Delta k} = \frac{2\pi}{2k(\omega) - k(2\omega)}, \quad \text{Eq. 11}$$

where k is the wave vector mismatch due to the material dispersion of the nonlinear crystal.

After the PP-MgO:LN crystal, a beam splitter of some sort is necessary to separate the difference frequency spectrum (respectively the second harmonic) from the fundamental spectrum. On the other hand re-compression of the pulses is required for most applications, due to the dispersion of the crystal.

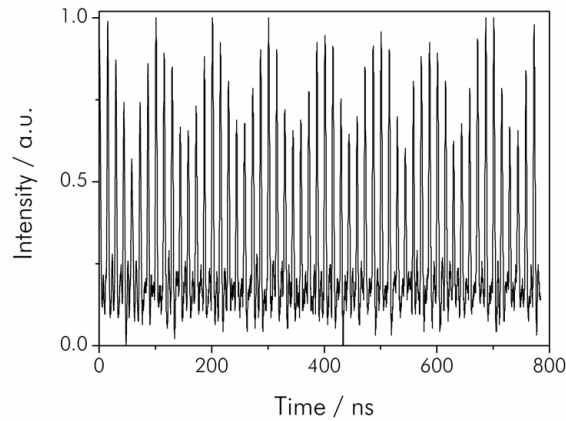


Figure 23. The pulse train from the nonlinear crystal filtered in the wavelength range of shorter than 1400 nm is modulated at f_{CEO} , monitored with a digital oscilloscope (TDS7104, Tektronix Inc.).

Therefore, one of the chirped mirrors used for pulse compression acts as a dichroic mirror: it reflects the fundamental spectrum and transmits the infrared components of the beam at >1250 nm (respectively the components at <630 nm), which emerge from the nonlinear interactions in the PP-MgO:LN crystal. The transmitted beam is passed through a long-pass filter with cut-off at 1400 nm (FEL1400, Thorlabs Inc.) and detected by an InGaAs photo diode (1811-FC, New Focus). In case the phase-matching for SHG is employed, short-pass filtering (FES0650, Thorlabs Inc.) and detection with a Si photo diode (S5627, Hamamatsu Inc.) is necessary.

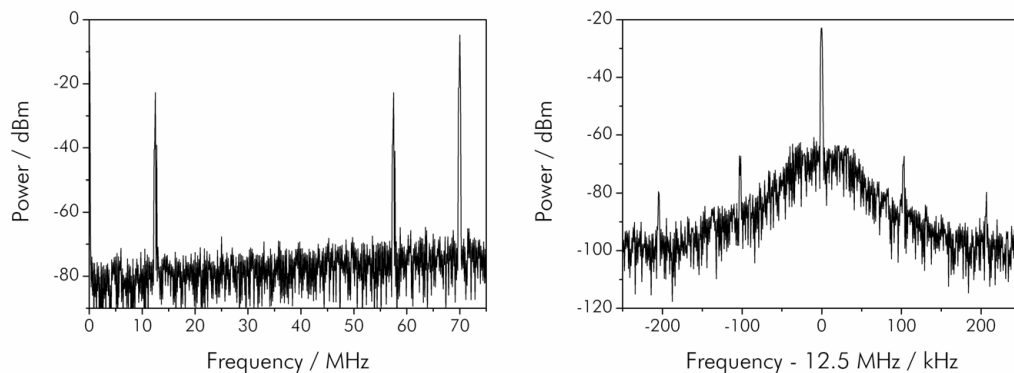


Figure 24. (a) rf spectrum of the same signal as in fig. 23 measured with a spectrum analyzer (E4401B, Agilent Inc.). The right peak at 70 MHz stems from the repetition rate f_{rep} . The two inner peaks represent the offset frequency f_{CEO} and the mixing product $f_{rep} \cdot f_{CEO}$. Resolution bandwidth is 100 kHz. (b) Close-up of the phase-locked beat note at f_{CEO} . Resolution bandwidth 1 kHz.

The signal of this photo detector is shown in figures 23 and 24. In the time domain, the detected pulse train is modulated with the offset frequency (fig. 23), whereas in the frequency domain side bands to the repetition rate and its harmonics are observable according to equation 9 (fig. 24).

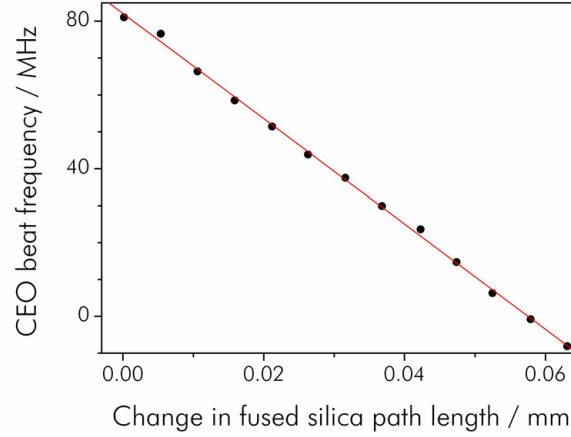


Figure 25. Measured CEO beat signal versus change in round-trip path length through the intra-cavity fused silica wedges.

By optimizing the chirp of the pulses in the crystal by means of wedged fused silica plates (W, see fig. 21) and the number of bounces on the extra-cavity chirped mirrors, a signal-to-noise ratio in excess of 55 dB in a resolution bandwidth of 100 kHz can be achieved. This permits routine locking of the offset frequency to a reference with the servo loop system described in the next chapter. Typically, a signal-to-noise of more than 30 dB in 100 kHz bandwidth is required for reliable phase control. A beat signal showing a comparable signal-to-noise ratio is observed at about 580 nm using the nonlinear crystal optimized for SHG. The beat frequency can be tuned with the wedged plates inside the cavity, as they change the intra-cavity relationship of group and phase delay. The fused-silica path length dependence of the beat frequency (fig. 25) is linearly fit as $f(\delta z) = f_{CEO} - 20 \text{ mm}^{-1} f_{rep} \delta z$, where f is the beat frequency, δz the change in fused-silica path length, f_{CEO} the beat frequency at $\delta z = 0$ and f_{rep} the repetition rate. The coefficient of the linear function (20 mm^{-1}) matches excellently the one determined from the group and phase delay difference of fused silica, providing clear evidence for the origin of the observed beating.

Figure 26a shows the long-wavelength tail of the spectrum exiting the crystal. Newly generated spectral components in the wavelength region of longer than 1150 nm are clearly visible in the near infrared region when the crystal is translated into the focal region of the laser beam. The main part of the spectrum, from 600 to 1150 nm, does not change in shape. The infrared light is attributed to SPM and phase-matched DFG.

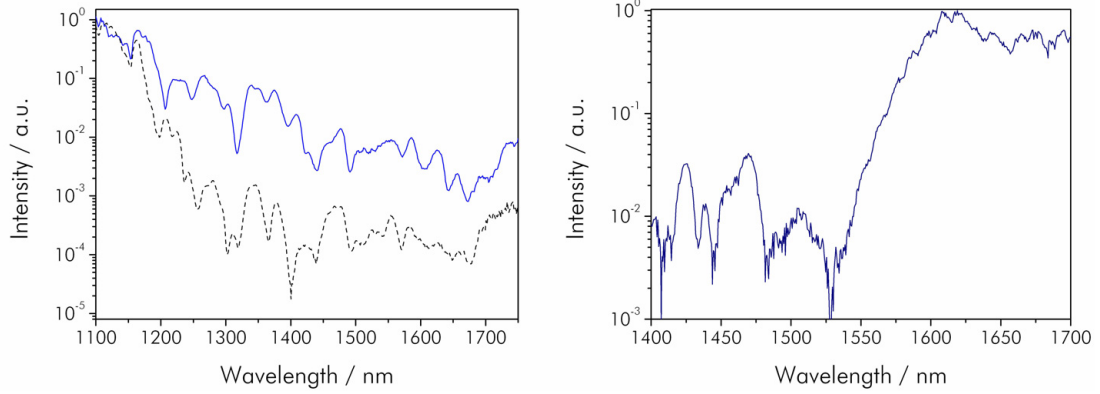


Figure 26. (a) The long-wavelength tail of the laser spectrum exiting from the nonlinear crystal, measured with an optical spectrum analyzer (AQ-6315A, Ando Corp.). The solid line shows the optimized spectrum, whereas the dotted line depicts it with the crystal shifted out of focus, for reference. (b) Difference frequency spectrum generated in the PPLN crystal, measured with the same optical spectrum analyzer.

A nonlinear CE phase shift due to SPM inside the PP-MgO:LN crystal estimated at $0.012 \cdot 2\pi$ rad by numerical simulations is present. Fluctuations of this phase shift, however, do not compromise the stability of the CE phase in the output beam, because they are fully compensated by the servo loop. This is in contrast with the conventional scheme, where the SPM-induced phase noise in the auxiliary beam for phase stabilization is written onto the main laser output and cannot be compensated for by the servo loop.

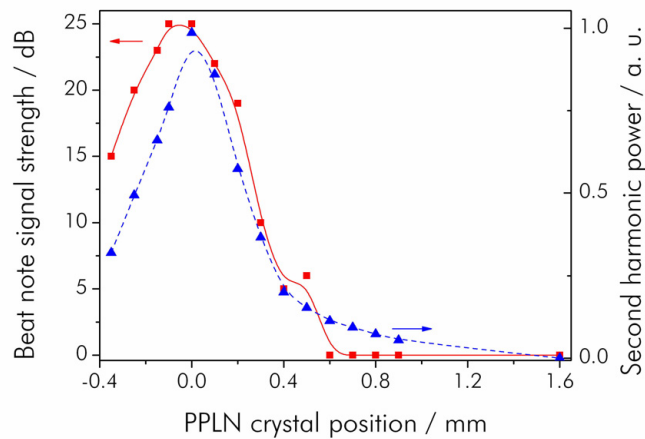


Figure 27. Comparison of second harmonic with f_{CEO} beat note strength. The relative power in the second harmonic with a maximum at 432 nm wavelength was measured with an optical spectrum analyzer (AQ-6315A, Ando Corp.). The beat note signal-to-noise ratio in a 100 kHz bandwidth was measured with an rf spectrum analyzer (E4401B, Agilent Inc.).

Figure 26b shows the generated difference frequency spectrum. The beating between DFG and SPM (SHG and SPM) is observed at $\lambda > 1350$ nm ($\lambda \approx 580$ nm).

In order to verify the origin of the beating signal several tests were performed. Figure 27 illustrates the correlation between the beat note strength and the power in the second harmonic generated in the crystal.

In the present system, the chirped mirror compressor and the PP-MgO:LN crystal have a combined loss of $\sim 30\%$ due to the mirror coating quality, the residual photorefractive effect in the crystal, etc. The photorefractive effect alone is responsible for more than 20% loss. This loss can in principle be avoided by heating the crystal.

The dispersion of the crystal may be compensated by chirped mirrors. The pulse energy passed through the compressor is ~ 4.3 nJ. The compressed pulses have been characterized with a broadband SPIDER apparatus [68]. The absence of serious phase distortions from nonlinear frequency mixing is verified by comparing the SPIDER results with the crystal being in focus and out of focus. The measurements yielded, within the measurement uncertainty, the same results as figure 10.

Future improvements to the offset frequency detection with a monolithic periodically poled crystal could make use of buried waveguides written into the crystal. By comparing the mode-field diameter for bulk and waveguide PP-MgO:LN crystals one can estimate for the waveguide a theoretical second harmonic conversion efficiency more than two orders of magnitude larger than for the bulk crystal. As a result, the required pulse energy for f_{CEO} detection is reduced, whereas the signal-to-noise-ratio of the beating signal can be improved. In particular, waveguide writing by reverse proton exchange is suitable for this purpose, as it preserves the material nonlinearity, resulting in a three-fold improvement in conversion efficiency over other writing techniques [35]. Care has to be taken in the design of such a PP-MgO:LN waveguide crystal, as the poling period for a waveguide crystal differs from that for bulk crystals. Furthermore, the use of a buried waveguide will result in better spatial mode quality after the crystal.

2.3.3 Control of the frequency comb parameters

Having measured both radio frequencies that constitute the two degrees of freedom of the frequency comb, the remaining question is how to control them.

Basically, both parameters are controlled and stabilized with *phase-locked loops*, however, the actual mechanism for giving feedback to the laser oscillator is different. Similar electronic feedback loops are employed in chapter 4.1.2.

Theoretically, if the electronics and the feedback are infinitely fast, any fluctuation in f_{rep} or f_{CEO} will be compensated for. Limits to the speed of the locking loops, however, make it that passive stability is important for producing a stable laser.

The three primary factors affecting phase stability are mechanical vibrations, air pressure changes, and temperature changes. Vibrations are addressed by using low profile and solid mirror mounts throughout the laser cavity. Enclosing the laser in a rigid box helps to reduce vibrations due to acoustics and also addresses the problem of air pressure changes. Air pressure fluctuations are detrimental because they change the density of the air in the cavity, which in turn changes the effective optical path length. Although this is a small effect, it can easily change the cavity length a wavelength or more, which in turn, changes the comb frequencies by f_{rep} or more. Although the long term drift of f_{CEO} and f_{rep} caused by temperature changes can easily be compensated by the feedback loop, due to the limited actuator dynamic range, the duration of locking is limited.

As the rms⁵ CE phase noise of a non-stabilized laser oscillator exceeds many cycles in seconds ($70 \cdot 2\pi$ rad in 0.1 s in ref. [97]) even when environmental shielding measures are taken, control of the CE phase becomes an issue. Having detected the repetition rate by a photodiode and the offset frequency by the self-referencing scheme, closing the phase-locked loop is the next step. Phase-locking means that the phase of a slave signal (here f_{CEO} , respectively f_{rep}) tracks a reference signal (e.g. from a frequency generator), so that the phase difference is zero on average. If the reference source is stabilized to a time standard, e.g. an atomic clock, the position of the frequency comb lines is determined in an ‘absolute’ manner (see chapter 5.1 for ‘absolute’ frequency measurements). A phase-locked loop generally consists of a phase detector (or comparator), loop filter and voltage-controlled oscillator (fig. 28).

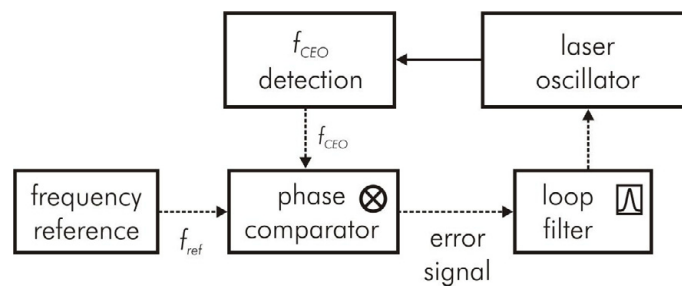


Figure 28. Block diagram of a phase-locked loop for offset frequency stabilization. The offset frequency detected by the self-referencing interferometer is mixed with a reference signal (e.g. from a frequency synthesizer) in a phase comparator to produce an error signal. With the loop filter the gain of the loop is shaped to achieve optimum phase-lock quality.

⁵ rms: root-mean-square, also known as the quadratic mean.

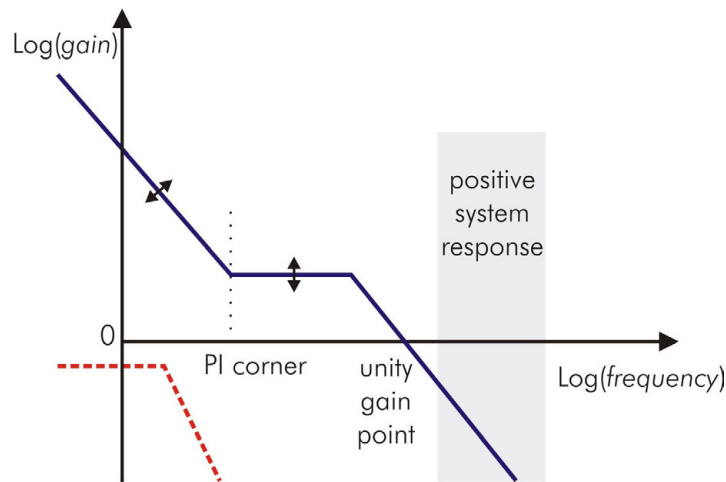


Figure 29. Schematic gain characteristics of the loop filter (Bode magnitude plot). For comparison the gain curve of a low-pass filter is shown (red dashed line). The gain is theoretically infinite at zero frequency and has to be below unity in the spectral region where positive system feedback occurs. The PI corner and unity gain point are at 10 Hz – 1 kHz and ~100 kHz, respectively. The adjustable gain parameters are indicated by arrows.

In the simplest case, the phase detector consists of an analog double-balanced mixer, which has an output proportional to the sine of the phase error, i.e. the phase difference between slave and reference signal. Therefore, it can only be assumed to be linear for small deviations ($\ll 1$ rad).

In addition to that, the output changes its sign at $\pm\pi$ rad, so an instantaneous value of the phase error exceeding π rad will lead to a cycle slip. Consequently, the capture range of an analog mixer is 2π .

On the other hand, digital phase detectors can provide a linear output and wider phase-detection range, as they detect not only the phase but also account for cycle slips. Such a detector counts the cycles (i.e. zero crossings with, e.g. positive slope) of both slave and reference input and outputs a voltage proportional to the cycle difference. It can track up to 16π of phase difference.

Afterwards, the error signal is fed to the loop filter that electronically shapes the system response, i.e. the gain of the loop, by e.g. a PI-circuit, a combination of a proportional and an integrating amplifier (see fig. 29). The effect of the loop filter is similar to a low-pass filter. The gain has a $1/f$ characteristic at low frequencies in order to have infinite gain at dc. For intermediate frequencies the gain is constant, i.e. the output is proportional to the input. For frequencies above ~100 kHz, the gain again has a $1/f$ characteristic so that it reaches values smaller than unity for frequency regions of positive feedback so that loop oscillation is avoided. Usually, the overall gain level, its shape (integrator time constant vs. proportional gain) and the gain sign can be adjusted.

2. Ultra-broadband oscillators

The control signal output by the loop filter is used to provide negative feedback to the laser oscillator. The combination of oscillator and feedback actuators constitute the electronic voltage-controlled oscillator in the schematic of the phase-locked loop.

Various methods can be employed to actually provide feedback to the Ti:sapphire oscillator cavity. Controlling the repetition frequency, which is inversely proportional to the cavity length, is a relatively easy task. Mounting one of the cavity (end) mirrors on a small piezo-active element that can displace the mirror and thereby change the optical path length of the resonator is sufficient.

For offset frequency control, three options are available: the oscillator cavity frequently contains a pair of glass wedges for fine-tuning the dispersion. Mounted on piezo-actuators, these allow for controlling the offset frequency f_{CEO} , as they affect the difference between group and phase velocity (see eq. 8). However, as these glass wedges are relatively large, the feedback bandwidth is insufficient with this method.

If the laser oscillator comprises an intra-cavity prism sequence, the end mirror after the second prism may be tilted [65]. After the prism sequence, the light is linearly spectrally dispersed on the end mirror (see fig. 5).

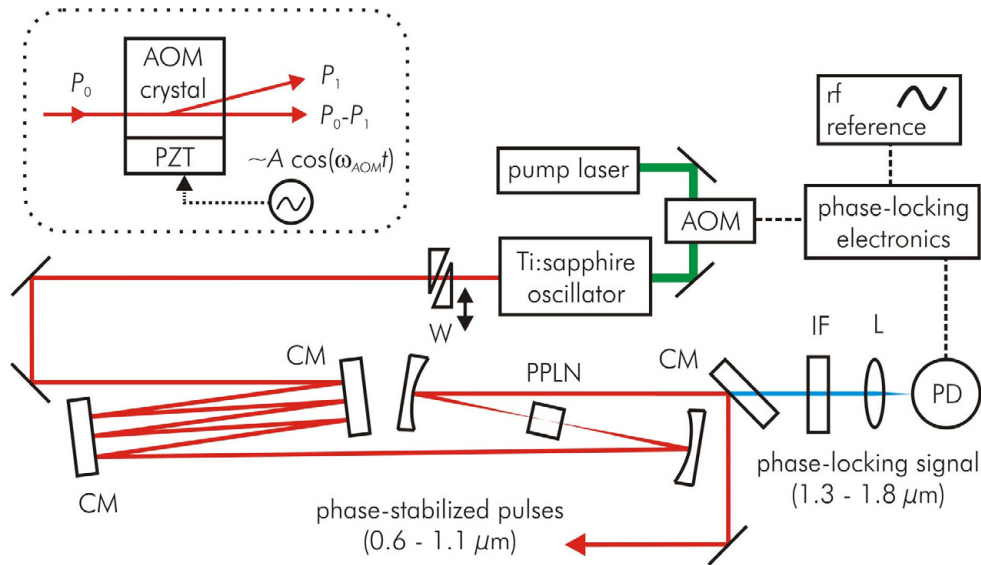


Figure 30. Setup for the offset frequency feedback loop. Phase-locking electronics (XPS 800, Menlo Systems GmbH); AOM: acousto-optic modulator (AOM-405, IntraAction Corp.), rf reference: frequency generator (2022D, Marconi Corp.), referenced to a quartz clock (OCXO8607, Oscilloquartz SA). Inset shows the AOM in the noise-eater configuration. Varying the amplitude A of the driving signal proportionally changes the light power in the first diffracted order P_1 , thereby modulating the power in the undiffracted beam. PZT: piezo-electric transducer.

Tilting the end mirror in the plane of incidence introduces a linear phase delay versus frequency. Just as in the previous method this influences the difference between phase and group delay and thereby changes the offset frequency.

However, for the all-chirped-mirror oscillators that are the topic here, a different stabilization option has to be employed: amplitude modulation of the pump power (fig. 30). This is obtained by placing an acousto-optic modulator (AOM) in the path of the pump laser beam in such a way that the zero order transmitted beam undergoes an amplitude modulation of a few percent ('noise-eater configuration'). Depending on the strength of the applied voltage, a fraction of the pump laser power is diffracted into first order and hence cannot contribute to pumping the crystal. This method takes advantage of nonlinear amplitude-to-phase conversion in the Ti:sapphire crystal to control the offset frequency. Here the speed of the feedback is limited by the upper state lifetime of the crystal, which is approximately 10 μ s, which results in a feedback bandwidth of about 100 kHz.

According to soliton perturbation theory, the change in pulse energy, caused by the change in pump power is actuating on the offset frequency mainly through two pathways [33, 82]: firstly, the optical Kerr effect in the gain crystal, modulated by the pulse energy, exerts a phase shift onto the carrier. Secondly, the group velocity varies with pulse energy, owing to a shift of the laser spectrum. Other effects, such as the change in optical cavity path length are found to be negligible.

Therefore, a change in intra-cavity pulse energy from W_0 to W changes the offset frequency f_{CEO} or equivalently the pulse-to-pulse CE phase shift φ by [33]

$$\Delta\varphi(W) - \Delta\varphi(W_0) \approx \delta (P_{peak}(W) - P_{peak}(W_0)) - \omega_0(W_0) D (\omega_0(W) - \omega_0(W_0)), \quad \text{Eq. 12}$$

where P_{peak} is the pulse peak power inside the gain medium, δ the Kerr phase shift (per unit power), D the net intra-cavity GDD and ω_0 the center frequency of the laser spectrum.

The same mechanisms that are exploited for stabilization are also causing f_{CEO} fluctuations: laser power fluctuations due to environmental disturbances are written onto f_{CEO} , e.g. through an intensity-related spectral shift $df_{CEO}/dI \sim \omega_c/I$. Empirically, it was found that in the parameter space of mode-locking conditions, loci exist where $df_{CEO}/dI = 0$. Operating a CE phase-stabilized oscillator near such a point can lead to minimum noise of f_{CEO} [82], as intensity fluctuations are the main contributors of CE phase noise in all-chirped-mirror oscillators. Minimizing the coupling coefficient therefore reduces the noise on f_{CEO} . On the other hand, stabilizing f_{CEO} at the same time reduces amplitude noise through the coupling coefficient.

One of the key factors for intensity fluctuations and therefore CE phase stability is the pump laser. Only pump sources that emit in a single spatial mode, with low amplitude noise can provide low CE phase noise [98].

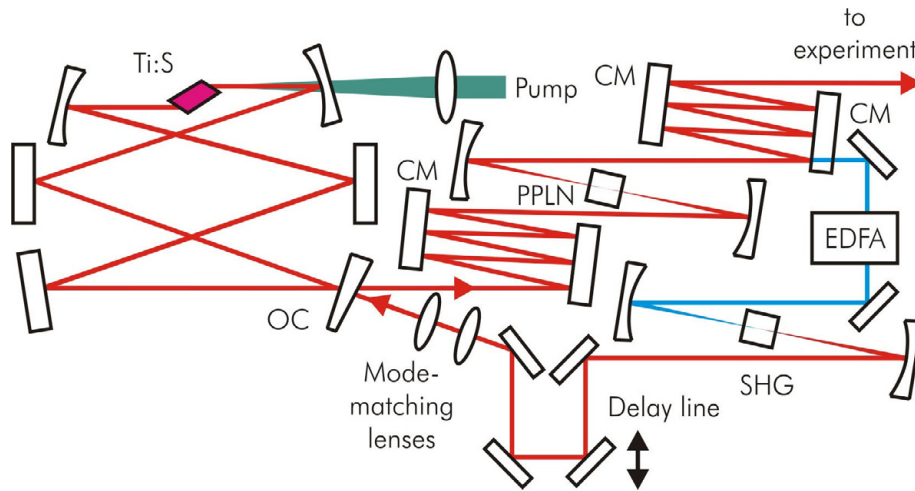


Figure 31. Schematic of the self-injection-locking principle. The difference frequency (1.3 – 1.9 μm) is generated as described above. Subsequently, the material dispersion from the PPLN crystal is compensated by a chirped mirror pair. One of the mirrors acts as a beamsplitter that separates the fundamental spectrum from the difference frequency light. The former can be used for experiments; the latter is amplified in an erbium-doped fiber amplifier (EDFA) and focused on a nonlinear crystal (SHG) for the generation of the second harmonic (0.7 – 0.9 μm), which is subsequently injected into the cavity, after spatial mode and delay adjustments. The oscillator cavity is depicted here in a ring configuration, as this facilitates the injection of light through the output coupler (OC). However, self-injection locking can also be realized with linear oscillator cavities.

Potentially, a future alternative method for giving feedback to the oscillator without the need for electronic phase-locking loops is *self-injection-locking*. The concept of injection-locking is commonly used with cw single-frequency lasers, where a low-noise low-power master laser is seeding a noisy high-power slave laser. The noise level of the latter is strongly reduced by injecting the output of the former through a partially transparent cavity mirror. Similarly, self-injection locking is used to force a laser diode to run at a certain frequency by means of spectrally filtered optical feedback from an attached fiber Bragg grating [99].

Here, the fact that a signal generated by difference frequency generation is intrinsically CE phase-stabilized ($f_{CEO} \equiv 0$) is exploited (cf. chapter 2.3.2). Frequency doubling the difference frequency light yields a CE phase-stabilized signal in the wavelength region of the original spectrum, which is coupled into the cavity through a mirror with some transmission (fig. 31). Provided that the delay and the spatial mode are adjusted properly, the injected light forces the offset frequency to zero. In the frequency domain picture, the fluctuating cavity comb modes are stabilized to the fixed comb modes of the injection signal. The higher the injected power, the larger the dynamic range of the

locking scheme, i.e. the larger the allowable excursions of the offset frequency. Using the parameters of an ultra-broadband oscillator and according to [100, 101]

$$P_{inj} > \left(\frac{\Delta\omega}{\omega_{rep}} \right)^2 \frac{Q^2}{4} P_0, \quad \text{Eq. 13}$$

about 100 mW of injection light power provides a dynamic locking range of 10% of the repetition frequency ($0 < f_{CEO} < \omega_{rep}/2\pi$). Here P_{inj} denotes the average power of the injected light; ω represents the dynamic range; P_0 the average output power of the oscillator, and Q the cavity finesse.

2.3.4 CE phase stability characterization

Once the phase-locking is established for stabilization of the offset frequency, obviously, it is desirable to estimate the precision of the stabilization.

But merely recording the fluctuations of the beating signal at the photo diode in the locking loop is not sufficient. This so-called *in-loop measurement* can only assess the effectiveness of the locking electronics, i.e. the degree of tightness of the servo loop. For example, when a noisy mixer is used as the phase detector of the locking loop, its output may still indicate a tight lock, while in actuality the mixer noise has been written back onto the slave laser. The same is true for the photo diode, the locking electronics and all other components of the phase-locked loop.

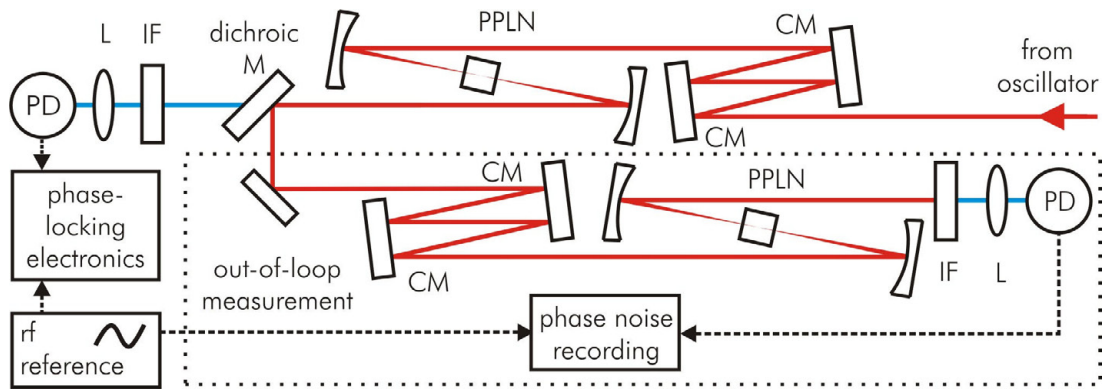


Figure 32. Schematics of the setup for characterizing the CE phase locking quality. A second monolithic detection for f_{CEO} is attached at the phase-stabilized output of the primary CE phase locking loop. After locking the offset frequency with the phase-locking loop to a reference, the signal from the photodiode (PD) of the second detector is recorded with a vector voltmeter (slow drifts), a digital oscilloscope (fast jitter) and a voltmeter (intermediate frequency region) and compared against the reference signal to extract the CE phase noise.

In order to determine an upper boundary of the offset frequency fluctuations, a secondary f_{CEO} detection loop has to be set up for an *out-of-loop measurement*. This out-of-loop signal provides an upper limit to the stability of the CE phase, as phase noise added by the locking electronics and both the in-loop and out-of-loop CE phase detection systems is included. However, provided that both detection systems are identical, common mode noise, such as phase noise stemming from amplitude-to-phase conversion of laser amplitude fluctuations is not detected.

The spatial and temporal matching of the waves interfering in the monolithic PPLN crystal as described in chapter 2.3.2 is expected to improve CE phase control over that provided by conventional schemes. To test the performance, the laser beam that emerges from the setup shown in figure 21 is focused onto another PPLN crystal for a second independent out-of-loop CE phase measurement (see fig. 32).

Since the chirped mirror used as a dichroic mirror has some reflectivity around 600 nm, the beat signal generated in the first crystal can be still observed at the second detection system, rendering an out-of-loop measurement with SHG phase-matching impossible. On the other hand, in the near-infrared region (>1350 nm), the beat signal generated in the first crystal has completely disappeared after several reflections off the chirped mirrors and is thus not observable at the second f_{CEO} detector. Therefore, the out-of-loop measurement is performed only with the near infrared output, i.e. DFG phase-matching.

The relative phase of the offset frequency as detected by the two independent f_{CEO} detectors was measured. To this end, the first detector was used to lock the beat to an rf reference at 12.5 MHz and the signal of the second f_{CEO} detector was compared to the same reference.

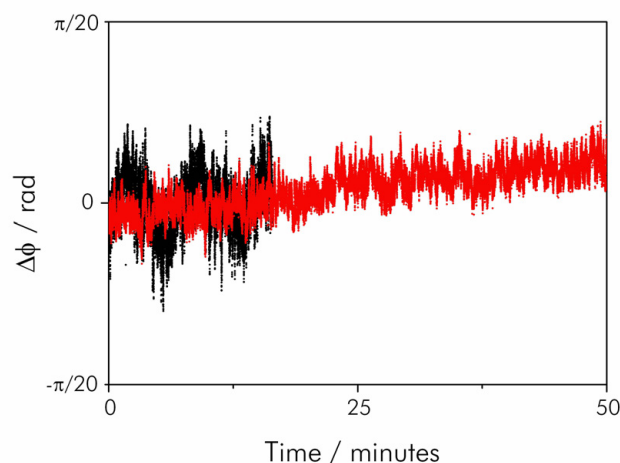


Figure 33. Typical phase deviations as recorded with the vector voltmeter (black dots), respectively the voltmeter after mixing (red dots). The rms phase jitter is 5 mrad (black), respectively 8 mrad (red).

Slow drifts of the CE phase in the spectral range of 0.2 mHz – 1 Hz were detected by recording the phase error between the reference signal at 12.5 MHz and the out-of-loop beat signal with a vector voltmeter (HP8405A, Hewlett Packard Corp.). For observing the fast jitter (frequency range 1 Hz – 35 MHz) of the CE phase, the signal of the second f_{CEO} detector was monitored by a digital oscilloscope. For the intermediate frequency region (frequency range 1 mHz – 10 Hz), the beat signal was electronically mixed with the reference and the dc signal recorded with a voltmeter. The oscilloscope and the reference frequency generator were both referenced to a high-quality quartz clock (OCXO8607, Oscilloquartz SA). This procedure permits to accurately measure the temporal variation of the CE phase, $\varphi(t)$. Typical slow-drift phase deviation traces are shown in figure 33.

As a first criterion for CE phase stability, the Allan variance σ_A^2 was computed from the phase noise data [102]

$$\sigma_A^2 = \frac{1}{2(M-1)} \sum_{k=1}^{M-1} (\bar{\varphi}_{k+1} - \bar{\varphi}_k)^2 \quad \text{with} \quad \bar{\varphi}_k = \frac{1}{\tau} \int_{t_k}^{t_k+\tau} \varphi(t) dt, \quad \text{Eq. 14}$$

where M is the total number of measurement points, and τ the gate time used for averaging. The result is shown in figure 34. A linear fit in the double-logarithmic plot shows an exponent of $\tau^{-1.05}$, close to the theoretically expected value of τ^{-1} for white flicker noise. As even for high frequencies the actual data is close to the expected values, small additional phase noise can be assumed in this region. This is important, because large phase noise above the bandwidth of the locking electronics would compromise the CE phase stability unavoidably.

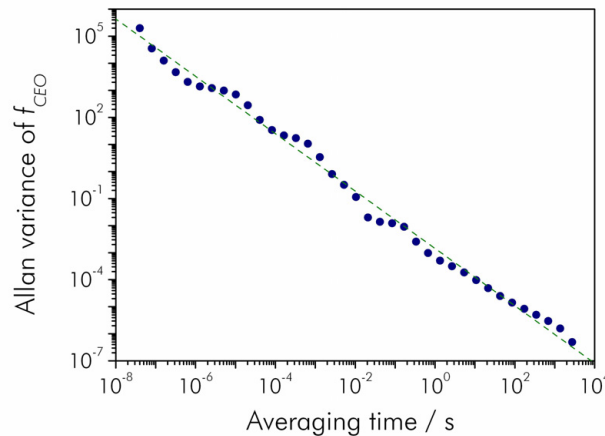


Figure 34. Standard Allan variance of f_{CEO} noise as derived from the out-of-loop measurement. The dashed line shows a linear fit to the data with an exponent of $\tau^{-1.05}$.

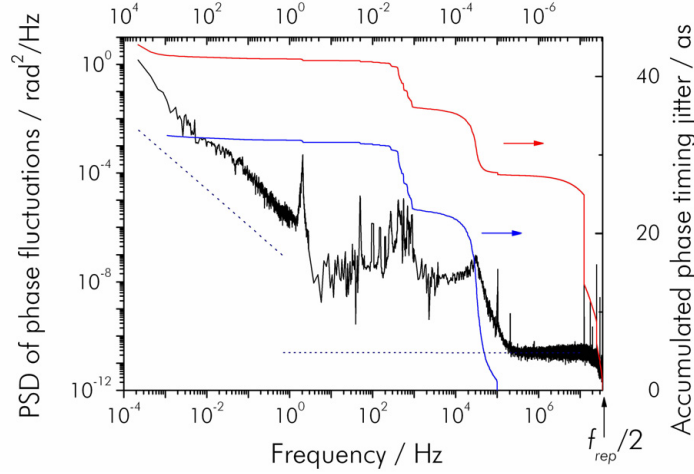


Figure 35. Out-of-loop two-sided phase noise power spectral density (PSD), $S_\phi(\nu)$ and integrated CE phase timing jitter. The red (blue) line shows the integrated phase jitter in the range of 0.2 mHz to 35 MHz (0.9765 mHz to 102.4 kHz) and results in an rms timing jitter of 99 mrad (72 mrad) or 44 as (32 as) in that range. The dotted line shows the noise floor of the photo detector and the vector voltmeter for low frequencies. The large peaks in the high frequency region originate from rf pick-up.

The two-sided power spectrum of phase fluctuations, $S_\phi(\nu) d\nu$, which is the absolute square of the Fourier transform of the CE phase noise as derived from the recorded time series, is shown in figure 35. The lowest resolved frequency component is given by the inverse of the observation time of 75 min. Since the CE phase advance is only measurable when a pulse arrives (fig. 23), the pulse train samples the f_{CEO} signal and the largest possible Fourier spectrum of the jitter of the CE phase extends to $f_{rep}/2$ according to the Nyquist theorem.

The accumulated timing jitter T_{rms} as a function of the observation time τ_{obs} ,

$$\Delta T_{rms}(\tau_{obs}) = \frac{\lambda_c}{2\pi c} \Delta \varphi_{rms}(\tau_{obs}) = \frac{\lambda_c}{2\pi c} \sqrt{2 \int_{1/\tau_{obs}}^{f_{rep}/2} S_\phi(\nu) d\nu} \quad \text{Eq. 15}$$

is also shown in figure 35. Here, $\varphi_{rms}(\tau_{obs})$ denotes the integrated CE phase error and λ_c the center wavelength of the pulses. The phase error integrated from $f_{rep}/2 = 35$ MHz to 0.2 mHz is $0.016 \cdot 2\pi$ rad, or 44 as of timing jitter at the center wavelength of ~ 830 nm. For frequencies above 200 kHz, the CE phase noise is lower than the current noise floor set by the photo detector. Nevertheless, these data set an upper limit to the CE-phase noise in the accessed spectral range.

By use of a conventional f -to- $2f$ scheme with microstructure fiber, phase-stabilization with very small timing jitter was also demonstrated earlier [103, 104]. However, only the phase stability of a single phase-locked loop was measured (in-loop measurement) [105]. Two other reports show timing jitter measurements from two separate phase

locking loops (out-of-loop). In ref. [98], a timing jitter of <100 as was reported. However, the observation time in this study was too short (4 ms) to be relevant for applications, where signal accumulation over many laser pulses (several minutes) is necessary. Another report, ref. [105] claims approximately 310 as timing jitter in a 0.9765 mHz – 102 kHz frequency band. With the same integration time (from 102.4 kHz to 0.9765 mHz) as used in ref. [105], the integrated phase error would be $0.011 \cdot 2\pi$ rad, corresponding to 32 as of timing jitter and constituting a one order of magnitude improvement. The most significant difference appears in the low-frequency region (<10 mHz), where amplitude-to-phase coupling in the microstructure fiber is dominant, as mentioned in chapter 2.3.2. A thorough literature study did not reveal another out-of-loop characterization of CE phase stabilization without fiber broadening, i.e. using directly the ultra-broadband spectrum from an oscillator [63-66, 88].

2.4 Long-cavity chirped-pulse oscillators

One of the thrusts of research with femtosecond Ti:sapphire oscillators is the increasing of the output pulse energy. Conventional oscillators are limited to just a few nanojoules pulse energy. The fundamental limitation for increasing the output pulse energy is the onset of instabilities such as satellite pulse formation, multiple-pulsing and cw generation when increasing the pump power. These occur due to excess nonlinearities (overly strong Kerr phase shift (SPM)) originating from high peak intensities in the gain medium as the pulse energy increases.

In order to produce more energetic pulses, different kinds of external laser amplifier systems can be employed. The most widely spread technique of chirped pulse amplification is presented in chapter 3. Yet, a lower repetition rate is traded in for higher pulse energies. A way of maintaining the oscillator repetition rate during amplification is discussed in chapter 4. Still, increasing the pulse energy directly provided by the oscillator is a desirable accomplishment.

An alternative developed in recent years is to extend the length of the laser cavity to reduce the repetition rate and increase the per-pulse energy while keeping the average output power constant. A multi-pass delay telescope (1:1 Herriott-type) that leaves the q parameter of the original cavity invariant is inserted to increase the cavity length [106]. In this way, the cavity stability range and the alignment sensitivity remain unchanged. To keep Kerr nonlinearities due to high peak intensities at bay, high output coupling (25 – 30%) and increased beam spot sizes in the crystal are employed.

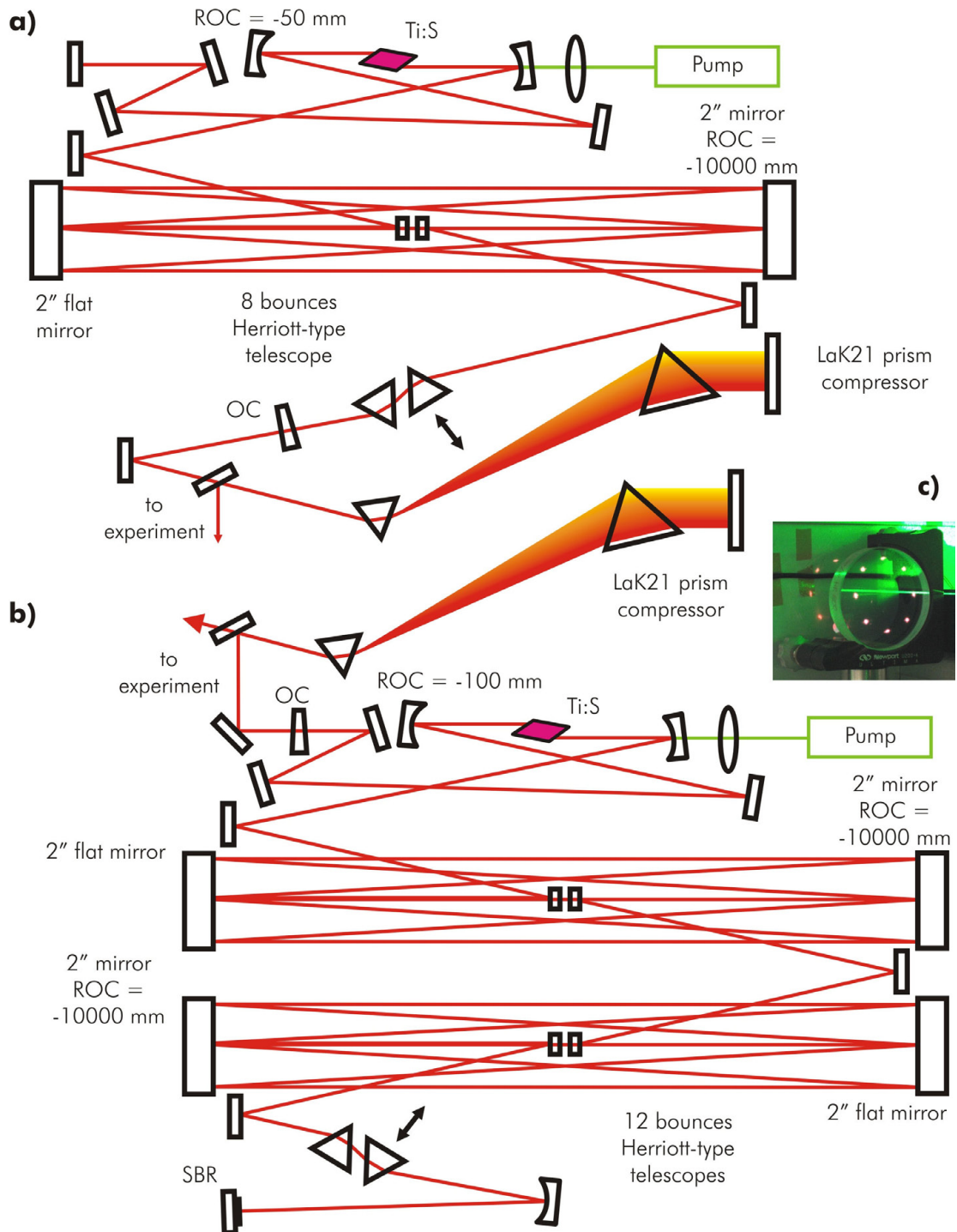


Figure 36. Cavity configuration of the 10 MHz (a) and 2.75 MHz (b) chirped-pulse oscillator. (c) shows the beam spots on the delay line mirrors. Ti:S: Ti:sapphire crystal, 3 mm thickness, absorption length $\alpha = 3.7 \text{ cm}^{-1}$; Pump: frequency-doubled Nd:YVO₄ cw laser with 10 W output power at 532 nm wavelength (Verdi V10, Coherent Inc.); SBR: saturable Bragg reflector (Batop GmbH); OC: output coupler, 30% transmission (Optilab Kft.).

Furthermore, two approaches for the dispersion regime are pursued: The first concept balances the enhanced SPM by large net *negative* intra-cavity dispersion [107, 108] and allowed the generation of 150 nJ pulses at 5.85 MHz repetition rate. The main advantage is the generation of near-chirp-free pulses directly from the oscillator. Yet, a trade-off between pulse energy and duration seems to exist due to the soliton-like pulse formation. The second concept to be presented here uses a small amount of net *positive* intra-cavity dispersion [109, 110]. In the positive dispersion regime, the pulse in the cavity is broadened to picosecond duration (~ 1.5 ps) by the combined action of positive group delay dispersion and self phase modulation. Scaling to higher pulse energies is feasible, as the pulse broadens increasingly with increasing pulse energy [111]. However, higher intra-cavity pulse energies require higher nominal values of dispersion. Compression of the heavily chirped pulses external to the cavity is required and has resulted in sub-40 fs pulses of 500 nJ energy at 2 MHz [110].

In the positive dispersion regime, generally speaking, starting mode-locked operation becomes more difficult, as the Kerr-lensing mechanism in the crystal is weaker. Therefore, in most of the low-repetition systems (5 MHz or lower), Kerr-lens mode-locking is supported by a saturable semiconductor Bragg reflector (SBR, SESAMTM) [50]. In fact, saturable absorption in the SBR dominates over Kerr-lensing as the prevailing self-amplitude modulation mechanism. Introducing an SBR to the cavity makes the oscillator easier to start and more stable over the long run. However, the relatively narrow bandwidth (in terms of reflectivity and low dispersion) of the SBR of around 40 nm limits the achievable pulse duration to ~ 30 fs with perfect pulse compression. Additional drawbacks are their high losses and the degradation over time.

The schematics of two long-cavity oscillators with 10 and 2.75 MHz, respectively, are shown in figure 36. They contain one, respectively two, Herriott telescopes. The distance between the telescope mirrors can be determined according to [112]

$$d = \frac{R}{2} \left(1 - \cos \left(\frac{\pi \mu - 1}{2 \mu} \right) \right), \quad \text{Eq. 16}$$

where a configuration of one flat and one curved mirror with radius of curvature R is assumed. The integer μ represents the number of bounces on one mirror (single pass). The cavities consist of chirped mirrors that compensate for the dispersion of the crystal, intra-cavity prisms and air. A pair of small Brewster-angled fused silica prisms with small separation allows for the fine tuning of the dispersion by adjusting their insertion into the beam. The pulses from the oscillator were recompressed in a double-prism compressor.

2. Ultra-broadband oscillators

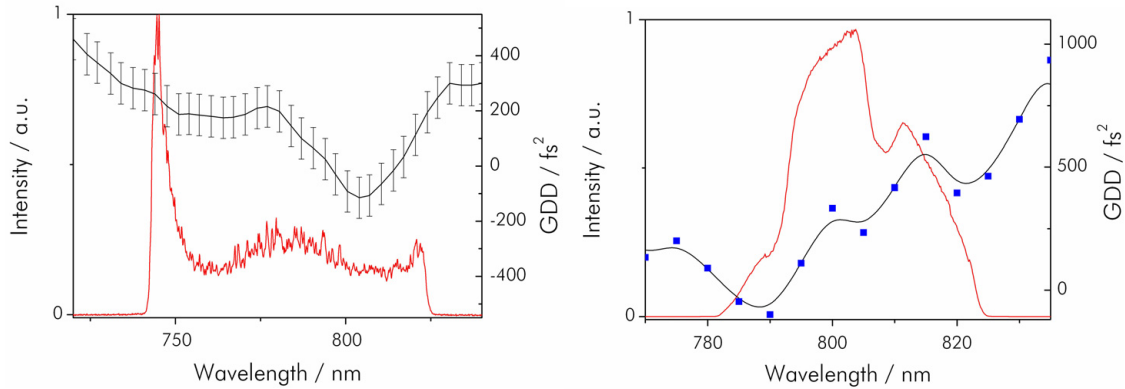


Figure 37. Spectra and net intra-cavity second-order dispersion of the long-cavity oscillators. The net dispersion is the sum of the GDD contributions in the cavity. **(a)** 10 MHz oscillator; **(b)** 2.75 MHz oscillator.

The 10 MHz system was set up to seed the enhancement cavity presented in detail in chapter 4. It yields 135 nJ pulses at 8 W pump power with a duration of approximately 35 fs. The oscillator operating at 2.75 MHz was built to seed a cw two-pass amplifier, presented in the next chapter. It generates 360 nJ pulses at 9 W pump power with ~ 40 fs duration. For both systems, increasing the pump power beyond 9 W caused instabilities to develop, such as cw background or pulse break-up. The intra-cavity dispersion and output spectra of both systems are shown in figure 37. The positive dispersion regime is characterized by rectangular spectra with relatively sharp edges. Theory predicts M-shaped spectra (with Kelly side bands) for nominal dispersion close to zero.

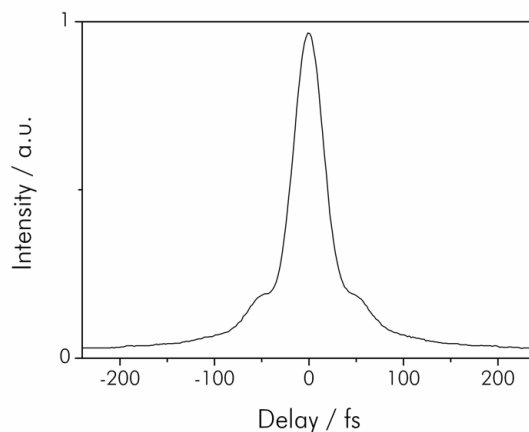


Figure 38. Intensity autocorrelation of the 10 MHz oscillator, measured with a second-order autocorrelator (Pulse Check 15, APE GmbH). The FWHM pulse duration is 35 fs with a transform-limit of 25 fs.

For more positive dispersion, the spectral shape changes to flat-top. An intensity autocorrelation trace is shown in figure 38. Side wings to the main pulse originate from uncompensated (higher-order) chirp. Despite their enormous cavity length (110 m and 30 m, respectively), with proper environmental shielding, both systems operate for hours without power degradation. However, with regard to high-repetition-rate oscillators operating in the negative dispersion regime, both oscillators displayed increased fluctuations of the chirp of output pulses over time. Small changes of the nominal value of the intra-cavity dispersion (e.g. path length changes through the intra-cavity prisms) show a strong effect on the output spectrum, and therefore the pulse chirp.

2.4.1 Double-pass post-amplifier

Despite the high pulse energies available from chirped-pulse oscillators, further amplification is a worthwhile goal. Here, a simple, compact post-amplifier for pulses at megahertz repetition rates is presented. It closes the gap between laser oscillators and high-power chirped-pulse amplifier systems (chapter 3) both in terms of repetition rate and pulse energy.

Seed picosecond pulses from a long-cavity oscillator are amplified in a Ti:sapphire crystal in a double-pass geometry (see fig. 39). A Faraday isolator together with a polarizing beam splitter serves as a passive switch to separate the amplified light pulses from the incoming seed pulses. In order to reach efficient gain in a double-pass configuration, it is necessary to induce strong population inversion. Very tight focusing of the pump and seed beams is mandatory, as well as a gain crystal with very high doping concentration.

The seed pulses from the long-cavity oscillator are focused to the Brewster-angled crystal and retro-reflected and refocused by spherical mirrors. By appropriate adjustment of the Faraday isolator and half-wave plate, the returning light is selected by means of its polarization and coupled out by the polarizing beam splitter.

The amplifier crystal is pumped with up to $2 \cdot 20$ W of cw light at a wavelength of 515 nm from a frequency-doubled thin-disk Yb:YAG pump laser (MonoDisk-515 Gemini, ELS GmbH). Ti:sapphire crystals with very high doping of $\alpha = 9 \text{ cm}^{-1}$ are available [113], however with increased doping concentration, the figure-of-merit $FOM = \alpha_{515}/\alpha_{800}$ becomes worse. Ti:sapphire has higher absorption at 515 nm than at 532 nm, the wavelength generated by more readily available Nd:YVO₄ pump sources. The pump laser offers two output beams which are used to pump the crystal from both sides. The pump light is focused by lenses to a beam waist diameter of approximately 80 μm . With such high pump powers and tight focusing, thermal issues such as thermal lensing and thermally induced distortions might arise in the amplifier crystal.

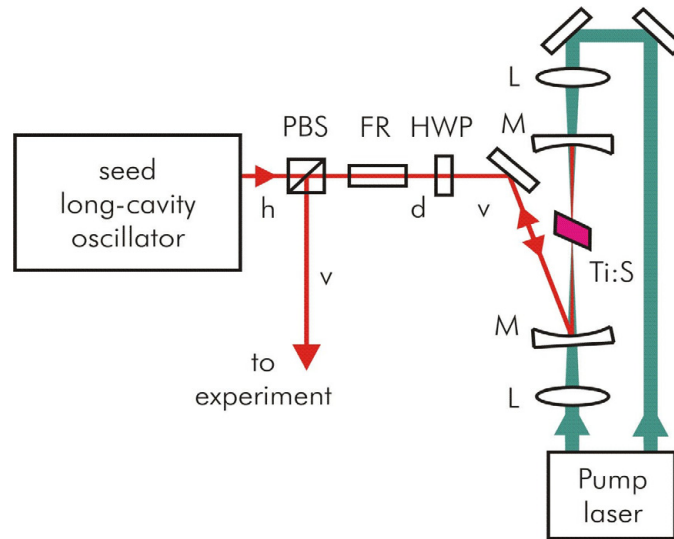


Figure 39. Schematics of the cw-pumped double-pass post-amplifier. h, v, d denote horizontal, vertical and diagonal (45°) polarization. PBS: polarizing beam splitter; FR: Faraday rotator (EOT Inc.); HWP: half-wave plate; Ti:S: highly-doped Ti:sapphire crystal, $t = 3$ mm, $\alpha = 7.42 \text{ cm}^{-1}$ at 514 nm (Crystal Systems Inc.) mounted on a cryostat finger in a vacuum housing (Oxford Instruments plc.); L: lens, focal length 120 mm; M: spherical mirror, ROC = -150 mm; Pump laser: frequency-doubled thin-disk Yb:YAG cw laser (MonoDisk-515 Gemini, ELS GmbH).

Thermal lensing is particularly dangerous, as it causes a reduction of the amplified mode spot size, eventually resulting in optical damage. It could in principle be compensated for, but aberrations and distortions in the wave front are difficult to correct. In order to avoid the formation of thermal lensing in the crystal [114], it is cooled by a liquid nitrogen cryostat to 100 K. This has the benefit that the thermal conductivity of the Ti:sapphire crystal increases dramatically upon decreasing the temperature [115] and the temperature-dependence of the refractive index (n/T) decreases upon decreasing the temperature [116]. Furthermore, the upper-state lifetime of the Ti^{3+} ions increases with decreasing temperature, which is beneficial for the efficiency of the gain process.

Previous studies [117] with a similar setup have shown an amplification factor of ~ 9 , albeit with 10.5 W of pump light at 532 nm and the crystal being at 232 K.

The combination of long-cavity chirped-pulse oscillators and a cw-pumped amplifier will enable the generation of microjoule pulses at megahertz repetition rates. Such a compact light source may find application, e.g. in the generation of sub-femtosecond electron pulses [118] or for coincidence experiments, as well as industrial applications, like machining on sub-micrometer scale and waveguide writing [56, 57, 119].

2.5 Conclusions

Recent progress, in particular in chirped mirror design and manufacturing, has resulted in the generation of ultra-broadband spectra directly from Kerr-lens mode-locked oscillators. As a consequence, CE phase stabilization methods emerged that do not require spectral broadening by a microstructure fiber. This has many benefits, amongst them are less cumbersome handling (no coupling into a tiny fiber core), smaller phase noise due to reduced amplitude to phase coupling, and most importantly the fact that phase detection is possible directly in the beam used for experiments. In this chapter CE phase stabilization by means of difference frequency generation in a single nonlinear crystal was presented. The monolithic setup that essentially avoids the alignment-sensitive interferometer allows for CE phase stabilization with very small phase jitter. Indeed, a thorough characterization of the CE phase noise in an out-of-loop measurement revealed an order of magnitude improvement over previously achieved results.

Further improvements to this offset frequency stabilization technique could originate from broader spectra from the oscillator with more power in the spectral wings, one octave apart. This would result in improved nonlinear interaction, a stronger beat note and hence better phase stability. Further improvements of the spectral bandwidth of Ti:sapphire oscillators might come from more precise characterization techniques for the dispersion of chirped mirrors [75, 76] or the use of specially designed output couplers. Also in the time domain, better dispersion compensation and in particular smaller GDD oscillations would result in less energy in the pulse pedestal and in smaller satellite pulses.

Additionally, the use of waveguides written into the nonlinear crystal could improve the phase-matching, as well as the spatial mode of the beam.

The concept of generation of SPM and DFG light, and their subsequent interference, in a single nonlinear crystal is very flexible. Thus, it can be applied to laser systems in other wavelength regions simply by changing the poling period of the crystal. This was demonstrated recently with an erbium-doped fiber laser [35].

The development of long-cavity chirped-pulse oscillators has at its focus the increase of the pulse energy while maintaining a repetition rate in the megahertz range. This is achieved by reducing the repetition rate by cavity extensions and the temporal stretching of the pulses. As the pulse energy in the positive dispersion regime appears to be limited ultimately only by the available pump power, breaking the microjoule frontier in the near future seems possible. Especially in combination with a cw-pumped post-amplifier, a compact system will be available that produces pulses with several microjoules energy at a repetition rate not available from common amplifier systems. Tight focusing of these pulses down to a spot size of a few micrometers can produce intensities of more than 10^{13} W/cm² [112]. This is sufficient for nonlinear conversion to the XUV region, resulting in a compact coherent XUV source at megahertz repetition rates.

Chapter 3

Few-cycle chirped-pulse amplifier systems

Studying strong-field phenomena requires ultrashort pulses with per-pulse energy typically on the order of hundreds of microjoules. One of the most widely studied and exploited strong-field mechanisms is the generation of extreme ultraviolet (XUV), respectively soft X-ray light using high-order harmonic generation. It requires intensities of more than $5 \cdot 10^{13} \text{ W/cm}^2$ and is of highly nonlinear nature.

Presently, laser oscillators can produce these intensities only when tightly focused down to a $1 \mu\text{m}^2$ spot [110,112]. As the average power is not sufficient for producing a useful flux from the frequency conversion, master oscillator – power amplifier systems are employed. For applications in the Ti:sapphire wavelength range, mainly two options are available: amplification in a parametric process or amplification by stimulated emission. Both methods are confronted with the problem of coping with the high peak intensities inside the amplifier crystal or nonlinear conversion crystal and the accompanying detrimental nonlinearities and damage potential.

This issue is resolved by temporal stretching the pulse before the amplification stage and subsequent re-compression of the amplified pulse (fig. 40). In the case of parametric amplification, this scheme has usually been termed *optical parametric chirped pulse amplification* (OPCPA) and was demonstrated for the first time in 1992 [120]. It offers a high single-pass gain of $\sim 10^5$ over a large bandwidth of a few hundred nanometers. However, effective re-compression of the pulses is an issue with the pulse duration being limited to around 10 fs [121]. Here, amplification by population inversion and stimulated emission in a Ti:sapphire crystal is in the focal point. This *chirped-pulse amplification* (CPA) scheme was demonstrated for the first time in 1985 [122] and has found wide-spread usage from table-top systems to large-scale laser units generating pulse energies of tens of joules. Due to the relatively low single-pass gain factor of 3 to 5, several passes through the amplifying crystal are necessary.

All high-field phenomena that are driven by few-cycle pulses, e.g. high harmonic generation [11], the production of attosecond pulses [15] and above-threshold ionization [123], exhibit a CE phase-dependent behavior. This is due to the threshold-dependence of these processes and the fact that for ultrashort pulses, the exact positions and amplitudes of the electric-field extrema become sensitively dependent on the CE phase. Random shot-to-shot shifts of the CE phase prevent the reproducible steering of these processes with laser light. For instance, changing the CE phase of a 5 fs laser pulse from 0 to $\pi/2$ will change the pulse peak intensity by $\sim 7\%$. The investigation of these processes demands ultrashort amplified pulses with controlled waveform of the electric field.

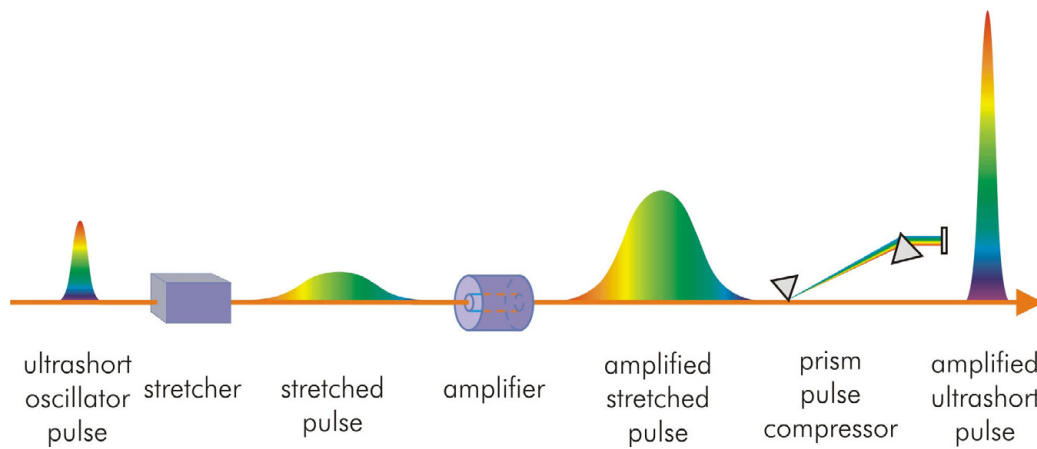


Figure 40. Principle of power amplification with prior temporal stretching and subsequent compression of the pulses.

In this chapter, a CE phase-stabilized chirped-pulse amplifier system is presented (chapt. 3.1) that makes use of the monolithic offset frequency stabilization method described in chapter 2.3. The origins of CE phase noise of the amplified pulses are described in chapter 3.1.1.

3.1 CE phase-stabilized chirped-pulse amplifier system

Generally, a chirped-pulse amplifier system consists of a seed oscillator, a stretcher, the amplifying stage and a pulse compressor [124, 125]. Due to thermal load issues, the onset of nonlinearities and the limited availability of adequate high-repetition rate pump sources for the amplifier crystal, the pulse repetition rate has to be reduced to a few kilohertz. This is achieved with a pulse picker in the amplifier stage. In order to generate pulses in the sub-10 fs regime, spectral broadening by nonlinear self-phase modulation and subsequent compression are used behind the amplifier.

A real-world sketch of such a CPA system is shown in figure 41. Ultrashort nanojoule pulses with a repetition rate of 78 MHz from a laser oscillator (as described in chapter 2.1) are temporally stretched in a block of SF57 glass. The material dispersion of the glass block and the Faraday isolator is sufficient to stretch the pulses to a duration of ~20 ps. Two pairs of chirped mirrors with specially designed third-order dispersion pre-compensate for the material dispersion of the amplifier and compressor stage. Taking into account the large bandwidth of the seed spectrum (see fig. 8) and the limited gain bandwidth of the Ti:sapphire amplifier (725 – 900 nm FWHM), only approximately 0.5 nJ of pulse energy is available for seeding.

3. Few-cycle chirped-pulse amplifier systems

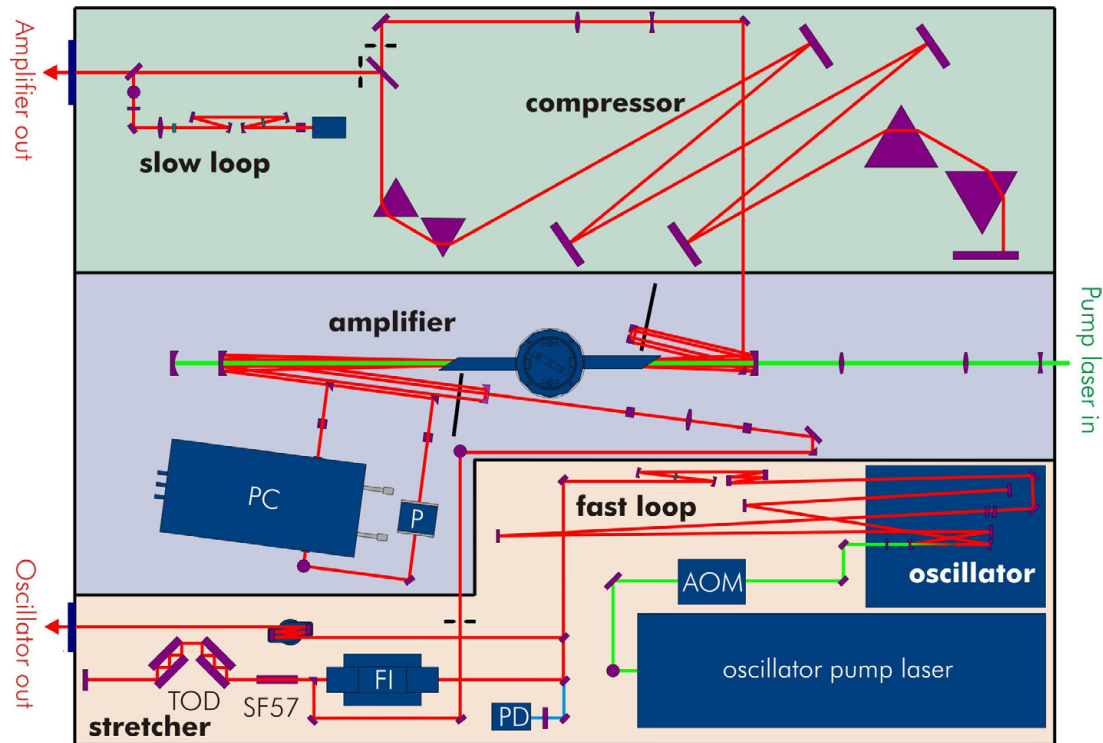


Figure 41. Schematics of the chirped-pulse amplifier (Femtopower Compact Pro CE-Phase HP/HR, Femtolasers GmbH). SF57: Brewster-angled glass block made from SF57, thickness 5 cm; FI: Faraday isolator (EOT Inc.); TOD: chirped mirrors with controlled third-order dispersion, 64 reflections; oscillator pump laser: frequency-doubled Nd:YVO₄ laser (Verdi V6, Coherent Inc.); AOM: acousto-optic modulator (AOM-405, IntraAction Corp.); amplifier pump laser: diode-pumped Q-switched frequency-doubled Nd:YLF laser (DM 30, Photonics Industries Inc.); PC: Pockels cell (LaserMetrics 5046, FastPulse Inc.); P: Berek polarizer; PD: photodiode; slow loop, fast loop: components for CE phase-stabilization (see next chapter).

After temporal shaping, the pulse train is injected into a multi-pass amplifier arrangement. In a Z-shape configuration, it consists of two curved mirrors, two retro-reflectors and a 3.5 mm-long Brewster-cut Ti:sapphire crystal. The highly doped crystal (absorption length $\alpha \approx 3.5 \text{ cm}^{-1}$ at 532 nm wavelength) is placed in a vacuum chamber and cooled by a closed-circuit methanol chiller down to -70° C (thermo-electrically stabilized) to reduce the effect of thermal lensing. Due to the deposition of heat in the crystal by the pump beam (via the quantum defect), the medium is hotter on the beam axis and a transverse temperature gradient is forming. This causes a transverse gradient of the refractive index by the thermo-optical coefficient dn/dT .

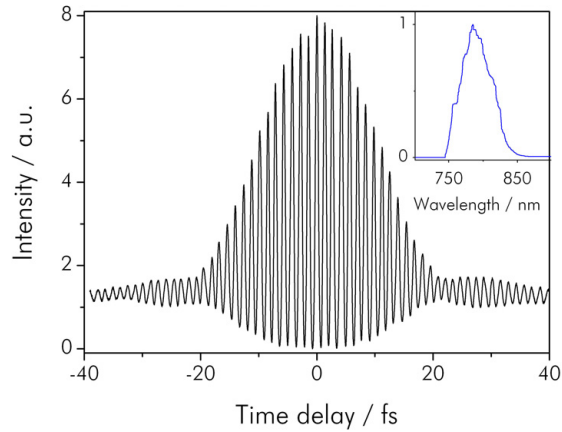


Figure 42. Interferometric autocorrelation trace of the amplified pulses after the prism compressor. The pulse width is 25.4 fs. The transform-limited pulse width as derived by inverse Fourier transform from the spectrum (inset) assuming flat phase is 17.9 fs.

In this way, some sort of lens is created, however not of perfect shape, as the heat and the thermal conductivity are not evenly distributed. Therefore the spatial beam profile is distorted and the lensing cannot be compensated easily with additional optical elements.

During the first four passes, the pulses pass through a dielectric multilayer filter with a Gaussian absorption profile (minimum transmission 20%) in the wavelength range 760 to 825 nm (FWHM). Thus gain narrowing is partially compensated for, increasing the amplified bandwidth by ~50%. After four passes through the crystal, a single pulse is selected out of the pulse train with a Pockels cell (PC) at a repetition rate of 3 kHz. In this way both the background due to amplified spontaneous emission and the susceptibility to lasing are suppressed. The Pockels cell is synchronized to the pump laser and oscillator via a divider. The selected single pulse is re-injected and amplified in another five passes. Before the last pass, the pulse is coupled-out once again and re-injected after an increase of the beam waist in the crystal by a factor of two. This allows optimization of the mode overlap of pump and seed beam, thus maximizing the energy extraction in the last pass. In addition, nonlinear effects in the gain medium are reduced, preventing phase distortions and ultimately crystal damage. Maximizing the energy extraction ensures operation of the amplifier close to saturation and therefore makes the output energy less susceptible to fluctuations of pump and seed pulses. Here, sufficient gain saturation guarantees a pulse-to-pulse energy stability of better than 1.5% rms (over 15 hours).

Pumping the amplifier stage in a double-pass configuration with 9 mJ from a diode-pumped Q-switched frequency-doubled Nd:YLF laser (DM 30, Photonics Industries Inc.) results in a pulse energy of ~1.1 mJ.

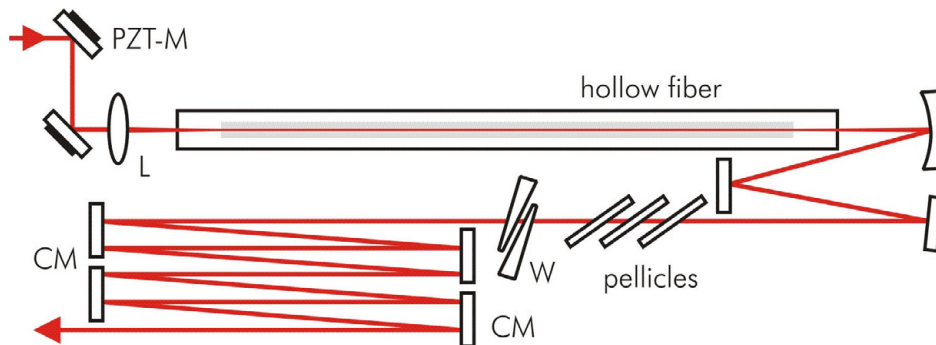


Figure 43. Hollow fiber-chirped mirror pulse compressor. W: pair of wedges; PZT-M: beam stabilizing mirrors, controlled by quadrant photodiodes; L: thin focusing lens, AR coated, focal length 1.5 m; CM: chirped mirrors with GDD of -40 fs^2 per reflection; pellicles: $5 \mu\text{m}$ thickness (National Photocolour Corp.); hollow fiber: hollow fused silica fiber ($260 \mu\text{m}$ inner diameter, 1.2 mm outer diameter, 1 m length, FiberTech GmbH) installed in a vacuum tube filled with 2.8 bar of neon.

The amplified pulses are compressed with a prism compressor consisting of two pairs of Brewster-angled fused silica prisms separated by 6 m. After passage through the prism compressor, the pulse duration is approximately 25 fs. The autocorrelation of the pulses and the corresponding spectrum are shown in figure 42. The good energy extraction efficiency in the amplifier and the high throughput of the prism compressor ($>80\%$) results in an overall efficiency (from nanosecond pump pulses into femtosecond amplified pulses) of $\sim 10\%$. The spatial profile of the amplified and compressed pulses is Gaussian and the M^2 was measured to be below 1.5.

The 25 fs, 0.85 mJ pulses from the prism compressor are injected into a hollow-core fused-silica fiber (1 m length, inner diameter $260 \mu\text{m}$; FiberTech GmbH) filled with noble gas (2.8 bar of neon) for spectral broadening by self-phase modulation (see fig. 43) [126]. The typical fiber throughput is 45 to 50%. A pair of thin wedges placed at Brewster angle at the output of the fiber introduces variable positive dispersion allowing precise control of the overall dispersion of the system. Residual ellipticity of the polarization on the order of 10% arising from non-uniform stress on the windows of the tube that houses the fiber has to be eliminated. To this end a series of $5 \mu\text{m}$ thick pellicles is introduced into the beam path at Brewster angle. They remove the vertical component of the polarization by Fresnel reflection while transmitting the horizontal polarization.

The resulting heavily chirped pulses are compressed by a set of ultra-broadband chirped mirrors. The pulses at the output of the hollow fiber-chirped mirror compressor are characterized with an autocorrelator designed for femtosecond pulses and an optical spectrum analyzer (fig. 44).

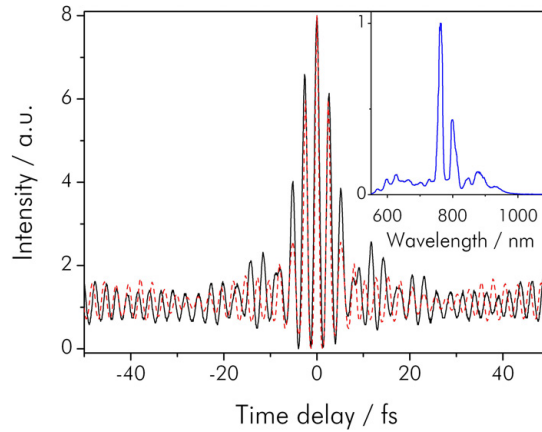


Figure 44. Characterization of the pulses from the hollow fiber-chirped mirror compressor. The dashed line shows the transform-limit autocorrelation as derived by inverse Fourier transform from the spectrum (inset) assuming flat phase. Pulse widths are 5.3 fs and 4.4 fs (FWHM), respectively.

Although for ultrashort pulses with non-Gaussian spectrum an autocorrelation trace can be considered only a good estimate for the pulse duration, a FWHM consisting of around 2 cycles indicates a pulse width of approximately 5 fs. The shift of the optical spectrum towards the blue side with regard to the seed oscillator spectrum (see fig. 8) is a consequence of pulse self-steepening.

The overall throughput of the hollow fiber-chirped mirror compressor is currently ~35%, mainly determined by the losses in the hollow fiber caused by refraction at the inner glass surface. This number could be greatly improved by the use of metal-coated hollow fibers. These fibers are commonly used as flexible waveguides for CO₂ lasers. However, recently they were also tested for the guiding of near-infrared ultrashort laser pulses. A throughput of 95%, including coupling losses, was reported for a 50 cm silver-coated hollow fiber with inner diameter of 250 μm , compared with 80% for an uncoated fiber under the same conditions. The theoretical values are 99.6% and 93.15%, respectively. The remaining losses are due to scattering from the silver surface roughness. Also, spectral broadening with gas-filled metal-coated hollow fibers was performed: with 250 μJ pulses of 110 fs duration, the broadening was similar ($\lambda = 53$ nm) to the one reached with standard fused silica fibers [127]. In this configuration, the pulse energy could be increased up to 500 μJ without damaging the fiber [128]. The reflectivity of the glass surface can be increased even further by coating several $\lambda/4$ -layers of a dielectric (polymer, CdS, PbS) on top of the inner metal layer. The thin films are applied with a liquid-phase deposition technique that has been shown to work even for 250 μm bore waveguides [129].

3. Few-cycle chirped-pulse amplifier systems

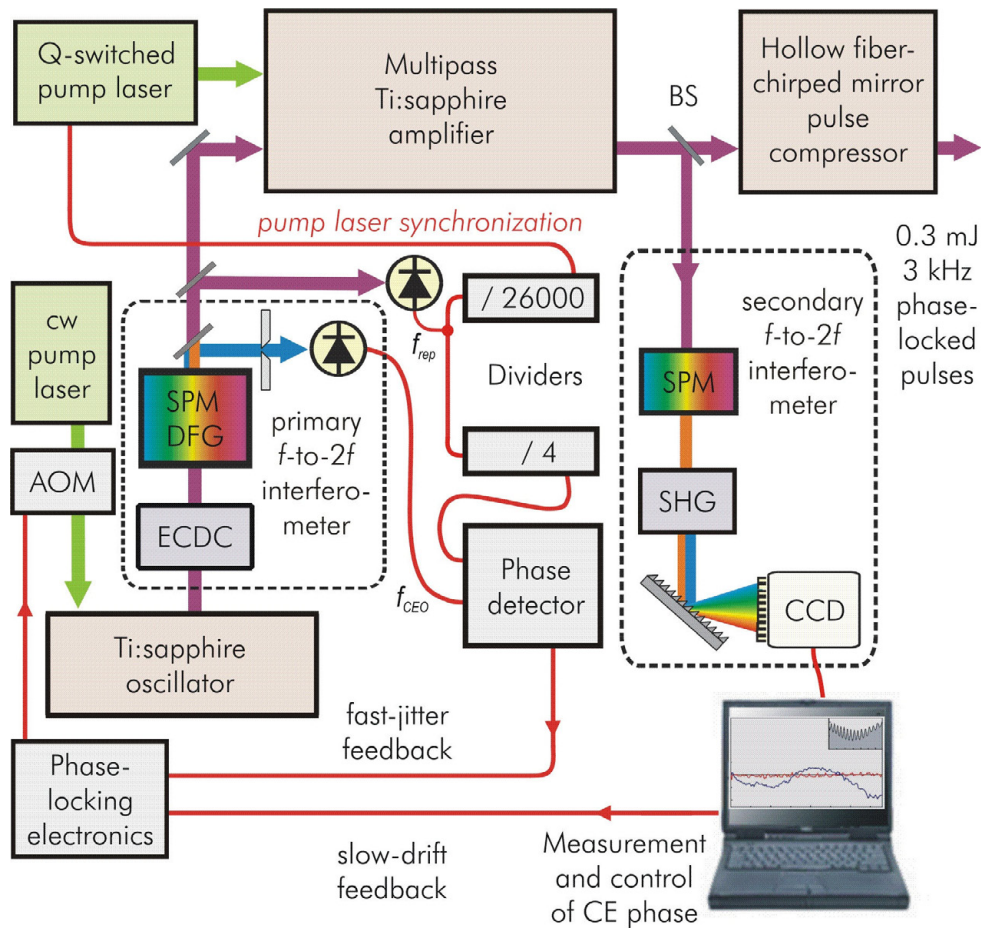


Figure 45. Schematics of the CE phase-stabilized amplifier setup with the two phase-locking loops shown. AOM: acousto-optic modulator; ECDC: extra-cavity dispersion control by chirped mirrors; SHG: second harmonic generation; CCD: charge coupled device camera, integrated in an optical spectrum analyzer; BS: beamsplitter, 0.7%.

With an Ag/polymer-coated hollow fiber of 700 μm inner diameter, 196 fs pulses were transported with energy of 700 μJ [130]. Pulses with a duration of 150 fs and energy of more than 1 mJ were transmitted with these fibers without damaging them [131]. First own tests with a silver-coated hollow fiber of inner diameter 250 μm (outer diameter 360 μm) resulted in the destruction of the fiber. Using the proven fused silica waveguides as substrates for a silver and/or dielectric could improve the throughput by more than 20%.

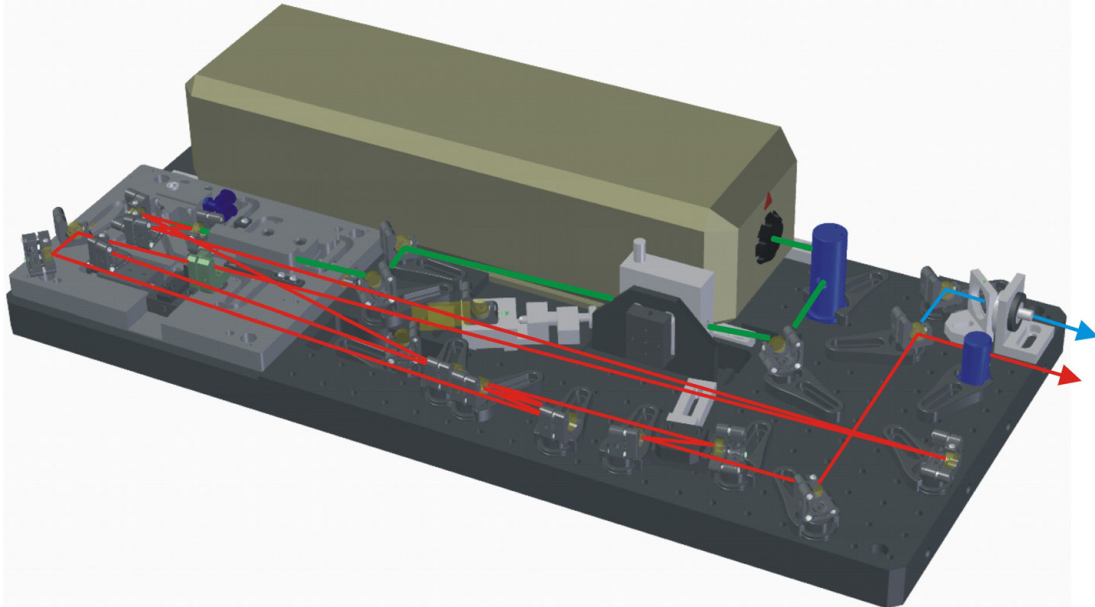


Figure 46. Computer drawing of the ultra-broadband oscillator with CE phase stabilization by DFG (Femtosource Rainbow, Femtolasers GmbH). The extension of the water-cooling of the pump laser base plate to the whole oscillator breadboard aims at lower intensity and CE phase noise. The compact footprint, 70 by 32 cm, helps to integrate the CE phase-stabilized oscillator in the standard amplifier housing.

The preceding description related merely to a standard chirped-pulse amplifier system. In the following, CE phase-stabilization of this system is the issue. It requires more effort than merely stabilizing the offset frequency of the seed oscillator as described in chapter 2, as the phase characteristics of the seed pulse are not necessarily preserved during the amplification process. Figure 45 shows an overview of the CE phase-stabilized amplifier.

An ultra-broadband oscillator, including the offset frequency stabilization with a monolithic crystal (cf. chapt. 2.3), is integrated in the amplifier system described above (see fig. 46). The stabilization method using difference frequency generation in a monolithic crystal commends itself as the full oscillator output power (neglecting refraction losses from the crystal) is available for seeding, i.e. no beam-splitting for the CE phase-stabilization unit is required. In contrast to microstructure fibers, the dispersion introduced by the nonlinear PPLN crystal can be compensated for. Inserting the PPLN into the beam path between seed oscillator and stretcher does not change (after re-alignment) the characteristics of the pulses after the prism compressor (see fig. 42) or after the fiber compressor (see fig. 44). The collinear setup and a temperature-stabilized base plate help reducing intensity and phase fluctuations from the oscillator.

3. Few-cycle chirped-pulse amplifier systems

As the pulses from the seed oscillator are reduced in repetition rate by the pulse picker (Pockels cell) in the amplifier, only every n -th seed pulse has to have the same CE phase. This simplifies the efforts necessary to produce waveform-controlled amplified pulses. Rewriting equation 7 as

$$\Delta\varphi = 2\pi \frac{f_{CEO}}{f_{rep}}, \quad \text{Eq. 17}$$

it becomes clear that the CE phase shift φ only depends on the ratio of f_{CEO} and f_{rep} . Therefore, stabilizing f_{CEO} to a value equal to a fraction of the repetition frequency f_{rep} ($f_{CEO} = f_{rep}/n$) will cancel out noise on f_{rep} and result in a pulse train in which every n -th pulse carries the same CE phase. If every n -th pulse is selected by the pulse picker, a train of pulses with identical electric field waveform is produced. In the given system, $f_{rep} = 78$ MHz and the pulses are picked with a rate of 3 kHz, which means that $n = 26000$. In practice, the beating signal of the oscillator phase stabilization is locked to f_{rep} , electronically divided by 4 (cf. fig. 45). This ensures that every 26000-th pulse has identical CE phase.

During amplification and compression, additional phase noise is added to the pulse train. The origins of these fluctuations are explained in detail in the next chapter. Yet, this additional CE phase fluctuation occurs on a slow timescale, i.e. on the order of tens of milliseconds and can be compensated.

Detection and correction of the additional slow CE phase noise is achieved by means of a secondary phase-locking loop (see fig. 47), based on f -to- $2f$ spectral interferometry [14]. Due to the lower repetition rate compared with the oscillator, the CE phase is sampled less frequently and information on the phase excursions is scarce.

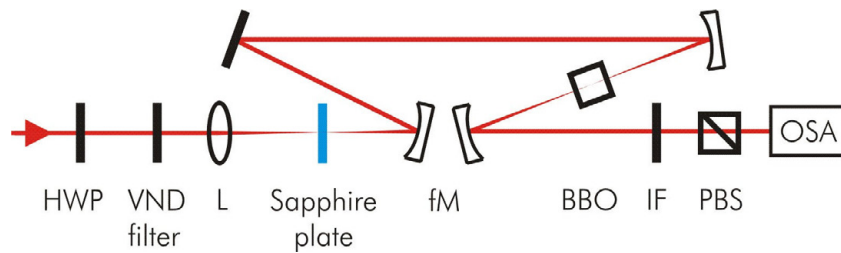


Figure 47. Setup of the secondary CE phase detection after the prism compressor. HWP: half-wave plate; VND filter: variable neutral density attenuator; L: lens, focal length 75 mm, broadband-AR coated; BBO: β -Barium borate frequency-doubling crystal (1 mm thickness, type I phase-matched, broadband-AR coated, EKSPLA Inc.); Sapphire plate, 2 mm thickness, c -cut (Korth Kristalle GmbH); fM: focusing mirror, ROC = -50 mm; IF: interference bandpass (325 – 640 nm FWHM) filter (FGB37, Thorlabs Inc.); PBS: polarizing beam splitter (GL5-A, Thorlabs Inc.); OSA: optical spectrum analyzer (S2000, Ocean Optics Inc.).

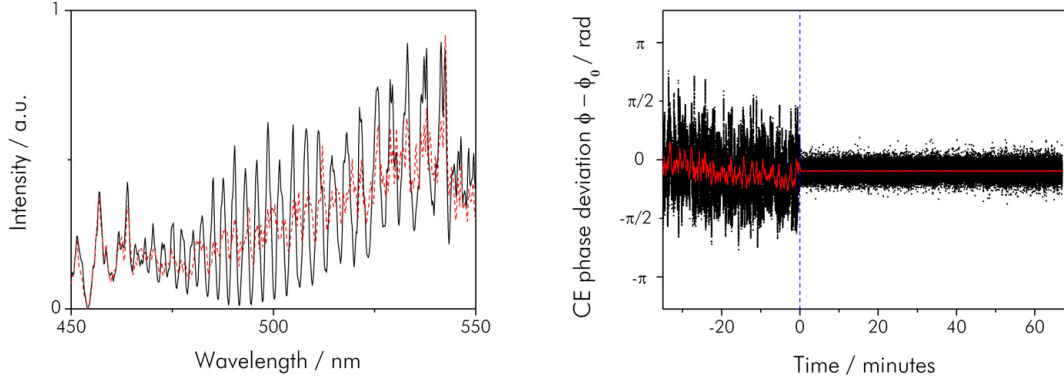


Figure 48. (a) f -to- $2f$ interference spectrographs recorded from the secondary interferometer, when oscillator phase-locked (solid black line) and free running (dashed red line). Integration time 20 ms. (b) Phase deviations as derived from the f -to- $2f$ interference pattern by the Fourier transform algorithm. The secondary feedback loop was put in operation at $t = 0$. The red line shows an average over 7 ms of the data. Root mean square jitter of the locked (unlocked) part of the trace is 149 mrad (678 mrad), in 0.24 mHz – 15 Hz bandwidth.

Therefore, in contrast to the narrowband detection principle employed in the oscillator, a broadband version of the self-referencing scheme has to be used. On the other hand, the high pulse energy simplifies the generation of an octave spanning spectrum, essential for the f -to- $2f$ self-referencing technique. For this purpose a small fraction (<1% of average power) of the beam is split off from the main beam after the prism compressor (see fig. 41) for a secondary interferometric CE phase detection. In the interferometer, an octave-spanning spectrum is generated in a sapphire plate. This continuum is then focused into a frequency-doubling crystal (BBO) and detected with a spectrometer. Appropriate spatial, spectral, and polarization filtering yields an interference pattern in the region of spectral overlap between the short wavelength wing of the fundamental spectrum and the second harmonic signal near $\lambda \sim 490$ nm according to

$$I(\omega) = I_{WL}(\omega) + I_{SH}(\omega) + 2\sqrt{I_{WL}(\omega)I_{SH}(\omega)} \cos(\omega\tau_0 + \varphi + \varphi_0) \quad \text{Eq. 18}$$

where $I_{WL}(\omega)$ and $I_{SH}(\omega)$ are the white-light and second harmonic spectrum, respectively, τ_0 the time delay between the two components, φ the CE phase and φ_0 an unknown phase shift due to dispersion in the frequency-doubling crystal.

As expected, the averaged spectrum shows a fringe pattern with high visibility when the seed oscillator is phase-locked (fig. 48a). Both timing jitter (frequency independent), as well as phase fluctuations (frequency dependent) blur the fringes. The slow phase drifts are extracted from the averaged spectrographs by a linear Fourier-

transform spectral interferometry algorithm [132]. This procedure consists of Fourier transforming into the time domain, applying a bandpass filter around $t = \tau_0$ and another Fourier transformation back to the frequency domain. To correct for these slow phase fluctuations, negative feedback by means of a voltage proportional to the phase deviation is given to the locking electronics of the seed oscillator (see fig. 45). Due to the good passive phase stability, the necessary feedback corrections are small and the system stays phase-locked for hours. Figure 48b shows typical phase deviations recorded over 67 minutes in the described manner with both feedback loops in operation. The resulting rms jitter is 149 mrad or 60 as in 0.24 mHz – 15 Hz bandwidth. However, care must be taken, as this does not represent the real fluctuations of the CE phase, as it is recorded within the locking loop (in-loop measurement). As such, it only shows the effectiveness of the stabilization circuitry (cf. chapt. 2.3.4). The upper limit of the CE phase drift at the output of the amplifier system could be obtained with an additional, out-of-loop interferometer.

3.1.1 Origins of CE phase noise of amplified pulses

Fluctuations of the CE phase of amplified ultrashort pulses can originate from many sources in the complex amplifier system.

Basically, all of the components of the amplifier system contribute to the CE phase noise of the output pulses. In the following, the building blocks and their noise sources will be treated one after the other.

Firstly, phase noise from the seed oscillator is transferred directly to the output. Noise components above the picking frequency of 3 kHz are written onto the picked pulse sequence and can therefore not be neglected. The picking of every P -th pulse in the amplifier stage can be understood as a sampling of the seed oscillator CE phase and is therefore subject to what is called *aliasing* in signal processing [4]. Due to the periodic nature of the pulse train, the CE phase error of the n -th seed pulse can be written as a Fourier series. It can be represented by the two-sided *power spectral density* (PSD, also see fig. 35),

$$S_k^\psi = \frac{T_r}{N} |\hat{\psi}_k|^2 \quad \text{Eq. 19}$$

where T_r is the temporal spacing between pulses, N the total number of pulses considered and $\hat{\psi}_k$ the Fourier component corresponding to frequency $\omega_k = 2\pi k/NT_r$. The highest frequency appearing is half the repetition frequency of the seed oscillator, which is the *Nyquist frequency* $\omega_{\text{Nyq}} = 2\pi N/2NT_r = \omega_{\text{rep}}/2$. The integral of the PSD is the rms noise value in a certain bandwidth. In an analogous manner, the CE phase error

of the m -th picked pulse (corresponding to the $P \cdot m$ -th seed pulse) can be expressed in terms of the Fourier components of the original pulse train. Comparing the two expressions, re-numbering indices and averaging yields the PSD of the picked pulse train

$$\langle S_l^\Phi \rangle = \left\langle \frac{T_r}{N} \left| \sum_{j=0}^{P-1} \hat{\psi}_{jM+l} \right|^2 \right\rangle = \frac{T_r}{N} \sum_{j=0}^{P-1} \langle |\hat{\psi}_{jM+l}|^2 \rangle = \sum_{j=0}^{P-1} \langle S_{jM+l}^\Psi \rangle, \quad \text{Eq. 20}$$

where M is the total number of picked pulses, $N = P \cdot M$.

The highest frequency component that appears is now $2\pi M/2NT_r = \omega_{rep}/2P$, which is the Nyquist frequency of the picked pulse train. However, the PSD in equation 20 still contains contributions of all higher frequencies of the spectrum of the original pulse train aliased to frequencies below $\omega_{rep}/2P$. Aliasing always happens if a function that is sampled at discrete times contains Fourier components higher than the Nyquist frequency determined by the sampling rate.

The major point to note is that the phase noise PSD of the original pulse train is moved block-wise into the Nyquist range of the picked sequence and stacks up there as shown in figure 49.

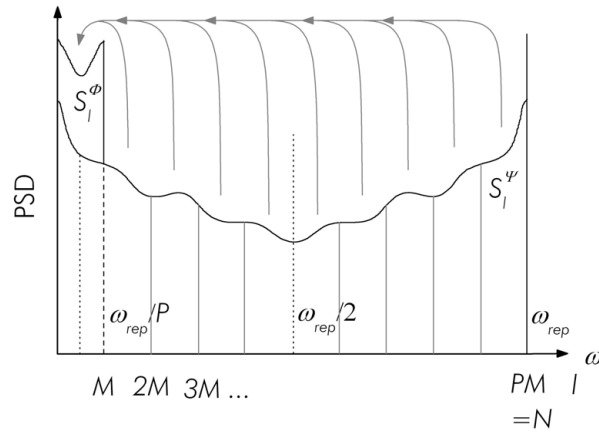


Figure 49. Different portions of the original PSD are aliased into the PSD of the picked pulse train and add there incoherently. Index l corresponds to the frequencies as given in the graph.

The integral of the PSD yields the mean square value of the phase error of the picked pulse train

$$\langle \Phi_n^2 \rangle = \frac{\Delta\omega}{2\pi} \sum_{l=0}^{M-1} \langle S_l^\Phi \rangle = \frac{\Delta\omega}{2\pi} \sum_{k=0}^{N-1} \langle S_k^\Psi \rangle = \langle \psi_n^2 \rangle, \quad \text{Eq. 21}$$

3. Few-cycle chirped-pulse amplifier systems

where $\omega = 2\pi/NT_r$ is the frequency resolution. Thus, the rms value of the picked sequence fluctuations is the same as the rms value of the original pulse train up to the full bandwidth of $\omega_{rep}/2$.

As an aside, this analysis is also applicable to similar problems such as pump pulse synchronization in non-collinear optical parametric chirped-pulse amplification systems [121, 133].

To demonstrate the above experimentally, the PSD of CE phase fluctuations was measured directly with the setup described in chapter 2.3.3 and shown in figures 30 and 32. It consisted of two independent CE phase detectors based on monolithic PPLN crystals. The first (in-loop) was used to lock the offset frequency to a 10 MHz reference signal derived from a low-noise quartz oscillator (OCXO8607, Oscilloquartz SA). With the second CE phase detector (out-of-loop) we measured the CE phase fluctuations Φ_n when locked. For this purpose we employed a 100 MHz digital sampler that was synchronized to a subharmonic at 5 kHz of the 10 MHz reference. In this way only pulses with the same average CE phase were picked (sampled). The bandwidth of the sampler was adjusted to be identical with the Nyquist frequency $\omega_{rep}/2$ so that there was always exactly one pulse from the laser present during each gate time of the sampler. For this reason it was not necessary to stabilize the repetition rate of the laser. At the same time this ensured that the full bandwidth of CE phase noise was present in the data.

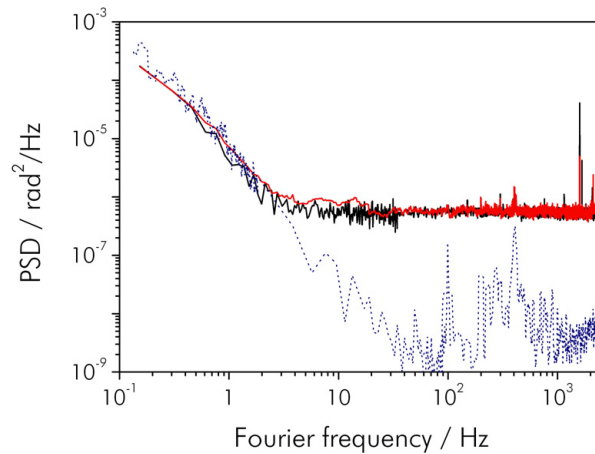


Figure 50. Two-sided PSD of phase fluctuation determined using the sampler at 5 kHz sampling frequency and 35 MHz bandwidth (black line), using equation 20 and the full phase noise PSD (red line), and full PSD neglecting all components higher than 2.5 kHz (dotted blue line).

Since the CE phase detector delivers the sine of the CE phase (up to an unknown phase offset) it can be adjusted to be maximally sensitive to phase variations and minimally sensitive to amplitude variations by choosing an appropriate reference phase in the phase-locked loop. The amplitude of the unlocked beat signal provides the voltage to phase conversion factor.

From the data obtained in this way, the left-hand side of equation 20 was calculated. We measured the full PSD of the beat signal in the same way as described in chapter 2.3.3 and calculated the right-hand side of equation 20.

A comparison between these two data sets (fig. 50) shows very good agreement in both magnitude and structure. The small discrepancy in the range from 0.5 to 20 Hz can be explained by different environmental conditions (air currents, etc.) that changed the quality of the lock during recording of various data sets. For reference, also the full PSD without taking aliasing into account is plotted.

From the above, it follows that it is necessary to characterize the phase noise properties of a femtosecond oscillator up to the full bandwidth of $\omega_{rep}/2$ to be able to derive the potential CE phase stability of a low repetition-rate amplification system seeded by this oscillator. The high-frequency components play an important role as indicated in chapter 2.3.3 and ref. [98].

Comparing the measured phase noise from the oscillator (99 mrad; see chapt. 2.3.4) with the out-of-loop phase noise measurement after the amplifier (678 mrad; see fig. 48b), it can be inferred from the above that the amplifier and compressor stage add around 578 mrad of phase noise (assuming equal amount of noise added by the detection systems).

Also the amplifier and compressor stages are contributing to CE phase fluctuations. In the amplifier stage, pump energy fluctuations contribute by means of intensity-dependent nonlinear phase effects [134]. These can be minimized by keeping the *B-integral*

$$B(t) = \frac{2\pi}{\lambda} n_2 \int I(t, z) dz, \quad \text{Eq. 22}$$

i.e. the accumulated nonlinear phase, or SPM in the amplifier low (here $B \sim 1.1$). Here n_2 is the nonlinear index of refraction and $I(t, z)$ the light intensity at coordinate z and instance t . Further, the choice of pump laser plays a role: flashlamp-pumped sources were found to introduce less than 0.1 rad rms of phase error [134]. However, the amplitude noise of diode-pumped pump lasers is by a factor of 2 to 3 better (<1% rms), therefore this contribution is negligible.

Furthermore, given the total propagation length of more than 20 m, beam pointing instabilities in the amplifier and prism compressor lead to significant path length fluctuations when the pulses propagate through optical elements (e.g. prisms) with angular dispersion. Already a tiny change in propagation length within dispersive

materials translates into considerable CE phase jitter. A change of optical beam path in fused silica ($n \sim 1.45$) of $\sim 53 \mu\text{m}$ wraps the CE phase by 2π [22]. The beam pointing instabilities in the double-pass prism compressor are estimated at $0.25 \mu\text{rad}$. With the ray-tracing algorithm developed in [98], this results in a change of the CE phase of ~ 0.2 rad. Ensuring mechanical stability and proper environmental shielding are possible remedies to this issue.

Finally, the hollow fiber-chirped mirror compressor might contribute phase noise. Previous experiments [11, 135] showed that the additional CE phase jitter introduced by the hollow-core waveguide is less than 50 mrad rms owing to the small intensity fluctuations of the amplified pulses ($<1\%$ rms pulse-to-pulse). The added phase noise stems from non-uniformity of the gas pressure and fluctuations of the spatial mode of the beam inside the hollow-core fiber. As a consequence, monitoring the CE phase at the output of the amplifier gives a true indication of the CE phase of the pulses eventually used for experiments.

3.2 Conclusions

The generation of amplified few-cycle laser pulses with controlled electric field waveform in 2003 [11] has been an amazing feat, as it opened the door for a series of astonishing experiments in the field of time-resolved spectroscopy and metrology [5, 6, 136]. In order to reach CE phase-stability of the output pulses, every building block in the amplifier system and its phase noise contribution has to be carefully controlled. The CE phase-stabilization by a monolithic PPLN crystal is highly suitable for the seed oscillator as it is a compact scheme that requires no beam-splitting. Due to the absence of microstructure fibers, the handling is less cumbersome and lower phase noise can be achieved. Starting off with few-cycle pulses phase-stabilized to within less than 100 as , a secondary broadband phase detector is necessary to compensate for the slow phase drifts introduced by the amplifier and prism compressor. The hollow fiber used for subsequent spectral broadening adds more phase noise. In a further step, this phase noise can be detected by CE phase-dependent nonlinear processes. For instance, the spatial distribution of electrons generated by above-threshold ionization is depending on the CE phase as discussed in chapter 5.3 and can be exploited in a compact device to give feedback to the phase-locking electronics [23].

Chapter 4

Femtosecond enhancement cavities

Increasing the pulse energy of few-cycle pulses without compromising the repetition rate has long been a major challenge. First and foremost, a repetition rate higher than ~ 1 MHz is mandatory for high-resolution spectroscopy, as discussed in chapter 1. Yet standard chirped pulse amplifiers as presented in chapter 3 reduce the repetition rate to a few kilohertz. The most notable advance in the direction of amplification at the full repetition rate, the recent development of chirped-pulse oscillators is limited by detrimental nonlinearities and ultimately by the availability of adequate pump sources. The same applies to post-amplification with a continuous wave pump source (cf. chapt 2.4).

An alternative way to boost the pulse energy and average output power is the use of a resonant cavity. The concept of power enhancement in a cavity is well-known in the area of cw lasers. For increasing the efficiency of nonlinear conversion, the corresponding medium is placed in a resonator arrangement. If the resonance conditions are met and the light interferes constructively, conversion efficiencies approaching unity can be reached [137]. Not only does the higher power of the circulating light drive the nonlinear medium more strongly, resulting in higher single-pass efficiency, but also light that is not converted in a single pass remains stored in the resonator and can contribute in later passes.

For a mode-locked laser source, this scheme can be applied as well and has been employed to enhance frequency conversion (second or third harmonic generation) by nonlinear crystals in a variety of systems: 100 fs pulses from a Cr:forsterite laser [138], 1.5 ps pulses from a Ti:sapphire laser [139], picosecond pulses from a dye laser [140], 83 fs pulses from a Ti:sapphire laser [141], and 33 ps pulses from a Nd:YVO₄ laser [142]. Recently, the step has been made to the intra-cavity frequency conversion by high-harmonic generation with 48 fs pulses [37] and 20 fs pulses [7] from a Ti:sapphire laser (see chapt. 5.2.2 for details). However in the case of pulsed operation the issue becomes much more complex, as not only one mode has to be made resonant in the cavity as in the cw case, but a comb of frequencies, as given by eq. 6. This raises the requirements for the cavity, as resonance is achieved only if the following conditions are met: (1) the envelope of the stored pulse does not change its shape in a roundtrip in the cavity, (2) the roundtrip time in the cavity equals the repetition period of the seeding laser, and (3) the waveform of the electric field underneath the pulse envelope of the seeding and circulating pulses stays in phase. In other words, (1) requires that the net dispersion inside the cavity is zero. If this is fulfilled, (2) and (3) require that the repetition rate and the offset frequency of the cavity match those of the seeding laser.

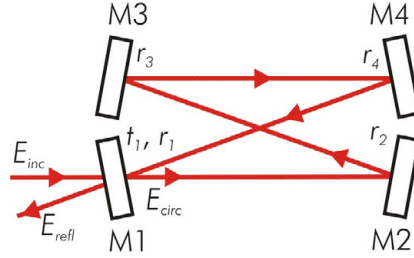


Figure 51. Sketch of an optical resonator. The coefficients r_i denote the mirror reflectivities, t_1 the input coupler (M1) transmission and E_{inc} , E_{circ} , and E_{refl} the electric fields of the incident, circulating and reflected waves, respectively.

In the following chapter, the design and setup of an enhancement resonator operating at 10 MHz repetition rate is described (chapt. 4.1 and 4.2). The intra-cavity nonlinear frequency conversion by high-harmonic generation is presented with a similar system operating at 100 MHz (chapt. 5.2.2).

4.1 Passive optical resonators for femtosecond pulses

Supporting the large bandwidth of femtosecond pulses in an optical resonator is far more complicated, theoretically as well as experimentally, than the case of cw radiation. However, several properties of enhancement resonators can be transferred from this simpler case (as in e.g. ref. [101]). Hence, considering for the moment only monochromatic waves of frequency ω and neglecting the transverse spatial mode distribution, the electric field of the beam seeding a resonator can be written as

$$E_{inc}(t) = \frac{1}{2} \left(E_{inc} e^{i\omega t} + c.c. \right), \quad \text{Eq. 23}$$

where E_{inc} is the field amplitude. Similarly, the electric field circulating inside the resonator $E_{circ}(t)$, taken at the position right after one round-trip and the field that is reflected $E_{refl}(t)$ from the input coupler M1 can be described (see fig. 51). In general, all field amplitudes are vectors, however with a linearly polarized beam scalars can be used. The circulating field results from the superposition of the incident field $E_{inc}(t)$ transmitted through the input coupler M1 and the field that was already present in the resonator one round-trip before. Therefore the steady state of the field inside the resonator at position M1 is given by

$$E_{circ} = t_1(\omega) E_{inc} + G(\omega) E_{circ}, \quad \text{Eq. 24}$$

with $t_1(\omega)$ being the input coupler transmission, and $G(\omega)$ the net round-trip gain of the system. Assuming a medium with a refractive index of one inside the resonator it is given by

$$G(\omega) = \exp(i\omega L / c) r_1(\omega) r(\omega) \exp(i\varphi(\omega)), \quad \text{Eq. 25}$$

with $r(\omega) e^{i\varphi(\omega)} = r_2(\omega) r_3(\omega) r_4(\omega) r_{diff}(\omega)$ the product of complex mirror reflectivities (except for the input coupler reflectivity $r_1(\omega)$) and diffraction losses $r_{diff}(\omega)$, L the optical path length of the resonator, and $\varphi(\omega)$ all additional phase shifts during one round-trip. The circulating field is solved as

$$E_{circ} = (1 - G(\omega))^{-1} t_1(\omega) E_{inc} \quad \text{Eq. 26}$$

and the power enhancement, i.e. the power of the circulating field related to the incident power is given by (using eqs. 25 and 26)

$$P(\omega) = \frac{|E_{circ}|^2}{|E_{inc}|^2} = \frac{|t_1(\omega)|^2}{1 + r^2(\omega) r_1^2(\omega) - 2r_1(\omega) r(\omega) \cos\left(\frac{\omega}{c} L + \varphi(\omega)\right)}. \quad \text{Eq. 27}$$

Assuming constant r , r_1 , t_1 , and φ expression 27 is maximized for $\omega = n2\pi c/L - \varphi c/L$. The spacing between the resonances is called *free spectral range* and given by

$$\omega_{FSR} = 2\pi c / L. \quad \text{Eq. 28}$$

The width (FWHM) of these resonances is (for $1 - r \ll 1$)

$$\Delta\omega_{FWHM} = \frac{1 - r_1 r}{\pi \sqrt{r_1 r}} \omega_{FSR} =: \omega_{FSR} / F. \quad \text{Eq. 29}$$

This width relaxes the requirement of constancy for r , r_1 , t_1 , and φ to slowly varying, as constancy is only necessary on the scale of ω . The *finesse* of a cavity is defined as $F = \omega_{FSR} / \Delta\omega$.

On resonance, the enhancement factor is

$$P = \frac{|t_1|^2}{\left(1 - \sqrt{1 - |t_1|^2} r\right)^2} \quad \text{Eq. 30}$$

neglecting losses in the input coupler ($r_I^2 = 1 - t_I^2$).

For $T_{max} := |t_I|^2 = 1 - r^2$, the so-called *impedance-matched coupling*, the enhancement factor is maximized and becomes

$$P_{max} = \frac{1 - r^2}{(1 - r^2)^2} = 1/T_{max} \approx F/\pi. \quad \text{Eq. 31}$$

Therefore, choosing an input coupler with transmission T_{max} optimizes the power enhancement in the cavity.

The enhancement factor as a function of the frequency of the driving field is shown in figure 52.

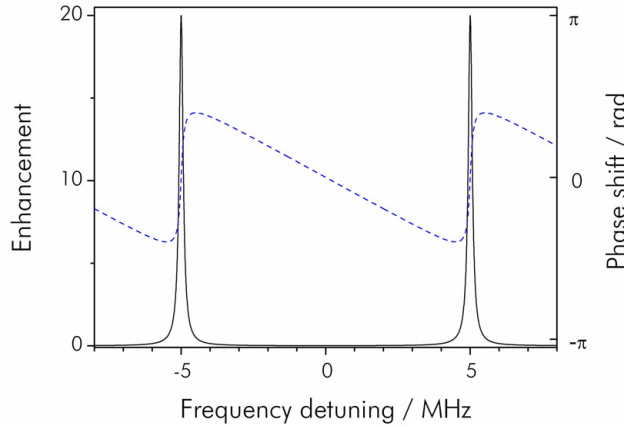


Figure 52. Enhancement factor (black solid) and phase shift (blue dashed) with regard to the incident laser field as a function of laser frequency. The parameters used are as follows: The cavity length is 30 m, corresponding to a free spectral range of $2\pi \cdot 10$ MHz. Effective mirror reflectivity is $r^2 = 95\%$, thus impedance-matching requires an input coupler transmission of $T_{max} = 5\%$. The resulting power enhancement on-resonance is $P_{max} = 20$ and the finesse $F = 61$.

So far only a monochromatic wave was considered. The situation becomes more complex when the broadband output of a femtosecond laser is to be made resonant in the cavity. Here, the comb-like structure of the spectrum (see chapt. 2.3.1) from a mode-locked laser helps: if each comb line is precisely located at a resonance, it will be enhanced just like the harmonic wave treated in the preceding paragraph and therefore the entire spectrum gets enhanced. Thus the task is to line up the comb modes of the seeding laser with the resonance frequencies of the cavity. The former are given by the indexing equation $\omega_n = n\omega_{rep} + \omega_{CEO}$, with ω_{rep} and ω_{CEO} being the repetition and offset (angular) frequencies of the laser, respectively. The latter originate from the resonance condition of equation 27

$$\omega'_n = n \frac{2\pi c}{L} - \frac{c \varphi(\omega'_n)}{L}. \quad \text{Eq. 32}$$

Despite their similarity, the ‘offset frequency’ $c \varphi(\omega'_n)/L$ is still depending on n . In order to transform the above relation into a frequency comb relation with a regular mode spacing, $\varphi(\omega)$ has to conform (in the spectral region of interest) to

$$\varphi(\omega) = -\varphi'_{CEO} + \tau' \omega. \quad \text{Eq. 33}$$

With this ansatz, equation 32 becomes

$$\omega'_n = \frac{n2\pi + \varphi'_{CEO}}{L/c + \tau'} =: n \omega'_{rep} + \omega'_{CEO} \quad \text{Eq. 34}$$

with the effective repetition rate $\omega'_{rep} = 2\pi/(L/c + \tau')$ and the effective offset frequency $\omega'_{CEO} = \varphi'_{CEO}/(L/c + \tau')$ of the resonator.

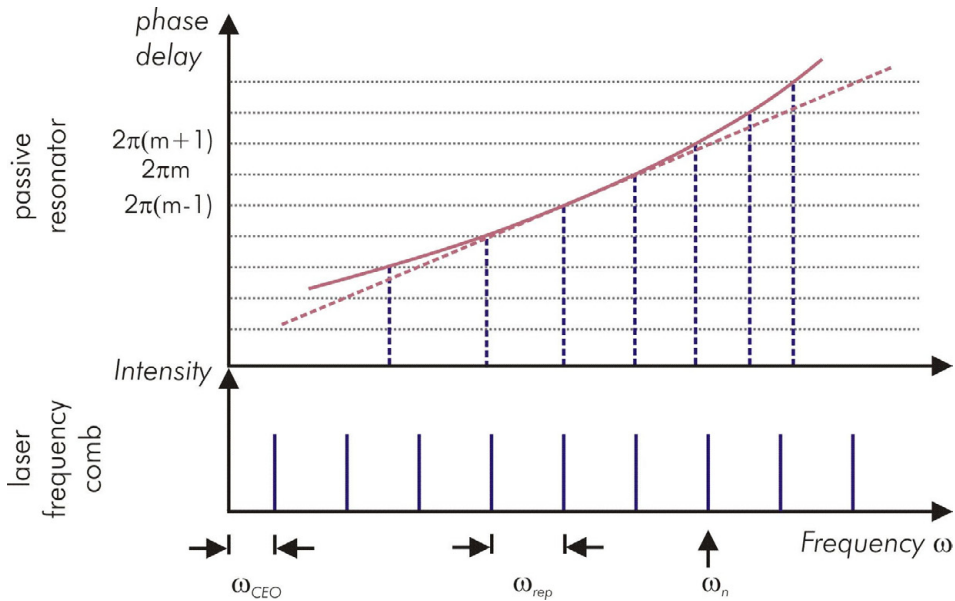


Figure 53. Schematics of the frequency comb of the seeding laser (bottom) and cavity resonances (top). The evolution of the phase delay $\omega L/c + \varphi(\omega)$ as a function of wavelength is not linear in the presence of dispersion in the cavity (optical elements, air, etc.). As a consequence, the resonances are not equidistant anymore. This brings about that only the comb modes that overlap are enhanced (in the middle of the figure) and the overall power enhancement is decreased.

From this it becomes apparent that τ' is the additional round-trip delay and ϕ'_{CEO} the round-trip carrier-envelope phase shift (see chapt. 2.3.1) of the resonator.

In reality, the phase contribution $\phi(\omega)$ will differ from the linear ansatz in equation 33, due to the dispersion introduced by the optical elements and the air in the resonator. Figure 53 shows the effect of dispersion on the line-up of the laser comb with the resonances.

The alignment of the comb modes of laser and resonator is achieved by making ω'_{rep} , coincide with ω_{rep} and ω'_{CEO} coincide with ω_{CEO} or vice versa. This is merely a re-phrasing of the aforementioned requirements (2) and (3). However, satisfying these criteria for enhancement only makes sense if requirement (1) is fulfilled, the constancy of the pulse envelope during one cavity round-trip, i.e. the absence of dispersion.

4.1.1 Dispersion control

Optical elements inside the cavity such as mirrors or even air will have a non-vanishing dispersion. Here, only the second-order dispersion D is considered and higher-order terms neglected.

Dispersion increases the chirp of the pulses and thus their width according to [143]

$$\tau'_p = 2\sqrt{\tau_p^2 + D^2 / \tau_p^2} \quad \text{Eq. 35}$$

with τ_p the undistorted and τ'_p the distorted pulse duration. As a consequence, the overlap of the circulating pulse with the incident pulse is worsened in the time domain. Regarded in the frequency domain, dispersion reduces the enhancement factor essentially by the decrease of the spectral power at the spectrum edges. This causes a deterioration of the spectral overlap between pulses from the resonator and the seed laser proportional to $(1+\omega^4 D^2)^{-1}$ [144]. The power enhancement of the incident comb modes is reduced to half the maximum at

$$\Delta\omega_{inc} = \sqrt{2\pi / DF}, \quad \text{Eq. 36}$$

where D is the dispersion of second order (GDD) [145]. This implies that the maximum bandwidth (FWHM) from the seeding laser that can be enhanced is $2 \omega_{inc}$. For a cavity of 30 m round-trip length, the GDD of air alone (notwithstanding other optical elements) amounts to $D = \sim 435 \text{ fs}^2$ at 800 nm wavelength. With a finesse of $F = 100\pi$, this results in a bandwidth of $2 \omega_{inc} = 13.5 \text{ THz}$ or $\sim 5 \text{ nm}$. This 'acceptance bandwidth' becomes smaller with increasing dispersion.

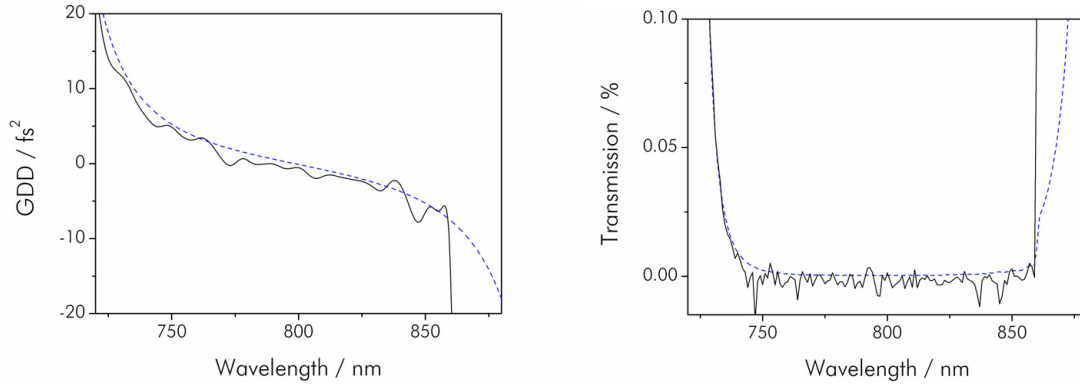


Figure 54. (a) Group delay dispersion of the high-reflecting cavity mirrors. Black line shows data measured with the cavity-based technique (angle of incidence 3.5° ; averaged over 7 nm), blue dashed line shows calculated data as provided by the manufacturer (Layertec GmbH). In the spectral region of interest (740 – 825 nm) the GDD varies between 6 and -2 fs^2 . (b) Mirror reflectance. Black line shows data measured with a spectrophotometer (Lambda 900, Perkin-Elmer Inc.). Blue dashed line shows calculated data as provided by the manufacturer (ATFilms Inc.). The transmission is specified at 5 ppm in the spectral region of interest.

Thus, a net dispersion of the cavity as close to zero as possible in the spectral bandwidth of the seeding laser is desirable for maximum power enhancement. For the enhancement cavities presented here, two measures for dispersion control were taken. Firstly, the cavity was set up in vacuum to prevent the dispersive influence of air. Secondly, care was taken to select mirrors with as small dispersion as possible while having extremely low loss at the same time. In order to find the mirrors with the best dispersion characteristics, surface quality and damage threshold, three batches were coated at different companies, respectively in-house. Figure 54 shows the dispersion and reflectance properties of some of the mirrors employed. For the targeted intra-cavity nonlinear frequency conversion (as described in chapt. 5.2.2), a thin sapphire plate has to be inserted at Brewster angle in the resonator. This introduces additional positive dispersion, which has to be compensated for together with the remaining GDD of the high reflecting mirrors. Therefore one chirped mirror (see chapt. 2.2) with carefully designed negative dispersion is added to the cavity. Due to the absence of air, only one chirped mirror is sufficient. This has the advantage that for the other mirrors the design is more flexible and can be optimized for high reflectivity. The target dispersion curve for the design is simply the negative sum of the GDD contributions of the other optical elements. The GDD properties of sapphire can be calculated with the Sellmeier equation using the coefficients found, e.g. in [146]. However, the actual quantity of interest is the uncompensated effective round-trip phase $\psi(\omega)$ (as shown in fig. 53) which has to be sufficiently close to integer multiples of 2π , scaled by the finesse

$$\psi(\omega) - n2\pi \ll \pi / F . \quad \text{Eq. 37}$$

The round-trip phase is generally connected to dispersion by the coefficients of its Taylor expansion

$$\begin{aligned} \psi(\omega)|_{\omega_0} &= \psi(\omega_0) + \psi'(\omega_0)(\omega - \omega_0) + \frac{1}{2}\psi''(\omega_0)(\omega - \omega_0)^2 + O(\omega - \omega_0)^3 \cong \\ &\cong \psi_0 + \psi_1(\omega - \omega_0) + \frac{1}{2}\psi_2(\omega - \omega_0)^2 \end{aligned} \quad \text{Eq. 38}$$

where $\psi_0 = \psi(\omega_0)$ is a global phase shift, the phase delay, $\psi_1 = d\psi/d\omega(\omega_0)$ the group delay and $\psi_2 = D = d^2\psi/d\omega^2(\omega_0)$ the group delay dispersion.

Figure 55 shows the target design curve, uncompensated group delay and phase of a set of mirrors, including the sapphire plate.

Precise characterization of the dispersion and reflectance properties of dielectric mirrors is a tedious task when approaching a transmission of 5 ppm or GDD fluctuations below 5 fs². Recent new developments have increased the accuracy so that measurements at these levels have become possible.

Measuring reflectances so close to unity is impossible directly. Therefore, usually cavity ring-down spectroscopy is employed for this purpose [147, 148]. The ring-down time of a cavity basically is the decay rate of the field inside, i.e. the photon lifetime, when the driving light is switched off abruptly. Making a switch that is fast enough is challenging, therefore the cavity is swept across a resonance and from the circulating power, the resonator decay constant can be determined. Measuring the cavity losses with and without the optical element under scrutiny, its losses can be inferred (if they are sufficiently large compared to the other cavity losses). Alternatively, if the elements that make up the resonator are of interest, the ring-down time yields the overall losses of the cavity.

Precise GDD measurements have also benefited from the development of high-finesse cavities. The general idea is to detect the Moiré pattern between the equidistant laser frequency comb and the cavity resonances when shifting the overall position of the comb by means of the offset frequency f_{CEO} [75, 76]. From the difference in the recorded spectra, the dispersion contribution of additionally introduced optical elements can be calculated. This method can reach an accuracy of 2 fs² in a resolution bandwidth of 0.6 nm [75].

With these recently developed characterization techniques dramatic improvements to the dielectric mirror design and manufacturing can be expected, as the effect of design modifications can be examined with high precision.

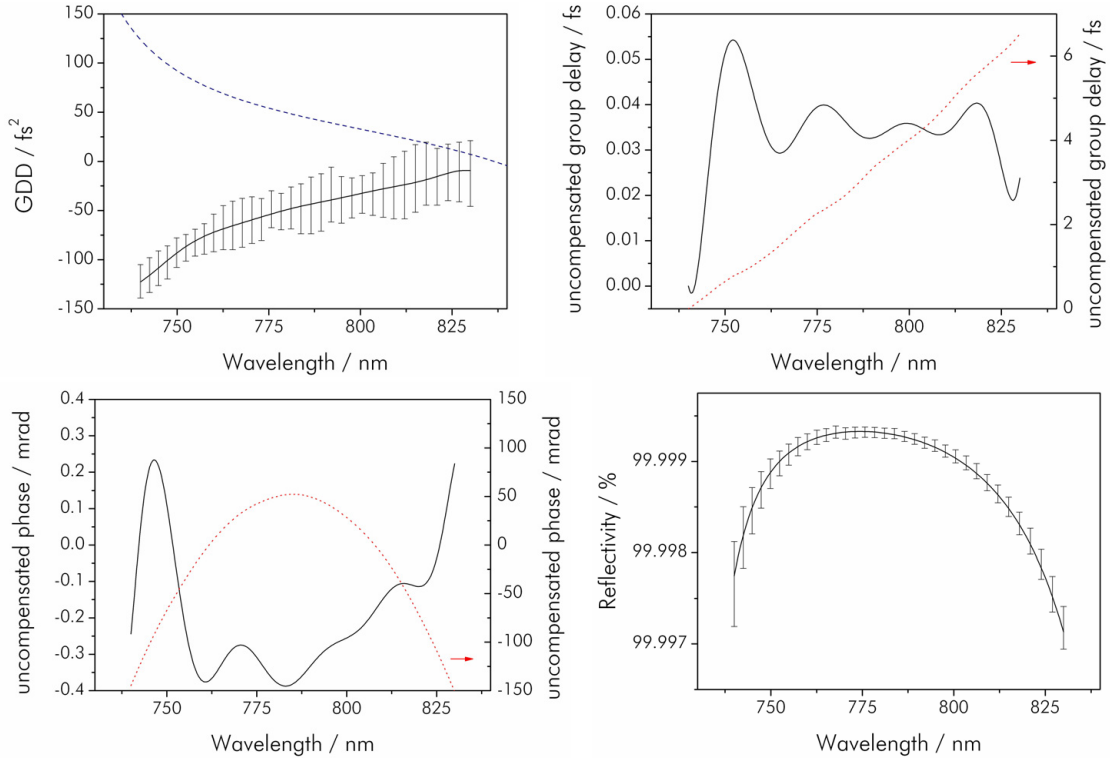


Figure 55. Compensation of the cavity dispersion by a chirped mirror. **(a)** shows the net theoretical GDD of the cavity to be compensated (blue dashed line, averaged over 7 nm). This includes eight high-reflectors, an input coupler with 0.25% nominal transmission (both Layertec GmbH), and a 0.5 mm thick sapphire plate at Brewster angle (Korth Kristalle GmbH). No air dispersion is taken into account as the resonator is located in vacuum. The black line shows the design curve of the chirped mirror that compensates for the positive GDD in the cavity. The error bars represent the span of 67% of the values in a Monte-Carlo simulation of 1000 runs assuming realistic production tolerances. **(b)** shows the corresponding uncompensated group delay, and **(c)** the uncompensated phase delay. The dashed lines illustrate the group (phase) delay when using the maximum value of the errors of the chirped mirror design, as displayed in **(a)**. **(d)** shows the calculated reflectivity of the chirped mirror.

4.1.2 Electronic feedback techniques

Having assured by dispersion control that the circulating pulse does not change its shape during one round-trip, the repetition period and CEO phase shift of laser and resonator can be aligned (requirement (2) and (3) on p. 67). In the frequency domain this equals the matching of (effective) repetition and offset frequencies.

This alignment is accomplished by tuning the cavity length of the laser or enhancement resonator (ω_{rep}) and the intra-cavity dispersion of the laser (ω_{CEO}). While the dispersion characteristics of the resonator can be assumed to be only drifting slowly,

just like all material parameters, both parameters are fluctuating on a shorter time scale. This is mainly due to mechanical vibrations or thermal drifts of the mirror positions. Because of the high mode numbers ($n \approx \omega/\omega_{rep} \approx 10^6$) and finesse of the resonator, fractional length changes on the order of a few nanometers already lead to a substantial change of the circulating power. Therefore, active feedback is implemented on the cavity length, forcing the cavity and the laser on resonance at a certain frequency. On the other hand, the offset frequency fluctuates on a slower time scale and is not leveraged by the mode number and is thus of lower importance for high enhancement. Manual offset frequency adjustment, e.g. by wedges inside the laser is sufficient for good results, however for optimum enhancement both degrees of freedom need to be actively stabilized.

Electronic phase-locking loops are employed for the stabilization, along the same lines as in chapter 2.3.3. For the generation of an error signal, principally two options are established: *polarization locking* [149] and *Pound-Drever-Hall locking* [150]. Both use the phase shift (see fig. 52) of the circulating field inside the resonator with respect to the incident field to construct the error signal.

The former requires a polarization-discriminating element inside the resonator in the sense that only a particular (linear) polarization can fulfill the resonance conditions, while the polarization perpendicular to that is suppressed by high losses. The discrimination of polarization is provided in the presented system by the sapphire plate that is installed at Brewster angle inside the cavity. Only p-polarized light (with respect to the sapphire plate plane of incidence) satisfies the Brewster condition, s-polarized light experiences high losses and is poorly impedance-matched at the input coupler. Rotating the polarization of the incident light slightly versus the plane of incidence creates a small amount of s-polarized light that is not coupled into the cavity but reflected. Also, the p-polarized light that is not coupled into the cavity is reflected but with a phase shift. Both polarization components add to give a circular polarization component depending on the phase shift.

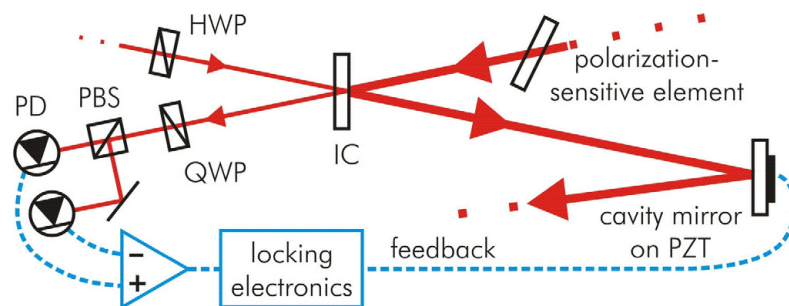


Figure 56. Setup for polarization locking. The polarization-sensitive element consists of the thin Brewster-angled sapphire plate. The feedback may be given to a piezo-actuated mirror in the enhancement resonator (as shown) or in the laser cavity. HWP (QWP): half (quarter) wave plate; IC: input coupler; PBS: polarizing beam splitter; PD: balanced photodetector; PZT: piezoelectric transducer.

On resonance, at phase shift zero, the reflected beam is again linearly polarized. A circular polarization analyzer, consisting of a quarter wave plate, a polarizing beamsplitter, and a difference photo detector (balanced receiver) as shown in fig. 56 is used to extract the phase information and create an electronic signal accordingly. If the beam is linearly polarized at the quarter wave plate, the two signals from the balanced photodiodes cancel each other. A loop filter and amplifier shape the error signal electronically before it is fed to a piezoelectric transducer that controls the cavity length and in this way closes the stabilization loop.

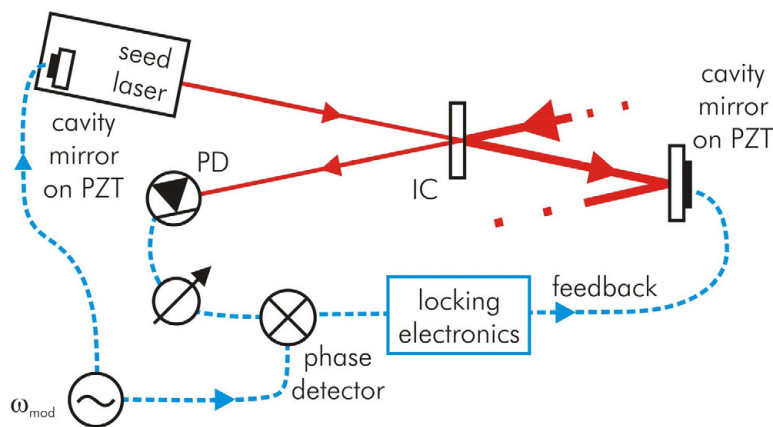


Figure 57. Setup for Pound-Drever-Hall locking. The output of the seed laser is phase modulated by a cavity mirror oscillating at ω_{mod} with the modulation frequency being provided by a frequency synthesizer. The feedback may be given to a piezo-actuated mirror in the enhancement resonator (as shown) or in the laser cavity. IC: input coupler, PD: photodetector, PZT: piezoelectric transducer.

The alternative way for producing an error signal is the so-called Pound-Drever-Hall technique (see fig. 57). There, the incident beam from the seed laser of central frequency ω_0 is phase-modulated with frequency ω_{mod} such that sidebands at $\omega_0 \pm \omega_{\text{mod}}$ are created. The modulation takes place by oscillating a cavity mirror on a piezoelectric transducer with a modulation frequency ω_{mod} drawn from a frequency synthesizer. In order to avoid coupling of the sidebands into the enhancement cavity, ω_{mod} is chosen to be much larger than the bandwidth of the cavity resonances ω (see eq. 29). A photodiode detects the beam reflected at the input coupler that contains a beating signal between the carrier frequency (at frequency ω_0) and the sidebands (at frequency $\omega_0 \pm \omega_{\text{mod}}$). The phase of the beating signal depends on the relative detuning between laser and resonator. A mixer compares the phase of the beating signal with the one of the reference and generates a dispersive error signal (shown in fig. 58).

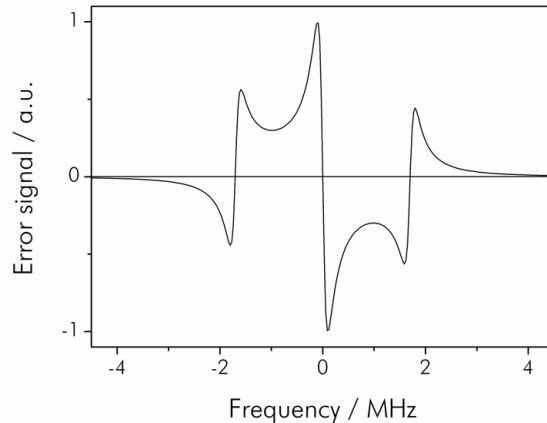


Figure 58. The calculated Pound-Drever-Hall error signal. The error signal crosses zero if the carrier or any of the sidebands resonates in the cavity. However, the sign of the error signal's slope is opposite for the carrier and the sidebands. The modulation frequency is $\omega_{\text{mod}} = 1.7$ MHz, about 3% of the free spectral range (cavity length 30 m). The cavity finesse is 100π .

The main advantage of the Pound-Drever-Hall scheme is its independence from a polarization-sensitive cavity element. Also, in contrary to the polarization locking scheme it does not require the balancing of a difference photo detector which can be tricky as beam pointing instabilities affect both photodiodes differently. The dynamic locking range is in principle only limited by the modulation frequency. The disadvantage of the scheme is the necessity for modulating the seed laser beam. On the other hand, the main advantage of the polarization locking technique is the simple setup, no phase-modulation of some sort is necessary.

Ultimately, it is necessary not only to phase-lock the offset frequencies of the laser and enhancement cavity to each other, but also to know the value of f_{CEO} . This can be accomplished by an f -to- $2f$ nonlinear interferometer (see chapt. 2.3.1) using a beam branched-off before the enhancement cavity. With the Pound-Drever-Hall scheme, the sidebands generated to each comb line create additional mixing products in the microstructure fiber of the nonlinear interferometer. The resulting large number of lines in frequency space considerably decreases the effective signal-to-noise ratio of the f_{CEO} beating signal. Thus the phase-modulation impedes the usage of the frequency comb for offset frequency detection by the self-referencing scheme. Furthermore, the phase-modulation of the seed beam introduces phase noise to the intra-cavity comb despite the fact that the sidebands are not coupling to the cavity. This affects the intra-cavity nonlinear frequency conversion negatively. These reasons disqualify the Pound-Drever-Hall locking scheme from usage in this particular arrangement.

Both presented locking schemes only control one degree of freedom of the frequency comb, the other one is still fluctuating. For best enhancement, it is desirable to stabilize

both degrees. This can be achieved by spectrally dispersing the beam reflected from the input coupler by means of a grating and taking two different spectral components to create two error signals in two separate detection setups (of either kind). Both error signals are then orthogonalized, before being sent to the locking electronics and their respective feedback actuators. The feedback actuators need to be linearly independent in order to prevent oscillations between the two loops. Ideally, the fixed point (see chapt. 2.3 and ref. [79, 80]) of one of the actuators should be at zero frequency (theoretically, frequency $\rightarrow \pm\infty$), while the other fixed point should be close to the carrier frequency.

The best positioning in the dispersed spectrum for the two detection systems is such that the fixed point close to the carrier is in the middle between the locking points. Generating sum and difference of the two signals provides a measure of any arbitrary fluctuation of the combs, split in the linear combination with regard to the actuators. For example, the difference yields the signal for the actuator whose fixed point is at the carrier frequency.

The cavity length controlled through a piezo-actuated mirror usually constitutes a feedback degree of freedom. Altering the cavity length changes f_{rep} and has virtually no impact on f_{CEO} . As the fixed point of the frequency comb for cavity length changes is at zero frequency, the effect is multiplied by the mode number $n \approx 10^6$ and thus mainly changes the overall position of the comb.

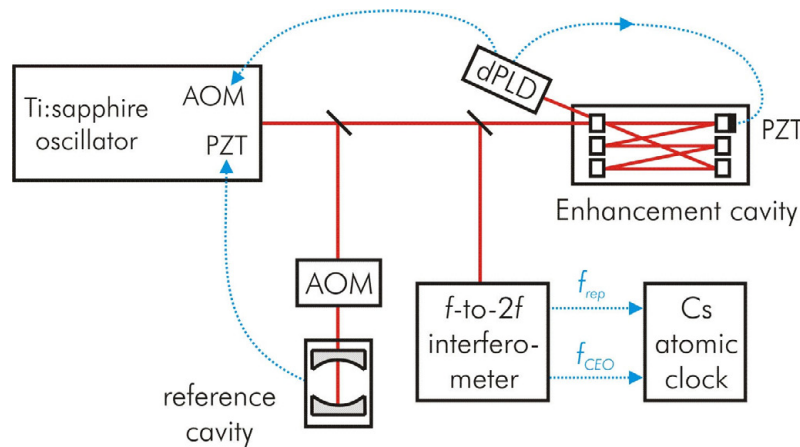


Figure 59. Setup for referencing the cavity comb to an atomic clock. A reference cavity is employed to stabilize the frequency comb and reduce the mode linewidth. An acousto-optic modulator (AOM) shifts the frequency comb with respect to the reference cavity. An f -to- $2f$ interferometer is used monitor the two comb parameters and compare them to a cesium atomic clock. The enhancement cavity is phase-locked by a double polarization locking detection (dPLD) with feedback to the enhancement cavity length (PZT) and the laser pump power (AOM).

As a consequence, when the cavity length fluctuates from external perturbations, both detectors will recognize a drift of their observed comb lines. Using the locking electronics to control the sum of the signals from both detectors to be zero on average will therefore stabilize f_{rep} .

Pulse energy modulation by an acousto-optic modulator in the pump laser beam (as described in chapter 2.3.3) is a possible second feedback option that is linearly independent from the former. The fixed point of the frequency comb for this mechanism is approximately at the carrier frequency [80] and thus, again via the mode number, mainly the offset frequency f_{CEO} is affected. If f_{CEO} is changed, either by the actuator or due to environmental perturbations, both detectors will observe an identical shift of the comb lines if symmetrically positioned about that fixed point. Using the locking electronics to control the difference of the signals from both detectors to be zero on average will therefore stabilize f_{CEO} .

Ultimately, for the frequency comb inside the enhancement resonator to be useful for spectroscopic experiments, the position of the comb lines needs to be known in an ‘absolute’ manner, i.e. it needs to be referenced to an external clock. As in the course of phase-locking the cavity frequency comb is stabilized to the seeding frequency comb, it is possible to reference the seed laser to the time standard. The schematic of such a setup is shown in figure 59. In a first step and before seeding the cavity, the laser beam is split and one part sent to an optical reference cavity after spectral filtering. Phase-locking one of the laser frequency comb modes to this highly-stable reference cavity reduces the linewidth of all the comb modes. A frequency shifting acousto-optic modulator is employed to shift the comb lines across the region of interest in the spectroscopy experiment. The laser comb parameters f_{rep} and f_{CEO} are monitored by an f -to- $2f$ nonlinear interferometer (chapt. 2.3.1) that uses another beam branched off from the laser. Both rf frequencies are compared to a cesium atomic clock, thus establishing the link to the time standard. The error signal generation and phase-locking between enhancement cavity and laser is achieved as described above with the feedback actuating on the enhancement resonator length on the one hand and the offset frequency of the laser on the other. In this way, the frequency comb inside the enhancement cavity is referenced to an atomic clock. With intra-cavity nonlinear frequency conversion, this opens the door to optical frequency metrology in previously unexplored spectral regions.

4.2 Vacuum enhancement cavity at 10 MHz repetition rate

In the following, the experimental setup and results from an enhancement cavity operating at 10 MHz repetition rate are presented. The cavity aims at enhanced nonlinear conversion to the XUV spectral region. This is accomplished by means of high-order harmonic generation (see chapt. 5.2) in a gas jet placed in a cavity focus. An overview of the setup is shown in figure 60.

The cavity is seeded by the 10 MHz repetition rate chirped pulse oscillator described in chapter 2.4. The laser pulses are sent to a double-prism compressor for compression down to a pulse width of approximately 35 fs.

Before coupling into the enhancement cavity matching the spatial mode of the laser to the resonator mode is necessary. In other words, the q parameter, i.e. the focus size and its position, of the incident beam at the input coupler has to equal the q parameter of the circulating beam. For this purpose a telescope consisting of a focusing ($f = 1000$ mm) and a defocusing lens ($f = -500$ mm) are employed. Their position and distance were calculated by means of the ABCD matrix formalism [151]. The next focus in the cavity after the input coupler was used as an image point for the focus of the laser mode.

In order to increase efficiency for the coupling into the cavity, the direction of the seed beam is stabilized by a beam-pointing stabilization device. It consists of two quadrant photodiodes where residual reflections of the beam are detected and two piezo-mounted mirrors that control the beam direction.

The cavity itself is completely set up in a vacuum chamber. This has the advantage of removing the dispersive effect of air and the absorption at the fundamental wavelength at 790 nm. As a consequence, only a fraction of the dispersion of a cavity in air has to be compensated by chirped mirrors. In fact, as the amount of GDD to be compensated is small (see fig. 55), a single chirped mirror is sufficient for intra-cavity dispersion compensation. This means that the other cavity mirrors can be optimized for high reflectivity. However, even these mirrors have non-negligible losses, therefore the number of reflections should stay within limits. With the cavity length being fixed to ~ 30 m, the number of acceptable bounces per round-trip was determined at 10, which resulted in a total cavity length of ~ 3.5 m and made the setup just table-top. A drawing of the vacuum chamber setup is shown in figure 61. Due to the large distance between the folding mirrors on either side and the high requirements for efficient enhancement, passive mechanical stability is an issue. For improving it, a passive stabilizer was mounted between the main breadboard and the small breadboard carrying the four folding mirrors. As its linear temperature expansion coefficient is more than an order of magnitude better than ordinary stainless steel, a tube made of Invar-36 ($\text{Fe}_{64}\text{Ni}_{36}$, $L/L = 1.18 \cdot 10^{-6}$ 1/K) was employed. Thus the total change in cavity length was estimated at $L_{\text{tot}} = 64$ μm for a temperature change of 1 K.

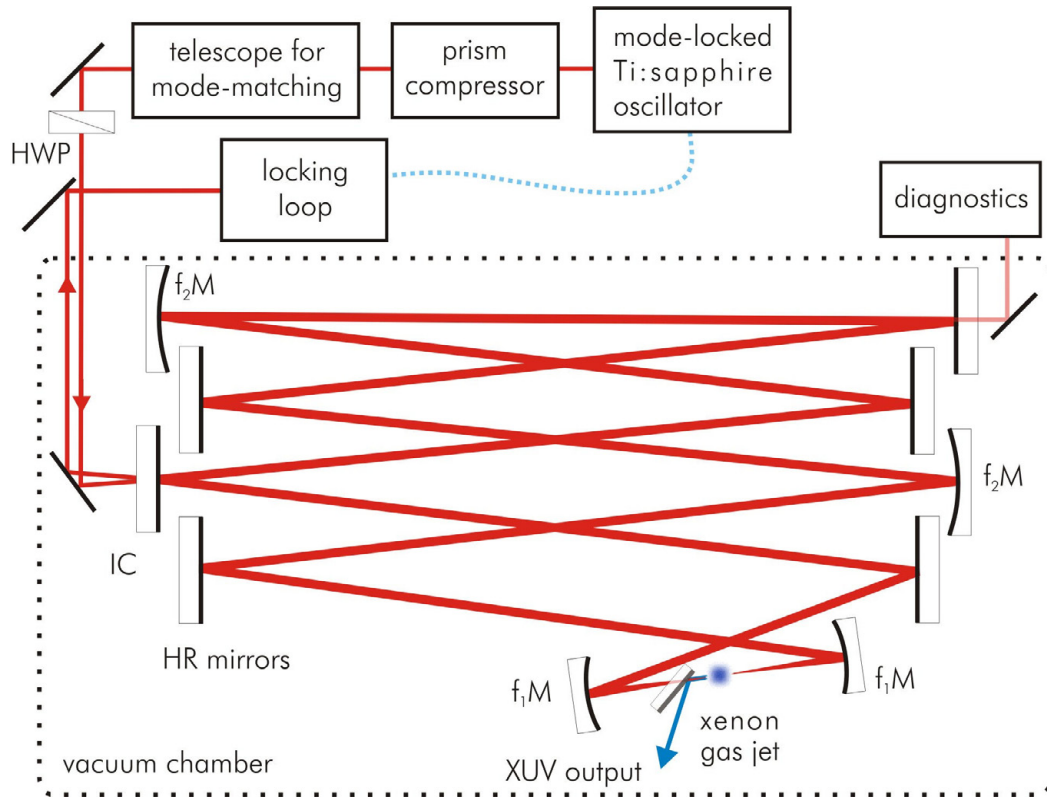


Figure 60. Enhancement cavity schematic overview. The cavity is located in a vacuum chamber. Distances are not to scale. Xenon gas jet and XUV output are for the nonlinear frequency conversion, see chapter 5.2.2 for details. HWP: half-wave plate necessary for polarization locking; IC: input coupler with 0.25% transmission; HR mirrors: high-reflecting mirrors (chapt. 4.1.1); f_1M : focusing mirrors, ROC 30 cm; f_2M : focusing mirrors, ROC = -10.24 m, for the intra-cavity telescope; diagnostics: optical spectrum analyzer (HR4000, Ocean Optics Inc.) for the intra-cavity spectrum, powermeter and photodiode for observation of the spectrally-integrated transmission.

However, it turned out that this long tube (inside the actual vacuum tube) introduces strong additional mechanical resonances in the tens to hundreds of hertz range to the system. Therefore, despite the improvement of slow drifts it was removed at a later stage.

The cavity is of a bowtie-type, i.e. it consists of a long and a short cavity section. The short, focused section contains the gas target for nonlinear conversion and a thin sapphire plate at Brewster angle for out-coupling the frequency converted light.

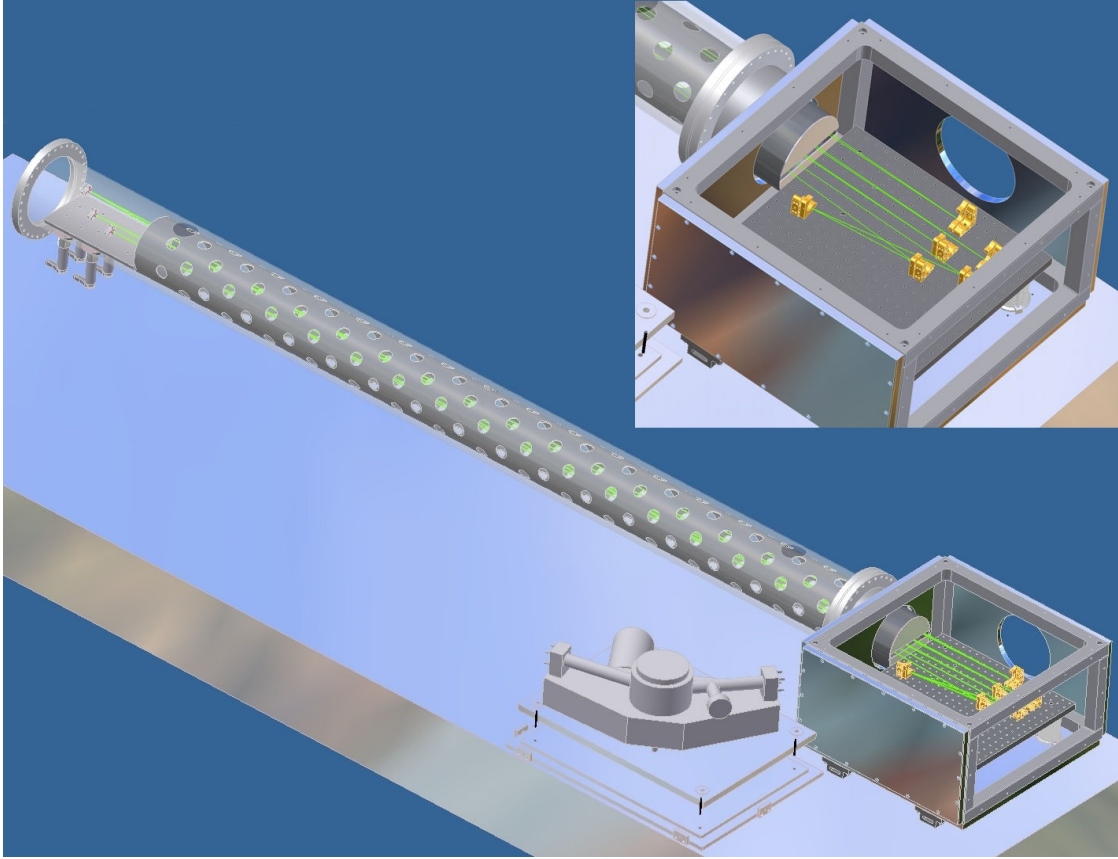


Figure 61. Computer drawing of the enhancement cavity. The main vacuum chamber (see inset) contains four folding mirrors, two focusing mirrors, the gas jet and the sapphire plate along with optics for diagnostics. Attached to the main chamber is a vacuum tube that houses a small breadboard for four folding mirrors (including the input coupler). To keep the distance between both breadboards as constant as possible a stabilizer in the form of a tube with a low temperature expansion coefficient was inserted. The tube was perforated for better vacuum pumping. The chambers are differentially pumped (TMH 1000 MP, TMH 071 YP, Pfeiffer Vacuum AG), as the only gas load is located in the main chamber. Also shown is an XUV spectrograph for the detection of frequency-converted light.

A ring cavity is employed as this simplifies the separation of the reflected beam at the input coupler from the incident beam. The reflected beam can only be picked up for locking loop detection after ~ 0.5 m because of the long overall cavity length and small angle of incidence on the mirrors.

Due to the large difference in length between the long and short cavity section, the spot sizes in the long arm would become very large in the standard bowtie setup with only two focusing mirrors. In order to keep the spot sizes reasonable and to use one inch mirrors, a telescope was introduced in the long arm. It consists of two slightly focusing

mirrors with large radius of curvature (ROC = -10.24 m), separated by approximately twice their focal length.

The stability range of the resonator is calculated using the ABCD matrix formalism for Gaussian beams [151]. The focal length of the focusing mirrors, their location in the cavity, their angle of incidence, and the thickness of the sapphire plate enter the stability calculation. The distance between the focusing mirrors in the short arm d is the stability tuning parameter, $d-2f_i = \delta$, with f_i the focal length of the mirrors in the short arm. It has to remain within certain boundaries called the stability range, to make the resonator stable. As the folding angle on the curved mirrors, as well as the sapphire plate, breaks the cylinder symmetry of the cavity (with all the planes of incidence being parallel), the ABCD matrix calculations need to be separated for the plane of incidence (tangential plane) and the plane perpendicular to it (sagittal plane). This symmetry breaking introduces astigmatism and therefore two slightly displaced foci at each cavity focus. In order to achieve high peak intensities in the short arm focus for efficient nonlinear conversion, this undesirable effect has to be minimized. The astigmatic influence of the sapphire plate and the folding angles can be made to almost cancel out and the stability ranges for both planes overlap. The result from the ABCD matrix calculations for the focal radius w_0 (1/e amplitude limit) is shown in figure 62.

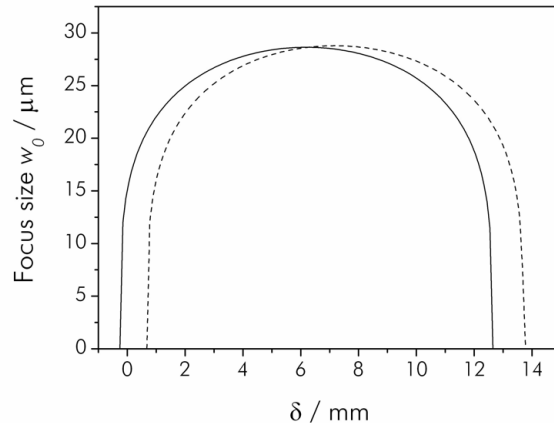


Figure 62. Cavity stability calculations with the ABCD matrix formalism. Focal spot size between f_1M mirrors. Cavity parameters are $f_1M = 15$ cm, $f_2M = 5.12$ m, sapphire plate thickness $t = 500$ μm , and the folding angles 3.5° (half-angle). Solid line denotes tangential plane, dashed line denotes sagittal plane.

In the center of the stability range w_0 is 27 μm . The ellipticity of the focus spot size remains within $\pm 5\%$ over a 6.5 mm range of the stability parameter δ . Theoretically, the focus could be made much smaller (even infinitely) at the edges of the stability range. However, in practice this is foreclosed by the finite aperture of the focusing mirrors, as the spot size there would grow without bounds. Furthermore, the beam

diameter and ellipticity would fluctuate strongly due to environmental perturbations. Thus, in practice, a setting of δ in the center of the stability range is employed.

Only one degree of freedom of the detuning of the frequency comb modes was detected. The error signal was generated by means of polarization locking detection for the reasons mentioned above (detrimental phase noise on the comb structure in the Pound-Drever-Hall scheme). The balanced detection setup after the grating was aligned such the locking point is approximately in the center of the spectrum. Feedback was given to the seeding laser where three optical elements in the cavity were piezo-actuated to control the cavity length. The key parameters of a feedback actuator are its bandwidth and dynamic range. The bandwidth is determined by the position of the first resonance of the piezo-mirror compound system. Heavier mirrors and larger piezo elements will have a smaller bandwidth. The largest dynamic range (25 μm) of the three actuators, but smallest bandwidth, is provided by the output coupler being mounted on a ring-piezoelectric transducer (HPSt 150/14-10/25, Piezomechanik GmbH). The intermediate timescale is covered by a small mirror (4 mm diameter, 1 mm thickness) mounted on a stack-type PZT. The fast timescale is covered by an even tinier mirror (1 mm³) mounted on a small PZT with 2.2 μm dynamic range (PL022.31, PI GmbH & Co. KG) which results in a bandwidth up to the first mechanical resonance at 110 kHz.

The three actuators are supplied with the processed error signal in the following way (see fig. 63): the faster actuators are connected directly to the locking electronics, while the slow PZT acting on the output coupler is connected via a second lock-box. This causes double integration of the signal in the lower frequency part and thus higher gain in this region.

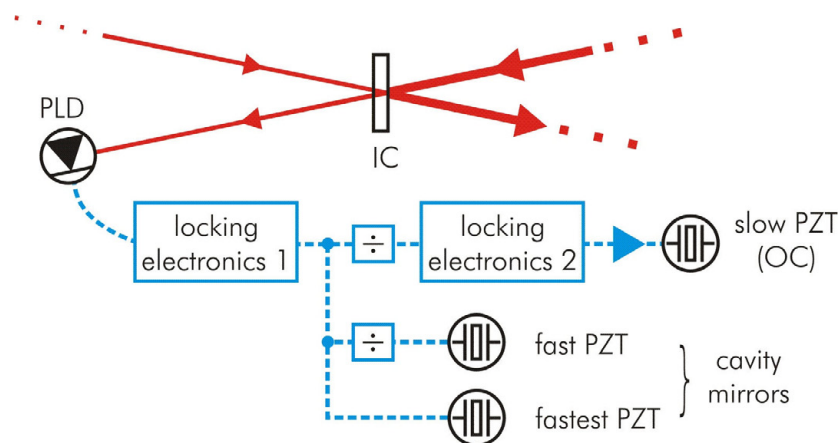


Figure 63. Schematic wiring of the feedback loop. PLD: polarization locking detection (chapt. 4.1.2); IC: input coupler; PZT: piezoelectric transducer used to actuate cavity mirrors; OC: laser output coupler.

The enhancement cavity consisted of eight high-reflecting mirrors (see chapt. 4.1.1), a dispersion-compensating chirped mirror, a 0.25% input coupler, and a 500 μm thick sapphire plate at Brewster angle. The cavity length was stabilized in the aforementioned manner while the other degree of freedom was controlled manually with one of the prisms inside the seed laser. The cavity finesse was determined with the cavity ring-down technique (chapt. 4.1.1 and ref. [75, 76]) to be approximately $F = 1100$. From this the round-trip cavity losses (excluding the input coupler transmission) can be estimated at $1-r^2 = 0.32\%$. Given these losses, the best choice of input coupler transmission for impedance-matching would be $T_{max} = 0.32\%$. The expected enhancement factor is $P = 307$ with this input coupler, for the impedance-matched case $P_{imp} = 350$.

However, the actual spectrally-averaged enhancement is only $P \approx 100$. This can be seen from the transmission of intra-cavity light through one of the cavity mirrors (fig. 60). With the precisely known transmission characteristics of the mirror, the intra-cavity power and spectrum can be determined. The circulating power is estimated at 120 W, with an incident power of 1.18 W. The missing factor in power enhancement can be attributed to a mismatch of the spatial modes of the incident and circulating light and to spectral filtering due to imperfect dispersion compensation. The incident and circulating spectra are shown in figure 64a. The circulating spectrum normalized with the seeding laser spectrum is shown in figure 64b. The three prominent peaks can be assumed to correspond to loci of perfect overlap of the incident frequency comb with the resonator modes. Therefore they were assigned a power enhancement of $P = 307$. Calculating the integral from the normalized spectrum results in an average power enhancement of 184 with the given spectral filtering. This is about 60% of the expected enhancement.

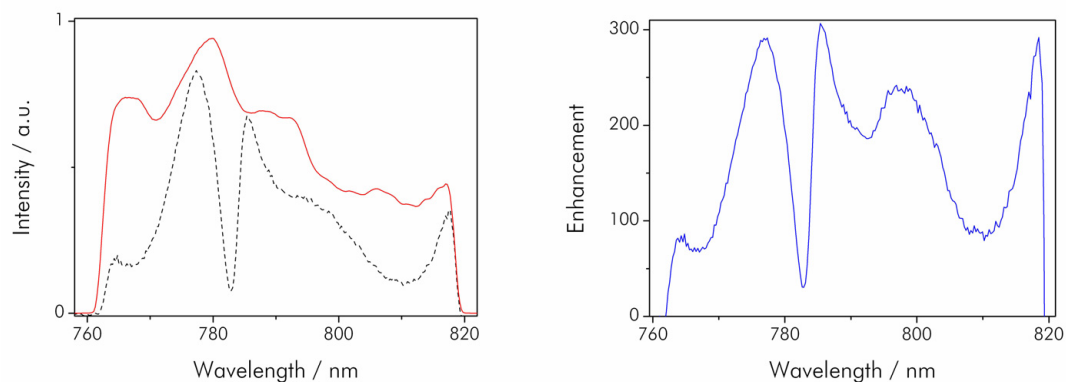


Figure 64. (a) Optical spectrum of the seed laser (red line) and circulating resonator spectrum (black dashed line). The resonator spectrum was calculated from the spectrum transmitted through a cavity mirror and measured with an optical spectrum analyzer (HR4000, Ocean Optics Inc.). (b) Intra-cavity spectrum normalized to the incident spectrum. Spectral filtering occurs mainly at 763 – 768 nm, 781 – 785 nm, and 807 – 812 nm.

Thus a resonator with perfect dispersion compensation would have an average enhancement factor of 184. The missing enhancement compared to the expected value of 307 might originate from imperfect spatial mode-matching. Further, the onset of nonlinearities in the mirror coatings or the sapphire plate could introduce detrimental phase shifts.

With the focal diameter obtained from the resonator mode calculations and the measured enhancement of 100, the intensity in the focus can be estimated at $\sim 4 \cdot 10^{13} \text{ W/cm}^2$.

4.3 Conclusions

Enhancement resonators for femtosecond pulses enable the amplification of ultrashort pulses at the full oscillator repetition rate of several tens or hundreds of megahertz. This is a factor of five orders of magnitude more than what typical amplifier systems can provide. Such cavities have been employed for the amplification of cw light for several years already. Though, compared to the enhancement of cw radiation in a passive cavity, more complex requirements have to be fulfilled to support the broad spectrum of femtosecond pulses. Starting out from the first enhancement cavities at 100 MHz repetition rate [7, 37], systems at 10 MHz and 1 GHz were designed and set up of which the former is presented in this chapter. Presently, it enhances the seed pulses from a chirped-pulse oscillator by a factor of ~ 100 , thus delivering $\sim 12 \mu\text{J}$ pulses of 35 fs duration. The intensity at one of the foci inside the resonator is estimated at $\sim 4 \cdot 10^{13} \text{ W/cm}^2$ which is sufficient for the generation of high-order harmonics (chapt. 5.2.2). Theoretically, the power enhancement could be around 350 with zero dispersion and perfect impedance matching. The gap could be narrowed significantly by further improvements to the chirped mirror.

A possible alternative to the delicate compensation of cavity dispersion could lie in the introduction of a small amount of nonlinearity to the cavity. The idea draws on the concept of mode-locked laser oscillators, where in steady-state operation the shape of the circulating pulse does not change from one round-trip to the next. This is achieved by the compensation of the dispersion from the optical elements in the cavity by nonlinearities such as the laser gain, self-amplitude modulation and self-phase modulation (SPM). Thus the suggestion arose that an increased bandwidth and thus higher circulating powers could result from the introduction of an appropriate nonlinearity to the enhancement resonator. In other words the nonlinearity relaxes the requirements on dispersion compensation which seems to be one of the major limiting factors. Numerical simulations of such an enhancement cavity showed that the soliton-like pulse is stable for a wide range of the SPM parameter [144, 152, 153]. The SPM introduced by, e.g. a thin sapphire plate, can compensate completely the second-order dispersion, while third-order dispersion still acts destructively. From the simulations it was apparent that the parameter range of dispersion (GDD and TOD) for a certain

enhancement was much larger for the nonlinear resonator than for the linear one. Also, the maximum achievable power enhancement was the same as for a dispersion-free resonator. Due to pulse-shortening effects inside the resonator, the peak power enhancement was higher for the nonlinear resonator.

With the improvements expected from the addition of a controlled amount of nonlinearity to balance the residual dispersion and the advances in high-reflecting mirror technology, enhancement resonators may further close the gap towards chirped-pulse amplifiers while keeping the repetition rate in the tens to hundreds of megahertz range.

Chapter 5

Applications

The preceding three chapters discussed the production of ultrashort near-infrared laser pulses with a controlled evolution of the electric field waveform, i.e. a stabilized CE phase. In the following, some applications that make use of these laser sources are presented. In chapter 5.1 two areas of application of the frequency comb provided by phase-stabilized oscillators (chapt. 2) are briefly presented as showcase examples. In chapters 5.2 and 5.3 *strong-field phenomena* that are driven by intense few-cycle pulses from a laser amplifier system (chapt. 3) are discussed. Chapter 5.2 introduces high-harmonic generation, a technique for frequency conversion to the XUV spectral region. In chapter 5.2.1 an alternative method for the realization of the conversion is presented. High-harmonics can also be generated inside the cavity of an enhancement resonator (chapt. 4) which is described in chapter 5.2.2. All strong-field phenomena that are triggered by few-cycle pulses are sensitive to the evolution of the electric field instead of the pulse envelope. Chapter 5.3 discusses another strong-field phenomenon, above-threshold ionization, and its dependence on the CE phase.

5.1 Spectroscopy experiments with frequency combs

As discussed in chapter 2.1, a mode-locked laser emits a spectrum that contains narrow comb lines that are equally spaced to a high degree. Measurement and stabilization of the two parameters of the frequency comb, f_{rep} and f_{CEO} , (e.g. with the technique employing a monolithic crystal, chapt. 2.3) renders the comb usable for a wide range of spectroscopy experiments.

The most prominent example is the precise measurement of optical frequencies [154]. Given that both degrees of freedom of the frequency comb are stabilized to a certain well-known value, the frequency of every comb line is known by means of the indexing equation 6. In this way a ‘ruler’ is formed in frequency space, suitable for the ‘absolute’ measurement of optical frequencies that are within the spectral bandwidth of the laser. Here, ‘absolute’ refers to the fact that such a measurement can be linked to the international definition of time and therefore also frequency. The second is defined in the SI system of units⁶ by the hyperfine splitting in the ground state of cesium-133 atoms at 9 192 631 770 Hz.

⁶ SI: Système International d’Unités. The metric international system of units monitored by the Bureau International des Poids et Mesures (BIPM).

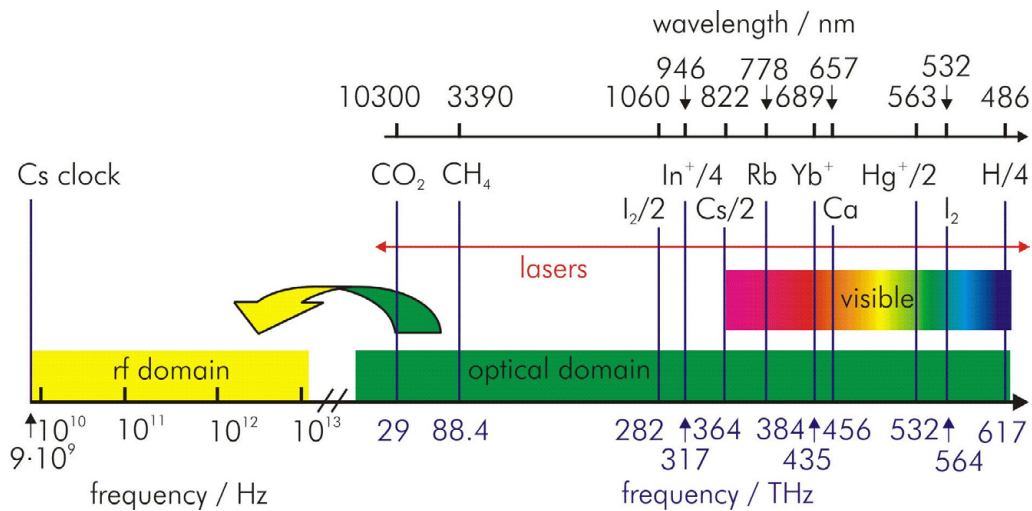


Figure 65. Map of the electromagnetic spectrum showing frequencies of several atomic and molecular reference transitions and the frequency range of laser sources. Spanning the frequency difference from the visible portion of the spectrum to the Cs clock time standard is now facilitated by the use of the frequency comb.

By using a Cs atomic clock as the reference for the phase-locking loops of the comb parameters, the link between the time standard (in the rf region) and optical frequencies (in the PHz region) is established.

Before the invention of methods for stabilizing the frequency comb, bridging this frequency gap of approximately five orders of magnitude was a complex and resource-consuming task involving *harmonic frequency chains*. These chains started with an atomic clock from which higher harmonics were generated in nonlinear diode mixers, crystals and other nonlinear devices. Phase-locked transfer oscillators were needed between steps to boost the power for the following nonlinear step. Apart from the immense efforts required to build and operate such a system, their use was limited to the measurement of just one single optical frequency. Consequently, only a few harmonic chains have ever been constructed [155].

Using a frequency comb, referenced to a time standard (e.g. an atomic clock), as a precise ruler in frequency space covering the entire visible to near infrared part of the electromagnetic spectrum greatly simplifies optical frequency metrology. This resulted in a large number of precision measurements in the last couple of years, e.g. in atomic hydrogen [31], Hg⁺ and Ca [156], In⁺ [157] or Rb [158]. Figure 65 shows some of the measured transitions in the optical frequency domain.

The recent measurement of the $6s - 8s$ transition in cesium [159] at MPQ may serve as a showcase example to illustrate the technique. The energy levels involved are shown in figure 66. When Cs-atoms are excited to the $8s$ state, a fraction of them decay via the $7p$ state back to the ground state.

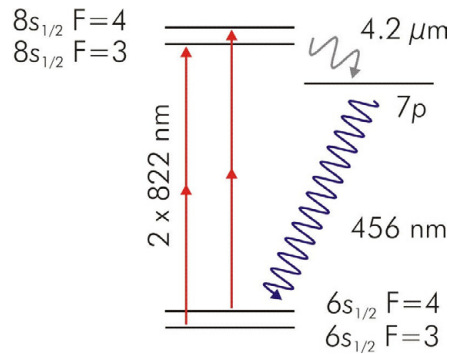


Figure 66. Partial energy diagram of Cs showing the $6s - 8s$ two-photon transition.

The emitted photons can be detected with a photomultiplier. Recording the photon count rate while scanning the frequency of the laser used to excite the transition gives a precise measurement of the transition frequency. However, this is only true if the frequency of the excitation laser is known accurately, which is accomplished by a self-referenced frequency comb clockwork. Figure 67 shows a cut-down version of the setup. A mode-locked picosecond Ti:sapphire laser is employed to excite the transition. Picosecond pulses are used, as the longer pulses reduce time-of-flight broadening and the narrower spectrum compared to femtosecond pulses does not overlap with undesired transitions, in that way simplifying the measurement. The center frequency is stabilized to an optical reference cavity, thus phase-locking a combination of f_{rep} and f_{CEO} . Additionally, f_{rep} is phase-locked to a Cs clock-referenced local oscillator. In this way the comb of the picosecond laser is stabilized, though the offset frequency remains unknown. At this point the offset frequency stabilization technique comes into play: detecting the heterodyne beat between the frequency comb of the picosecond laser and an octave-spanning femtosecond frequency comb referenced to the Cs clock enables the measurement of f_{CEO} . The femtosecond frequency comb serves as optical clockwork to reference the picosecond laser to the Cs atomic clock. The comb lines from the picosecond laser are frequency-shifted by means of an acousto-optic modulator and in so doing, the transition is scanned. The pulses traverse the cesium probe cell in a double pass configuration. A suitably positioned retro-reflector ensures that two counter-propagating pulses collide inside the cell. This enables the Doppler-free excitation of the two-photon transition at 822 nm. Recording the photon count rate from the $7p - 6s$ fluorescence while simultaneously scanning the frequency comb (and measuring the beating frequency between picosecond comb and clockwork) reveals a Lorentzian line shape. With this technique, the absolute frequency of the Cs $6s - 8s$ two-photon transition was measured with an uncertainty six times smaller than previous work.

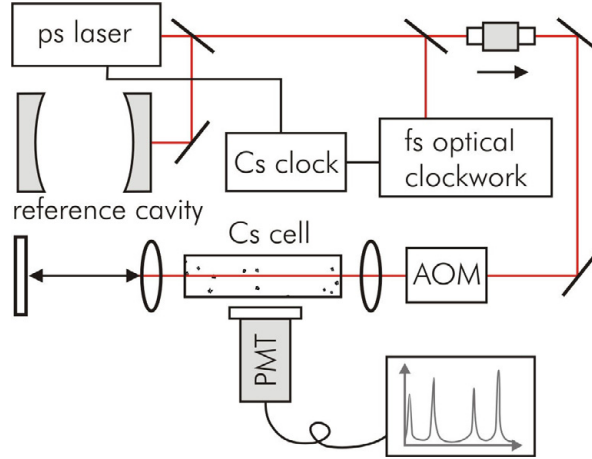


Figure 67. Simplified representation of the setup for spectroscopy on the $6s - 8s$ transition in cesium. The laser frequency is shifted using an acousto-optic modulator (AOM). The distance between the retro-reflecting mirror and the cell is $c / 2 f_{rep}$, so that two counter-propagating pulses collide inside the cell. An optical isolator is used to prevent the back-reflected light from going back into the laser. The photo-multiplier tube (PMT) is detecting the photons emitted via the $7p - 6s$ decay channel.

When measuring the cesium transition, like in all optical frequency metrology experiments, the frequency comb was used to transfer the time standard from the rf region to the optical region. However, it is also possible to use the frequency comb transfer mechanism in the other direction, namely as clockwork in an *optical atomic clock*. Just like any other clock, an atomic clock consists of an oscillator (‘pendulum’) that defines the ticks in time and a counter that counts those ticks. In case of an optical atomic clock, an optical transition serves as the clock’s pendulum and the frequency comb acts as the link to connect phase-coherently to the clock’s counter. In practice, this is realized by phase-locking the offset frequency f_{CEO} to a fraction k of the repetition frequency f_{rep} of the mode-locked oscillator:

$$f_n = n f_{rep} + f_{CEO} = (n + 1/k) f_{rep}. \quad \text{Eq. 39}$$

A suitable comb line f_n is then locked to the optical transition line of choice. The large integer n acts as the transfer coefficient, when the cycles of the repetition frequency are counted.

Obviously, a clock becomes more accurate, the higher the oscillation frequency, simply because time is divided into smaller pieces. Therefore, redefining the second in terms of an optical frequency transition, rather than the rf frequency Cs transition currently used, has been a long-standing goal. The advantage is straightforward: to first order, the uncertainty is inversely proportional to the number of cycles counted during

a measurement. This means that increasing the frequency of a clock allows a measurement with a certain statistical error to be made in a shorter time. This corresponds to an improvement of up to the ratio of the frequencies of the Cs and the optical standard.

With the development of frequency comb stabilization techniques, a reliable optical atomic clock has come into reach [160]. Owing to the simplicity of the system, compared to previous harmonic frequency chains, it can run for hours and may eventually become a truly turn-key system.

Controlling the frequency comb evidently also means controlling the waveform of the electric field of an ultrashort laser pulse. Therefore, the advent of offset frequency stabilization techniques also had a great impact on ultrafast physics. Generally speaking, the control of the CE phase enables the study of highly nonlinear phenomena in the time domain. CE phase-sensitive processes such as above-threshold ionization, photoemission or high-order harmonic generation have become the focus of interest. However, almost all of these processes require high peak intensities that cannot be delivered by laser oscillators presently but require an amplifier system. The generation of intense few-cycle pulses in an amplifier equipped with a CE phase-stabilized oscillator and a secondary stabilization loop (chapt. 3) has enabled the study of these phase-sensitive phenomena. Two examples will be discussed in the next chapters.

5.2 High-order harmonic generation

CE phase-stabilized amplified ultrashort pulses are employed to study various high-field phenomena. Amongst the ones most intensely exploited is the generation of XUV light by the non-perturbative mechanism of high-order harmonic generation (HHG). Focusing intense ($>5 \cdot 10^{13} \text{ W/cm}^2$) laser pulses into a gaseous medium produces high-order harmonics of the laser frequency that are emitted as a coherent beam in the laser direction.

HHG can be described using a semi-classical three-step model (see fig. 68) [161] or a quantum version [162]. In the first step, an atom (usually a noble gas) or molecule in the laser field is *tunnel ionized*, releasing an electron into the continuum. This occurs at or slightly after the maxima of the electric field half-cycles in the pulse that are strong enough to overcome the effective binding potential. In a first approximation, the ionized electron can be considered as born in the continuum with zero velocity.

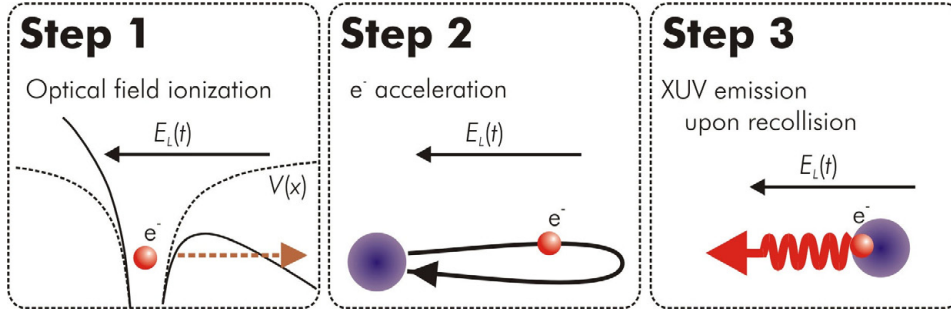


Figure 68. Schematic of the three-step model for harmonic generation in gases. Step 1, the Coulomb barrier $V(x)$ (dashed line) is temporarily bent down by the laser field $E_L(t)$. An outer-shell valence electron can tunnel through the barrier formed by the superposition of the Coulomb field and the instantaneous laser field (solid curve); step 2, acceleration by the linearly polarized laser field in the continuum, along a trajectory typical of an oscillating free electron; step 3, radiative recombination occurs when the electron is set free at or slightly after the maximum of the electric field half-cycle.

The intensity regime where tunneling occurs is characterized by the so-called Keldysh parameter [163]

$$\gamma = \sqrt{\frac{I_p}{2U_p}} \quad \text{Eq. 40}$$

being smaller than one. Here I_p is the ionization potential of the atom and U_p is the ponderomotive quiver energy of the electron in the laser field. U_p , the average kinetic energy of the accelerated electrons, is given (in eV) by

$$U_p = \frac{e^2 E_0^2}{4\omega^2 m_e} = \frac{e^2}{4\omega^2 m_e} \frac{2I}{c \epsilon_0} \cong 9.33 \cdot 10^{-14} I \lambda^2 \quad \text{Eq. 41}$$

where $\epsilon_0 = 8.85 \cdot 10^{-12}$ F/m is the vacuum permittivity, λ the wavelength of the laser light in μm , and I its intensity in W/cm^2 .

For values of the Keldysh parameter much higher than one, the field ionization rate is dominated by multi-photon absorption. HHG is typically conducted in the intermediate region of $\gamma \approx 1$, which translates to intensities of $5 \cdot 10^{13}$ to $1 \cdot 10^{14}$ W/cm^2 for the typically used noble gases.

In the second step, this electron is *accelerated* by the laser field $E_L(t)$ and can gain considerable kinetic energy. The oscillation amplitude of the electron in this step can be calculated (in m) by

$$A = \frac{e E_0}{m_e \omega^2} = 2.56 \cdot 10^6 \sqrt{I} \lambda^2 a_0 \quad \text{Eq. 42}$$

where e is the electron charge, m_e its mass, E_0 the electric field amplitude, ω the frequency of the laser light, λ the wavelength in m, and I its intensity in W/cm^2 , and $a_0 = 5.29 \cdot 10^{-11}$ m the Bohr radius.

In the third step, the electron is driven back to the core approximately three-quarters of an optical cycle after it was ionized, where it can *recombine* emitting a photon of energy equal to the sum of its kinetic energy and the ionization potential I_p of the system. In fact, the electron can recollide with a range of kinetic energies that correspond to a spread of possible ionization times in the laser field. Different ionization times lead to different semi-classical electron trajectories. This results in a broad emission spectrum.

The repetition of this process in multi-cycle laser pulses leads to a spectral comb of harmonics that extends over many orders up to a high-frequency cut-off. The photon energy at the cut-off can be estimated using

$$E_{\text{cutoff}} = I_p + 3.17 U_p. \quad \text{Eq. 43}$$

For a few-cycle pulse, the electric-field extrema vary significantly from one half-cycle to the next. As a consequence, each half-cycle produces an HHG spectrum with a cut-off dependent on the amplitude of the half-cycle electric-field extremum (fig. 69).

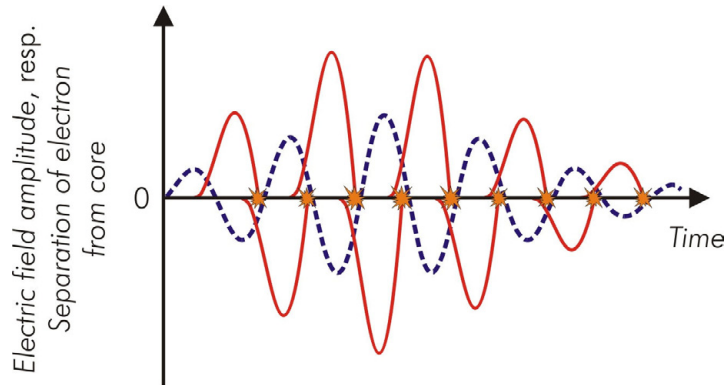


Figure 69. Sketch of the temporal distribution of HHG in a few-cycle laser pulse. The electric field of a two-cycle laser pulse (dashed blue line) is shown with the corresponding electron trajectories. Owing to the trajectory dependence on the history of field amplitudes, electrons released at different instants undergo a different amount of acceleration and therefore every half-cycle has a different cutoff energy.

Due to the strict periodicity and spatial symmetry of the process only harmonics of odd number are generated. Even harmonics from neighboring half-cycles interfere destructively due to the change of direction. However, this applies only to media with inversion symmetry, like gaseous media. In contrast, HHG from solid surfaces yields odd and even harmonics when illuminated with a p-polarized laser beam, because the surface breaks the inversion symmetry.

The efficiency of the HHG process is about $\eta = 10^{-7}$ to 10^{-9} , depending on laser pulse width, the cross-section of the gas medium, the XUV spectral range considered and in particular the phase-matching in the gas. The ionization of the gas, accompanying HHG generates a free-electron plasma that causes a phase-mismatch due to altered dispersion. The electron plasma dispersion relation is given by

$$k(\omega) = \frac{\omega}{c} \sqrt{1 - \frac{\omega_{pl}^2}{\omega^2}} \quad \text{Eq. 44}$$

where ω_{pl} is the plasma frequency. As this dispersion relation approaches the one for vacuum with increasing frequency, the effect of the plasma is largest for the fundamental wave and diminishes with ascending harmonic orders.

Furthermore, the Gouy phase [164], the phase shift of the beam at the focus creates a phase-mismatch and reduces efficiency.

Many efforts have been undertaken to improve the efficiency, among others by using quasi-phase-matching in modulated hollow waveguides [165] or by placing gas targets in a row, separated by twice the coherence length (see fig. 22). Moreover, using a standing wave instead of a traveling wave is expected to boost the conversion efficiency. This can be accomplished by placing the gas jet in an enhancement cavity (see chapt. 5.2.2).

Another way to improve the efficiency of HHG could be to increase the number of particles that are contributing in the nonlinear process. Yet, the particle density in the gas target cannot be raised easily, as this would also cause higher absorption of the generated XUV photons. As an alternative, HHG from surfaces was proposed [166], using the same mechanism as in a gas target (depicted in fig. 68).

5.2.1 High harmonic generation from surfaces

High-order harmonics from surfaces have been produced [167], however only in the so-called oscillating plasma mirror regime [168] that requires high laser intensities ($>10^{18}$ W/cm²). There, the target surface is highly ionized by the leading edge of the laser pulse, and a reflecting layer of plasma is formed. The collective electron motion created by the incident electromagnetic wave can be regarded as an oscillating mirror.

The phase modulation of the reflected light introduced by this mirror gives rise to harmonic frequencies. Due to the plasma formation, optical breakdown occurs and the target (usually glass) has to be moved for every shot. Here, HHG from a surface with the same generation process as in a gas target using moderate laser intensities shall be treated and first experimental results presented.

Using a solid, instead of a gas target for HHG holds the potential of increased efficiency, as more atoms or molecules can participate in the process due to the higher density. Comparing a typical solid (e.g. diamond or fused silica, SiO_2) with a noble gas (at 200 mbar backing pressure), the particle density is four orders of magnitude higher in the solid.

On the other hand, the HHG process will only take place at or close to the illuminated surface. This is due to the fact that the excursions of the electron during the acceleration step (in the semi-classical picture) are approximately 1 nm for the intensities considered here (cf. eq. 42 with $I = 5 \cdot 10^{13} \text{ W/cm}^2$) and therefore much larger than the average distance between atoms in a solid, which are e.g. 3 Å for fused silica. Furthermore the high absorption of the XUV photons inside the solid state material impedes the HHG process inside the solid.

Assuming suitable focusing conditions for reaching the required intensity (while avoiding damage), a layer on the order of 1 nm in the solid target comprises the same amount of particles as the interaction volume in a gas target with 2 mm interaction length. Therefore, only several (~9) of the uppermost atomic layers would have to contribute to the HHG process to rival the gas target. For most materials, the skin depth of the evanescent field in the solid is far larger than that.

In addition to the potential for increased efficiency, HHG from solid state surfaces has the advantage of reducing the background pressure in the vacuum chamber. This in turn means lower absorption of the generated XUV photons and very pragmatically lower demand on the turbomolecular vacuum pumps.

A thorough literature study has not provided evidence that such HHG with non-relativistic laser intensities has been attempted before. Apart from the publications reporting harmonic generation at intensities of more than 10^{17} W/cm^2 using the plasma mirror [167], only photoemission from surfaces at moderate intensities is described [169]. The authors used 40 fs laser pulses with intensities of 0.5 to 6 TW/cm^2 and wide-bandgap crystals (CsI, diamond) to generate spectra up to a cut-off at 40 eV. This indicates that HHG from surfaces might be possible at non-relativistic intensities.

Two theoretical publications have dealt with HHG from solid surfaces at moderate laser intensities [170, 171]. They use a three-dimensional quasi-free electron model, where the effective electron masses take into account the periodic structure of the medium. Within this approximation, it is assumed that the electron in the crystal moves freely. The model relates HHG with the recombination process of photoelectrons to the evanescent part of the electron wave function in the vacuum during the rescattering process with the surface.

Material	Bandgap energy / eV
SiO ₂ (fused silica)	8.9 (ref. [172])
AlN	6.2 (direct bandgap)
C (diamond)	6
Na	5.1
Al ₂ O ₃ (sapphire)	5
InAlGaN	~4
AlGaN	3.8
GaN	3.4 (direct bandgap)
SrTiO ₃	3.4
InGaN	3.1
SiC	2.2 – 3.25
ZnSe	2.6
GaP	2.26
CsI	2.2 (ref. [173])

Table 1. Survey of wide-bandgap materials.

As a case study, a sodium surface is employed. It is illuminated with laser light at 800 nm wavelength with an intensity of 10^{13} W/cm² at an angle of incidence of 60°. The resulting calculated spectrum shows a plateau, just as expected for an HHG process. Efficiencies of $\eta = 10^{-4}$ for the 5th harmonic (in the plateau) and 10^{-7} for the 10th harmonic (in the cut-off) are estimated. These numbers are comparable to those from gas targets, but one must recall that the theoretical model only accounts for effects at the very surface; evanescence of the electric field into the solid is not taken into account. Further simulation results show that the higher-order harmonics (>15th order) are radiated predominantly parallel to the surface and in the direction perpendicular to the plane of incidence of the laser. Harmonics from the plateau are almost isotropically distributed.

The choice of sodium for the published simulation results poses the question of target materials. In a first attempt, materials with a large energy band gap, high optical breakdown threshold and high surface quality were selected. The requirement of a large bandgap is motivated by the dependence of the maximum photon energy (cut-off) achievable through HHG on the ionization potential. Table 1 shows a selection of wide-bandgap materials. In order to avoid the immediate absorption of the generated photons, a material with high transmission in the wavelength range of interest has to be chosen. Figure 70a shows absorption curves for the XUV wavelength range for some of the materials in table 1.

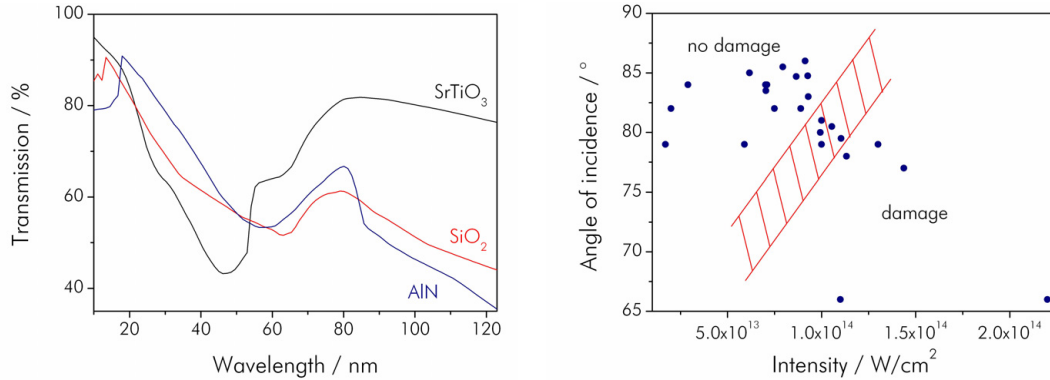


Figure 70. (a) Calculated transmission of a 10 nm layer of a wide-bandgap material (AlN, SrTiO₃, SiO₂) in the XUV wavelength region [174]. (b) Damage threshold study of a fused silica sample. The super-polished sample (surface flatness better than $\lambda/10 \approx 63$ nm) was irradiated in vacuum (pressure $\sim 5 \cdot 10^{-3}$ mbar) under grazing incidence ($66 - 86^\circ$) with 8 fs laser pulses. After each parameter setting, the sample was investigated with an optical microscope. A transition zone is marked in red where damage occasionally occurs. The spot size in the focus was verified with a beam profiler.

For the following experiments, a fused silica sample was irradiated under grazing incidence with intense few-cycle laser pulses. Fused silica was chosen, as samples with high surface quality are easily available. Grazing incidence was chosen in order to maximize the contribution of the electric field vector that is normal to the target surface. This should maximize the overlap of the incident electric field with the evanescent electron wave function in vacuum.

For the realization of HHG from surfaces below the onset of plasma formation, it is important to know the optical breakdown threshold precisely. Due to surface field enhancement, optical damage in a bulk material occurs first at the surface. The surface optical breakdown threshold was studied in ref. [175] with laser pulses of 120 fs duration. In fused silica breakdown occurred at $1 \cdot 10^{13}$ W/cm². The authors infer that the measured thresholds are affected by surface imperfections, such as scratches, cracks, grooves, and chemical contamination. A similar value for fused silica is also given in ref. [176], as well as the dependence of the optical breakdown threshold on the pulse duration: an 8 fs pulse raises the threshold to $\sim 1.7 \cdot 10^{14}$ W/cm².

With a laser amplifier system similar to the one described in chapter 3.1, the damage threshold of fused silica was measured. Illuminating a super-polished sample of fused silica (surface flatness better than $\lambda/10 \approx 63$ nm) with 8 fs laser pulses under grazing incidence yielded the results shown in figure 70b. Like the published value, they indicate a damage threshold of $\sim 1 \cdot 10^{14}$ W/cm².

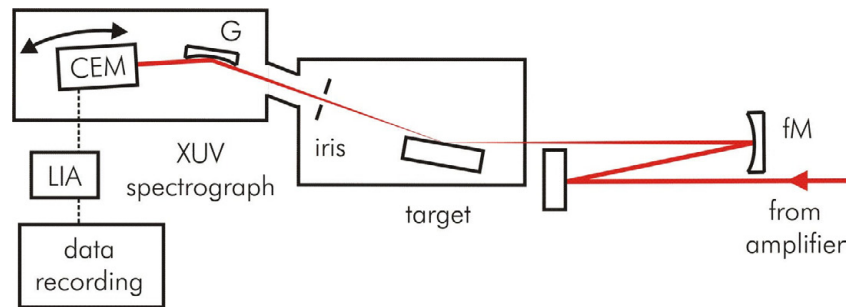


Figure 71. Setup for HHG from surfaces. The incident laser pulses have a duration of ~ 8 fs and a per-pulse energy of ~ 250 μJ at a repetition rate of 1 kHz. The vacuum in the target and detection chambers was $2 \cdot 10^{-3}$ mbar and $9 \cdot 10^{-6}$ mbar, respectively. CEM: channel electron multiplier, wavelength range 10 – 130 nm, photon detection efficiency $\sim 30\%$ at 50 – 150 nm (CEM 4751G, Burle Inc.), fM: focusing mirror, ROC = -500 mm; G: concave grating, 300 G/mm, platinum coated, ROC = -1000 mm, wavelength range 1 – 140 nm; XUV spectrograph: 88° grazing angle of incidence, Rowland circle 1 m (248/310G, McPherson Inc.); LIA: analog lock-in-amplifier (5209, EG&G Signal Recovery Inc.).

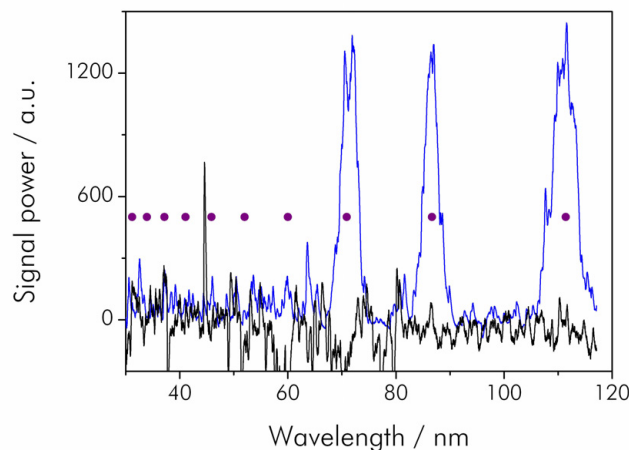


Figure 72. XUV spectrum of harmonics from a fused silica surface. Blue line shows an average of three scans. Black line shows the background, measured with a 5 μm thick pellicle in the beam 10 cm after the target. The signal-to-noise ratio is ~ 11 . The purple dots mark the position of the odd harmonics, calculated from a center frequency of the fundamental spectrum of 780 nm. The intensity on-target of the 8 fs laser pulses was estimated at $\sim 8 \cdot 10^{13}$ W/cm^2 at an angle of incidence of $\sim 85^\circ$. The channeltron bias was 2.6 kV, resulting in an electron gain of $\sim 2 \cdot 10^6$. Integration time of the lock-in amplifier was 10 s, together with a scan speed of 0.6 inches/min resulting in a spectral resolution of 2 nm.

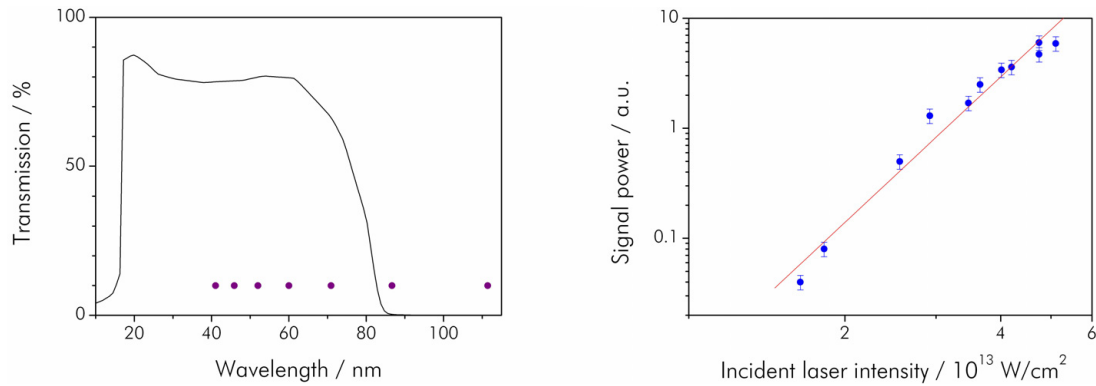


Figure 73. (a) Calculated transmission of an aluminum filter of 100 nm thickness in the XUV spectral range. Purple dots show the position of the 7th to 19th harmonic at a center wavelength of 780 nm [174]. (b) Power scaling of the 11th harmonic at 71 nm. The grating was removed and the channeltron placed directly in the XUV beam. An aluminum filter (Lebow Company) of 100 nm thickness was inserted to block lower order harmonics and the fundamental light. From the measured spectrum it is known that the major contribution stems from the 11th harmonic. The red line is a power law fit to the data with an exponent of 4.4. The 10 fs laser pulses were incident at 85°. The bias voltage of the channeltron was 2.6 kV.

In order to characterize the generated XUV light, a scanning XUV spectrograph (248/310G, McPherson Inc.) was installed after the target in the direction of the reflected beam (see fig. 71). It consists mainly of a 300 G/mm-grating and a movable channeltron detector. The signal from the channeltron is fed to a lock-in-amplifier triggered by the laser repetition rate and logged by a computer. The target was set up in a vacuum chamber to prevent absorption of the XUV light and the formation of plasma in air. Figure 72 shows an XUV spectrum recorded in the described manner. Odd harmonics of 7th, 9th, and 11th order are clearly visible, which is in contrast to the theoretical prediction that odd and even harmonics are generated at the surface due to the lack of inversion symmetry. The cut-off of the spectrum is calculated according to equation 43 at 63 nm. In order to get an estimate of the total power and the power scaling as a function of peak intensity, the monochromator was removed and the channeltron placed directly in the beam path. An aluminum filter of 100 nm thickness was inserted that transmits only in the wavelength range of 17 – 80 nm (see fig. 73a) and in particular blocks the infrared light efficiently. Thus, only the 11th harmonic can reach the detector. Additionally, the channeltron is insensitive to the infrared laser light. A rough knife-edge measurement confirmed that the XUV radiation is confined to the center of the reflected fundamental beam, as expected (but in contrast to the results in ref. [171]). The channeltron photocurrent measured for different laser intensities shows a clear nonlinear behavior (fig. 73b). The estimated exponent of the intensity scaling of 4.4 indicates that the 11th harmonic belongs to the plateau region of the XUV spectrum. The maximum photocurrent is ~6 pA across the input impedance

of 100 M Ω at a bias voltage of 2.6 kV, which indicates a generated power in the 11th harmonic of about a few femtowatts. This means that the efficiency of the HHG process to this particular harmonic is $\sim 10^{-14}$. However, this estimate contains several uncertainties, most notably the transmission of the aluminum filter which theoretically is 67% for the 11th harmonic, but in reality can be reduced dramatically by oxidation or other impurities.

This low power might be improved by one of the following measures: Due to the destructive interference of the incident with the reflected beam in the focus area, a different focusing geometry might be more suitable. Calculations indicate that less grazing angles close to the Brewster angle maximize the electric field strength at the surface.

Additionally, phase-matching could improve the situation. As fused silica is an amorphous material, no Bragg condition for phase-matching has to be fulfilled. Using a target material with a lattice structure, such as diamond or AlN and adjusting the angle of incidence to fulfill the Bragg equation may be useful (as was proposed in ref. [177] for relativistic intensities).

5.2.2 High-order harmonic generation in an enhancement cavity

High harmonic generation is a powerful tool for the phase-coherent conversion of light to the XUV region. Thus one could think of using HHG for extending optical frequency metrology (as discussed in chapter 5.1) to these shorter wavelengths. This would open up the study of a whole new world of transition lines – however the typically used chirped-pulse amplifiers for driving the HHG process destroy the comb structure during amplification. This is because the pulse repetition rate is reduced by a pulse picker and thus the spacing of the comb lines is too narrow to be useable for spectroscopic purposes. As a consequence, an amplification method is necessary that keeps the repetition frequency of the seeding oscillator while reaching the intensities required for HHG. Enhancement cavities for femtosecond pulses as presented in chapter 4 can fulfill both requirements and constitute a major step towards a useful frequency comb in the XUV spectral region.

In contrast to the usual HHG schemes, such an enhancement cavity has the benefit that the power that is not converted into the XUV after a single pass through the medium is ‘recycled’ and can contribute in subsequent passes, so that higher total conversion efficiencies than for conventional schemes can be expected.

Yet, the fact that the high intensity exists only within a carefully balanced resonator imposes additional obstacles to the production of XUV light by HHG.

Firstly, placing a gas jet at a cavity focus introduces additional dispersion to the circulating infrared light and thus may reduce the enhancement factor if not being compensated for. Due to the strong ionization of the gaseous medium, its dispersion is dominated by the contribution from the plasma as given by equation 44. Fluctuations in the plasma density make the compensation of this dispersion contribution impossible and thus add phase noise to both the fundamental as well as the XUV light. Plasma density fluctuations may arise from gas density fluctuations as well as fundamental laser intensity fluctuations. The plasma dispersion also affects the generated XUV light, however it scales (linearly) with the frequency of the light, thus the effect is much weaker there.

Secondly, another obstacle is given by the fact that the XUV radiation is emitted collinearly with the driving light. Hence, some sort of beamsplitter that separates the infrared from the XUV light is necessary. The usual approach of a specially designed dielectric cavity mirror that transmits the desired wavelength region is not feasible as XUV light is strongly absorbed by all common substrate and coating materials. On the other hand, several optical materials exist that provide considerable Fresnel reflection coefficients in the XUV (due to the refractive index being smaller than one) which could be used to couple out the upconverted light from the cavity. With this configuration a strong limitation of choice of a beamsplitter is given by the low-loss criterion for the fundamental infrared light that is transmitted so that cavity finesse is not compromised. When placed at Brewster angle, for instance a sapphire plate has a reflectance in the XUV as shown in figure 74. The small reflectivity with at most 18% originates from the absorption of the penetrating evanescent wave by the sapphire. The most promising alternative materials are silicon carbide (SiC) and diamond (C) whose reflection coefficients at 60 nm are higher at ~63% and ~48%. Yet these materials are hard to obtain in high optical quality and without impurities.

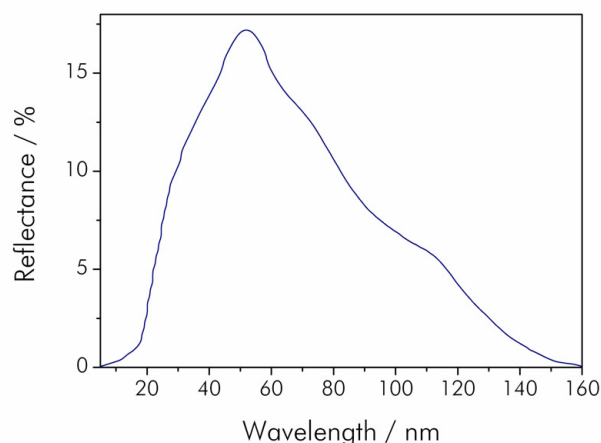


Figure 74. Fresnel reflectivity of sapphire for p-polarized light incident at the Brewster angle ($\theta = 60.4^\circ$ at 800 nm wavelength).

An alternative way for coupling the XUV light out of the resonator was proposed recently [178]: As the divergence of the generated harmonics scales as $1/n$ with n the harmonic order (assuming a Gaussian spatial profile), high-order harmonics have a divergence much smaller than the fundamental beam. A tiny hole in the concave mirror right after the gas target passes the less divergent XUV beam while almost the entire fundamental light is reflected by the mirror. Still this introduces notable losses to the cavity, as the peak intensity maximum is on axis, exactly where the hole in the mirror is located. Therefore it was further proposed to employ higher order cavity modes, such as TEM_{01} and TEM_{10} which have an intensity minimum on axis. However, several challenges arise: Firstly, generating such a higher order mode directly from the seeding laser is difficult, so that phase-masks have to be employed. Further, the peak intensity in such a donut-mode is only 74% of the intensity of a TEM_{00} mode, which will result in a significant reduction in the HHG yield. Also, the XUV light is produced in two lobes due to the two intensity maxima in the spatial profile. Another issue is the tricky alignment of the HHG beam through the tiny hole in the mirror. Due to these reasons, so far only the third harmonic was coupled out by a holey mirror.

An enhancement cavity similar to the one described in chapter 4 but operating at 100 MHz repetition rate with average circulating power 38 W was used to characterize the generated XUV light [7]. As not the whole resonator was installed in a vacuum setup, a small chamber that contained the gas jet was placed at the intra-cavity focus in the short cavity arm. The focus size was estimated with a diameter of $5.3 \mu\text{m}$ with a peak intensity on-axis of $5 \cdot 10^{13} \text{ W/cm}^2$. Figure 75 shows a close-up view of this part of the setup.

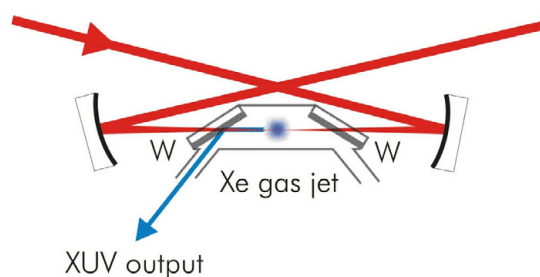


Figure 75. Close-up of the interaction zone of the enhancement cavity. The gas jet is housed by small vacuum chamber with two windows (W) made from sapphire with 1 mm thickness. The generated XUV light may be detected at the XUV output port. The gas jet is provided by a glass capillary with $\sim 50 \mu\text{m}$ inner diameter and 1 bar backing pressure.

One of the Brewster-angled windows of this chamber was made of sapphire of 1 mm thickness and thus simultaneously acted as a beamsplitter for out-coupling the XUV radiation. The losses per window are about 10^{-3} so that the cavity enhancement was not compromised ($P = 54$ for this cavity). The peak intensity in these windows was estimated to be below 10 GW/cm^2 , so that their nonlinear response is negligible. Xenon gas is injected into the focus of the resonator mode in the HHG chamber, using a glass capillary placed right above the focus with $\sim 50 \mu\text{m}$ inner diameter and 1 bar backing pressure. This diameter is approximately matched to the Rayleigh range of the focus of about $110 \mu\text{m}$. With this focus geometry and repetition rate, the atoms see about five pulses before leaving the focus.

The XUV light generated in the gas jet and extracted by the sapphire window was analyzed in a similar manner as in the previous chapter. The same scanning grazing incidence spectrograph was installed at the exit port of the small vacuum chamber. The signal from the channeltron was analyzed with (1) a photon counter (SR400, Stanford Research Inc.) for high sensitivity measurements, and (2) a voltmeter across a $1 \text{ M}\Omega$ load resistance for XUV photon flux measurements.

With the photon counter, a spectrum as shown in figure 76 was recorded. The short wavelength section of the spectrum was recorded with a $0.1 \mu\text{m}$ aluminum filter in the beam path to reduce stray light from the fundamental and the lower order harmonics. High harmonics up to 15^{th} order or 23 eV photon energy (as expected for the intensity in the focus) are observed, with an exponential roll-off starting around the ninth harmonic, presumably due to increasing phase mismatch. The cut-off wavelength of the XUV spectrometer around 120 nm prevented the observation of the 5^{th} harmonic.

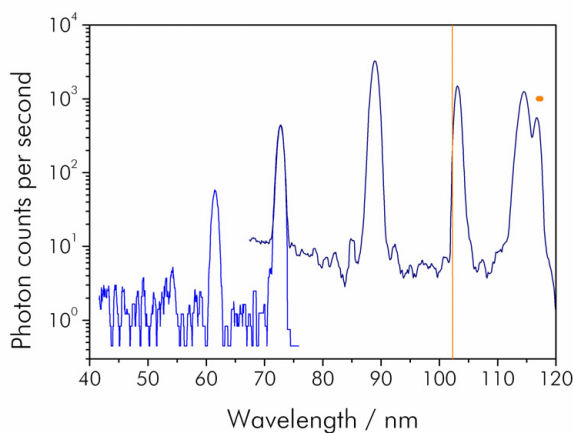


Figure 76. Harmonic spectrum with the cavity in lock, recorded with a channeltron (CEM 4751G, Burle Inc.) connected to a photon counter (SR400, Stanford Research Inc.). The short-wavelength end of the spectrum (blue) is taken with a $0.1 \mu\text{m}$ aluminum filter in the beam path to reduce stray light from the stronger lower harmonics, and is rescaled to match the peak height at the eleventh harmonic of the measurement without filter (purple). Orange dots indicate the $5P-7S$ resonance in xenon that modifies the shape of the seventh harmonic, and the vertical line indicates the ionization potential at 103 nm . The spectral feature just below the ionization limit presumably originates from fluorescence of coherently excited Rydberg states.

With the channeltron placed directly in the XUV beam without the monochromator in between, the total power in the observed XUV spectrum was determined with the voltmeter. A photocurrent of 1 mA was detected at 1.36 kV bias, which corresponds to a photon flux of about $0.85 \cdot 10^9$ photons per second, according to the manufacturer's specifications. From the spectrum it is known that the major contributions to that flux come from the spectral range between 85 and 115 nm, so an average photon energy of about 12 eV can be assumed, from which the total power can be calculated. In the spectral range from 120 nm down to 60 nm, the total power was determined to be more than 1 nW after the sapphire window. If the calculated coupling efficiency of the window is taken into account, the power in the harmonics is estimated to be 10, 1, and 0.01 nW for the 9th, 11th, and 13th order, respectively. On average, more than 10^{-8} of the power from the seeding laser is converted into photons in the 60 – 120 nm range. This is comparable to the typical efficiencies obtained from gas jet HHG with chirped-pulse amplifiers.

As mentioned above, a build-up cavity holds the potential of increased efficiency in the HHG process due to the recycling effect. The enhancement cavity discussed in chapter 4 with a finesse exceeding 1000, seeded by a high-power chirped-pulse oscillator is expected to provide higher XUV photon flux as well as an increase in conversion efficiency η . As the peak intensity in the focus is approximately the same, no change in the cut-off energy is likely. The longer focal lengths in the 10 MHz system provide a larger interaction volume for the HHG process. Further, the detrimental effect of the Gouy phase, the phase shift in the focus, is greatly reduced, thus improving the phase-matching of HHG. Combining both effects and neglecting saturation effects (e.g. due to ionization) yields a scaling law of the XUV power for plateau harmonics $P_{XUV} = \eta P \sim b^3 \tau P$, where P is the average fundamental power, b the confocal parameter, and τ the intra-cavity pulse duration [179]. Inserting the parameters of both enhancement cavities yields an expected improvement in XUV power of $5 \cdot 10^6$ and thus 50 μ W of average power in the 13th harmonic.

5.3 Above-threshold ionization

When a laser beam of high intensity interacts with a gaseous medium ionization can occur. If the laser intensity is increased even further, the atoms absorb more photons than necessary to overcome the ionization potential. This process is called *above-threshold-ionization* (ATI) and was discovered in 1979 [180]. For a review see ref. [181]. The resulting photoelectron kinetic energy spectra consist of a series of peaks separated by the photon energy. In general, the peak heights decrease with increasing order. However, a plateau behavior with a pronounced cut-off can be observed. This is similar to the shape of spectra from high-order harmonic generation, which indicates that the two processes are strongly connected.

At high laser intensities, ATI can be understood in terms of quasistatic field ionization and subsequent classical evolution of the electron in the laser field [161]. Directly emitted photoelectrons are accelerated up to a maximum kinetic energy of $E = 2 U_p$, where U_p is the ponderomotive potential (see eq. 41). However, a considerable fraction of the photoelectrons generated when atoms or molecules are exposed to intense laser pulses do not escape directly. Instead they return to the ion core within times of typically less than an optical cycle and in precise synchronization with the electric field of the laser pulse. The underlying mechanism is elastic scattering of the electrons when they return to the ion with subsequent acceleration by the laser field. The rescattered electrons manifest themselves in the high-energy plateau-like annex in the kinetic energy spectrum with a maximum drift energy of $E = 10.007 U_p$ [182].

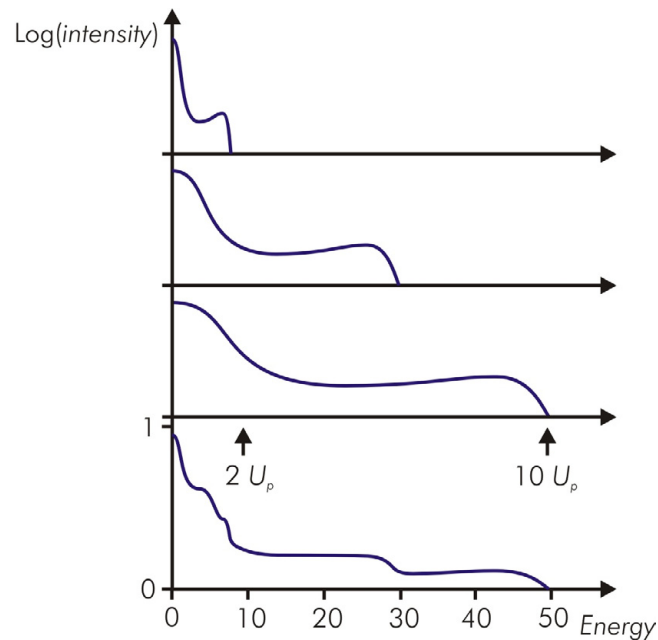


Figure 77. Individual contributions of the half-cycles to the ATI photoelectron spectrum. The upper three panels show qualitatively the spectra generated by the three strongest half-cycles in a phase-stabilized pulse with CE phase $\varphi = 0^\circ$, a ‘cosine pulse’. The cut-off energies were calculated for a pulse of 7 fs duration with a $1 \cdot 10^{14} \text{ W/cm}^2$ intensity on-target. The spectrum for each half-cycle does not consist of a plateau and cut-off as expected in ATI emission but of two peaks with cut-offs at $2 U_p$ and $10 U_p$, respectively. Only half-cycles before the pulse envelope peak were taken into account due to the strong ionization of the gas at the pulse maximum. Also only emission in one direction of polarization is considered ($\theta = 90^\circ$). The bottom panel is the complete spectrum, i.e. the sum of the upper panels. The dips from the half-cycle emission are clearly visible.

The kinetic energy spectrum of the plateau electrons is sensitive to the CE phase for several reasons. First of all, high-energy electrons returning to the ion core can be created only in sub-femtosecond time intervals at the peaks of the electric field of the laser pulse [183] (analogous to high harmonic generation, see fig. 69). However, the probability for them to tunnel through the atomic potential at t_0 depends exponentially on the electric field strength $E(t_0)$. For few-cycle pulses this is likely only for the very few optical half-cycles close to the pulse center. Generally, the highest kinetic energies are reached for electrons returning to the core when the electric field becomes nearly zero, $E(t_1) = 0$. Additionally, the field amplitude E_0 needs to be as high as possible for $t > t_1$ in order to allow effective acceleration after rescattering. Quantum mechanical calculations are in very good qualitative agreement with this classical treatment [184] while considerably softening the sharp cut-off energy limits.

Therefore, the number and energy of the rescattered photoelectrons depends strongly on the evolution of the electric field. In particular, the highest kinetic energy that the electrons can acquire, the cut-off energy, was found to vary with the CE phase [185]. From the asymmetry in cut-off energies in the two principal directions of emission (for a linearly polarized pulse), the value of the CE phase can be inferred [22].

However, not only the cut-off energy changes with CE phase, but also the shape of the spectrum varies. This is due to the fact that in a few-cycle laser pulse, each half-cycle produces a spectrum with a cut-off dependent on the amplitude of its electric field maximum. The energy of the cut-off electrons (in eV) is thus approximated by $E_{HCO} = 10.007 \frac{e^2}{4\omega^2 m_e} E^2 = 1.24 \cdot 10^{-19} \lambda^2 E^2$, where λ is the laser wavelength in μm and E the electric field strength at the maximum of the half-cycle in V/m. Each of the individual half-cycles contributes to the ATI spectrum and the cut-off position, as shown in figure 77. Analyzing this phase-dependent spectrum can thus provide a measure of the actual CE phase of the laser pulse. The analogous effect has recently been observed in high-order harmonic emission [186]. Three distinct contributions from half-cycles were observed in the experimental spectra from which the actual value of the CE phase was extracted by comparison with a library of theoretical energies. In contrast, half-cycle cut-off signatures have not been reported from ATI spectra so far. Substructures in ATI electron spectra were predicted recently [187], though, only the low-energy part of the spectrum was examined and the sub-peaks were not depending on the value of the CE phase.

In the experiment, ATI electrons may simply be generated by focusing an intense ultrashort laser beam into a gas jet. Here, phase-stabilized linearly polarized pulses from the amplifier system described in chapter 3 were employed to generate intensities in the focus of around $1 \cdot 10^{14} \text{ W/cm}^2$. The target consisted of a pulsed nozzle backed by argon gas. The kinetic energy of the photoelectrons can be measured by a time-of-flight detector. In order to resolve not only the energy and the number of the produced electrons but also their direction of emission, the *velocity-map imaging* technique can be employed [188].

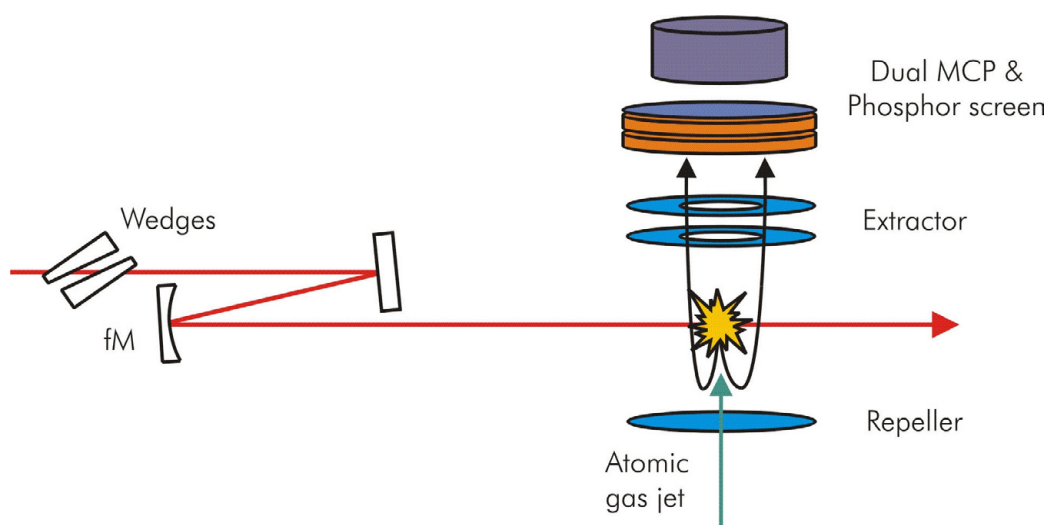


Figure 78. Experimental scheme of the velocity-map imaging setup. Intense few-cycle pulses from the chirped-pulse amplifier system ($E_p = 300$ mJ, $f_{rep} = 3$ kHz, $\lambda_c = 760$ nm, $\tau = 7$ fs, $I_{peak} = 1 \cdot 10^{14}$ W/cm²) are focused in a jet of argon. Electron optics (repeller and extractor) direct the generated electrons to a detector consisting of a dual multichannel plate (MCP) and a phosphorous screen (F2226-24PX, Hamamatsu Inc.). The gas jet was operated at 50 Hz and the MCP was switched such that electrons from every 60th laser pulse were detected. This allowed maintaining a low background pressure in the chamber (typically $2 \cdot 10^{-7}$ mbar) and keeping ionization from background gases sufficiently low. The image of the phosphor screen was taken by a CCD camera (TM-9701, JAI PULNiX Inc.). The CE phase of the laser beam may be adjusted with a pair of thin wedges. fM: spherical focusing mirror, focal length 40 cm.

Figure 78 shows the schematics of the detection principle. The electrons generated at the crossing point of the laser beam with the gas jet are accelerated and focused by electron optics onto a multichannel plate-phosphor screen assembly. A CCD camera records the image of the screen. A sample image is shown in figure 79. In this manner, the direction of emission is mapped onto the angle and the electron kinetic energy onto the radius at the detector (using a polar coordinate system). Thus, the velocity-map imaging technique enables the observation of photoelectron emission in both polarization directions. This is not possible with the standard time-of-flight measurement method.

Different information may be extracted from these images. Integrating a pie section of the image over a certain angle about an axis (usually the axis of the laser polarization) reveals a spectrum for the upper ($P_{up}(E, \varphi)$) and lower ($P_{down}(E, \varphi)$) half of the image, respectively.

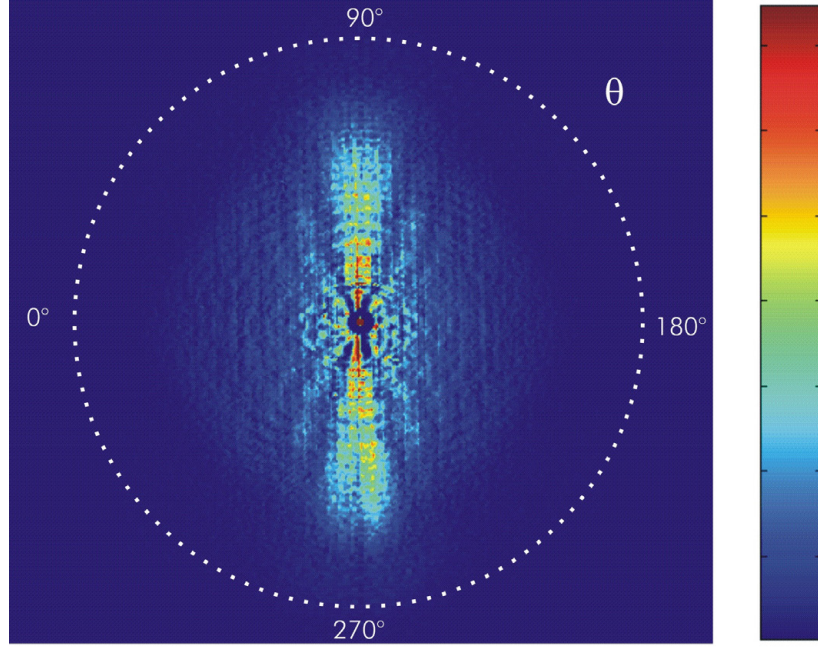


Figure 79. Sample image from the velocity-map imaging detector. The laser pulses were phase-stabilized ($\varphi = 0^\circ$) and propagated along the horizontal axis ($\theta = 0^\circ/180^\circ$) with linear polarization in the vertical axis ($\theta = 90^\circ/270^\circ$).

From both spectra, the asymmetry factor can be calculated

$$A(E, \varphi) = \frac{P_{up}(E, \varphi) - P_{down}(E, \varphi)}{P_{up}(E, \varphi) + P_{down}(E, \varphi)} \quad \text{Eq. 45}$$

with

$$P_{up/down}(E, \varphi) = \int d\theta \int_0^{360} d\psi P(E, \theta, \psi, \varphi) \sin \theta \quad \text{Eq. 46}$$

with ψ being the azimuthal angle and where the integration limits over the polar angle θ are given by the pie section of interest.

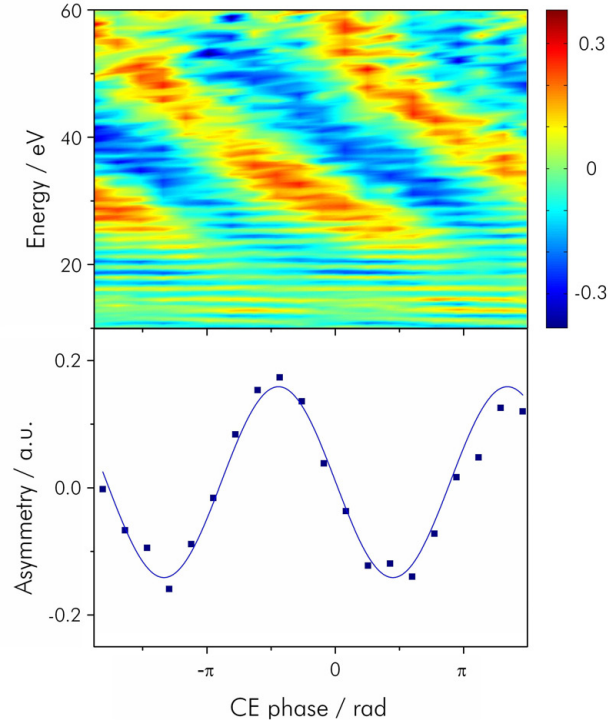


Figure 80. Map of the asymmetry factor integrated over 10° polar half-angle about the laser axis. The map consists of 20 spectra. The step in CE phase between images is $\pi/5$. The integration time for each CE phase setting was 1 min. The bottom panel shows the asymmetry integrated over the energy range 30 to 40 eV versus the CE phase.

A map of the asymmetry factor as a function of kinetic electron energy and CE phase derived from measured angular-resolved ATI spectra is shown in figure 80. The polar angle was integrated over $2 \cdot 10^\circ$ about the laser polarization axis which provided the strongest overall asymmetry. Figure 80 also displays the asymmetry factor integrated over the energy range 30 to 40 eV, the region where the strongest oscillation in asymmetry is found. CE phase dependence, though with smaller modulation depth, is also seen in the other energy ranges above and below.

However, as mentioned above, not only the asymmetry between spectra but also the individual spectra themselves reveal a CE phase dependence. Figure 81 illustrates the change in the spectral shape when the CE phase is varied from 0 to π in steps of $\pi/5$. The individual cut-offs from half-cycles appear as spectral peaks that move in energy as a function of the CE phase. At least two half-cycle cut-offs are visible in each spectrum. In contrast, the spectrum recorded with randomly varying CE phase does not display signs of half-cycle cut-offs. The position in energy of the cut-offs is in good agreement with estimates from the relative peak heights of half-cycles of a laser pulse with 7 fs duration (FWHM) in a Gaussian temporal profile and a peak intensity on-target of $1 \cdot 10^{14}$ W/cm².

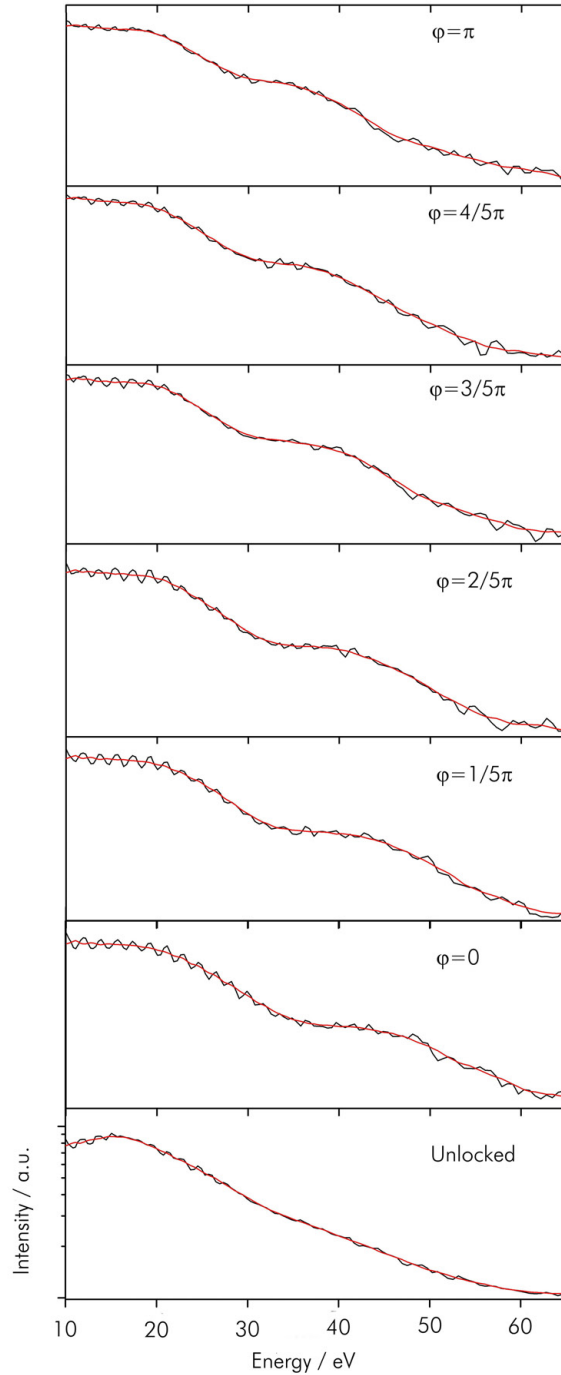


Figure 81. Half-cycle cut-offs in ATI spectra. Spectra of ATI photoelectrons emitted in one hemisphere, spatially integrated over 10° half-angle about the laser polarization axis ($\theta = 90^\circ/180^\circ$). Smoothed line-outs (red lines) emphasize the half-cycle cut-offs. The upper five panels show spectra with phase-stabilized 7 fs pulses with the CE phase varying in steps of $\pi/5$. Bottom panel displays the spectrum generated with unlocked CE phase.

The evolution of the half-cycle cut-offs is even clearer visualized when the spectra are stacked to give a color-mapped plot. Figure 82 shows the experimental ATI spectra recorded as the CE phase is varied in a range of almost 4π . Individual contributions of two half-cycles can be observed, which are – by comparison to (classical) theoretical estimates – attributed to the half-cycles with the highest amplitude and the half-cycle before in the same direction. The blue dots represent theoretical estimates of the individual cut-offs of these half-cycles for a laser pulse with parameters as above. Contributions from the half-cycle after the peak maximum are not clearly observed in the experimental data. These contributions were also not seen in the half-cycle cut-offs in high-harmonic spectra in ref. [186]. Potentially, ionization saturation could be responsible for such a behavior.

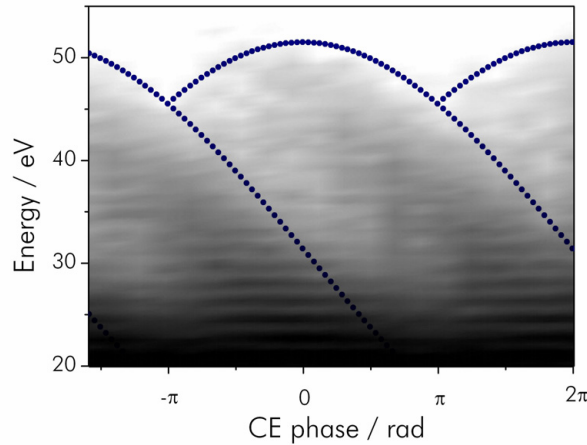


Figure 82. Theoretical and experimental positions of half-cycle cut-offs versus CE phase. The color-mapped plot consists of 20 spatially-integrated spectra (10° half-angle) measured for different settings of the CE phase. The step in CE phase between images is $\pi/5$ with an integration time for each CE phase setting of 1 min. The theoretical half-cycle cut-off positions (blue dots) were calculated from the relative intensity at the maxima of the two strongest half-cycles of a 7 fs pulse with Gaussian temporal profile and a peak intensity of $1 \cdot 10^{14} \text{ W/cm}^2$. Only half-cycles before the global pulse peak were taken into account due to the strong ionization of the gas at the pulse maximum.

By comparison between the theoretical estimates and the experimental data, the actual value of the CE phase can be determined from figure 82, similarly to the CE phase recovery procedure proposed in ref. [186]. Both the asymmetry in the electron emission from ATI and the position of individual half-cycle cut-offs in the electron kinetic energy spectra can serve to derive the CE phase. Velocity-map imaging provides electron kinetic energy spectra in both emission directions along the laser polarization axis such that both ways of CE phase determination are accessible single-shot. This is also possible with a setup employing two time-of-flight detectors

(so-called stereo-ATI setup, ref. [185]). In contrast to that, half-cycle cut-offs may serve in the future to determine the phase directly in a measurement with only a single time-of-flight detector.

5.4 Conclusions

High-harmonic generation is a highly nonlinear frequency conversion process that permits the generation of coherent XUV light. HHG either makes use of the nonlinear interaction of moderate laser intensities with a gas target or of relativistic intensities with solid surfaces. However, the actual generation process differs. Combining both worlds by using the generation process customarily employed in a gas target (fig. 70) and applying it to a solid surface was proposed recently. The results from a fused silica sample under grazing incidence showed harmonics up to 11th order, albeit at very low efficiencies. Changes in the focusing geometry and possibly a different target material (with a lattice structure) could increase the generated power.

Also, placing the interaction gas target in an enhancement resonator for femtosecond pulses holds the potential of improved overall conversion efficiency. Light that has not contributed to the conversion is stored in the resonator and can participate in a later pass through the nonlinear medium. In a first demonstration harmonics up to 15th order were demonstrated with overall efficiencies comparable to chirped-pulse amplifier systems. The envisaged build-up resonators seeded by high-power Yb-based oscillator-amplifier systems [189-191] will likely push the cut-off energy to shorter wavelengths. Here the scaling law $E_{cutoff} \sim I \lambda^2$ (eq. 43) helps: the longer wavelength of ytterbium, around 1030 nm, by itself results in an increase in the cut-off energy of 65%. Clearly also the higher average power of these systems holds the promise of shifting the cut-off energy as well as generating a larger number of photons in a given harmonic order.

Apart from HHG, other strong-field phenomenon exist that can be studied with intense few-cycle laser pulses. Above-threshold ionization is one of the processes that display a pronounced dependence on the CE phase of the driving laser pulses. The ionization of argon atoms is studied with the velocity-map imaging technique that can spatially resolve the generated photoelectrons. Apart from the well-known phase-dependent asymmetry of the ATI spectra in the two polarization directions, another CE phase effect was described: signatures of the half-cycles of the electric field in a phase-stabilized few-cycle laser pulse were observed in the ATI spectra. Comparing the individual contributions of these half-cycles with theoretical estimates reveals the value of the CE phase. With better resolving power, spatial filtering and thus improved contrast, the information from the half-cycle cut-offs in an ATI spectrum could potentially be used to determine the CE phase with a single time-of-flight detector.

“I look back on tremendous efforts and exhaustion and dismal looking out of a tent door on to a dismal world of snow and vanishing hopes and yet, and yet, and yet there have been a good many things to see the other side.”

G. L. Mallory

Chapter 6

Outlook

Ultrafast laser science has progressed rapidly in the last years. Since the invention of chirped mirrors in 1994 pulse durations from laser oscillators have decreased continuously, reaching the single-cycle limit very recently. Similarly, the quest for ever higher pulse energies was spurred by the demonstration of chirped-pulse amplification in 1985. Recent developments attempt to close the gap in terms of pulse energy and repetition rate between laser oscillator and complex CPA systems by alternative methods. The alternative concepts discussed in this work are long-cavity oscillators, also supplemented by a cw post-amplifier, and most importantly enhancement cavities. Figure 83 shows an overview of the characteristics of the presented ultrafast laser sources.

The chirped-pulse oscillator in combination with a compact double-pass post-amplifier is expected to produce microjoule pulses at repetition rates of a few megahertz. Tightly focusing these pulses will result in intensities well above $1 \cdot 10^{14}$ W/cm², sufficient for the generation of XUV photons by HHG. First ionization experiments with a helium gas jet indicate that these intensities are attainable directly from a chirped-pulse oscillator [112]. These developments could lead to a compact coherent XUV source at megahertz repetition rate.

The enhancement cavity operating at 10 MHz, seeded by a long-cavity oscillator was presented in detail. It is aimed at producing XUV radiation by HHG with a comb structure usable for spectroscopic experiments. In particular, the system will be employed for probing the 1S-2S transition of He⁺. This two-photon transition is located at 60 nm, corresponding to the 13th harmonic. Inferring from the proof-of-principle experiment with the 100 MHz enhancement cavity, 50 μW of average power in the 13th harmonic can be expected at 10 MHz repetition rate. In addition to the out-coupler, steering and focusing mirrors for the XUV light will reduce the power by a large amount, as optics with high reflectivity are not available in this wavelength range. If ~20% of the power can reach the helium ions in the trap in an anti-collinear arrangement with a focus spot size of 1 μm, an event rate in the hertz-range can be expected. With an acquisition time of 10⁵, this corresponds to a measurement on the $2 \cdot 10^{14}$ level [192].

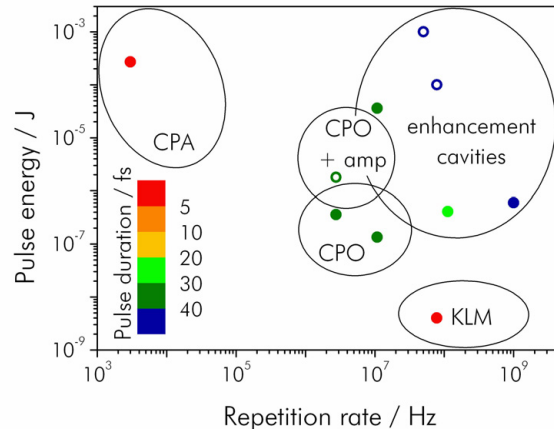


Figure 83. Overview of the ultrafast laser sources discussed in this work. The range of the technologies in the parameter space of pulse energy and repetition rate is marked by ovals. Solid dots represent realized systems, while empty dots denote parameters of projected systems. CPA: chirped-pulse amplifiers; CPO: chirped-pulse long-cavity oscillators; CPO+amp: CPO with subsequent cw amplification; KLM: Kerr-lens mode-locked oscillators. The two projected enhancement cavities will be seeded by ytterbium amplifier systems (fiber amplifier and slab amplifier, respectively).

Further in the future, enhancement cavities could be employed for coincidence experiments, e.g. for the investigation of the correlation of electrons in multiphoton double ionization [193]. The simultaneous detection of the electrons emitted from a single atom necessitates an event rate per laser pulse much smaller than one (typically on the order of 0.05 per laser shot). This in turn means that such an experiment would benefit immensely from an increase in repetition rate. The use of an enhancement cavity instead of a CPA system would reduce acquisition times by up to five orders of magnitude.

Both these experiments would profit greatly from an increase in the average circulating power in the cavity. One thrust of research toward this goal is the seeding of the enhancement resonator with master oscillator-power amplifier systems. Increasing the incident pulse energy can boost the circulating power if the seed power is efficiently coupled to the cavity. The cw-pumped double-pass Ti:sapphire post-amplifier is a promising device for boosting the pulse energy before seeding the enhancement cavity. But especially amplifier concepts based on ytterbium as the gain material hold high potential in that respect. Mainly two architectures are available, fiber-based amplifiers and slab amplifiers. The former can consist of a bulk Yb:KGW oscillator and subsequent chirped-pulse amplification in an Yb-doped fiber. It provides pulses at a center wavelength of 1030 nm with an energy of up to 1 μ J and a duration of 45 fs after compression by a set of chirped mirrors [190, 191]. The latter has so far only been demonstrated for Nd:YAG doped crystals [189]. With the larger bandwidth of

Yb:YAG such a system is expected to deliver ~100 fs pulses with a few tens of microjoule energy at a repetition rate of 50 MHz.

Enhancing the pulses from such an amplifier system in a passive resonator, may be by a factor of 100, will together with intra-cavity HHG tap a range of new applications: the envisaged coherent XUV light at 13 nm wavelength with average power close to a milliwatt could be used for instance in the realm of XUV lithography for the characterization of masks or the inspection of the surface of wafers.

Appendix

Appendix A.1

The electric field of a train of pulses is given by

$$E(t) = \sum_n \hat{E}(t - n\tau) \cdot \exp(i(\omega_c t - n\omega_c \tau + n\Delta\varphi + \varphi_0)), \quad \text{Eq. 47}$$

where $\hat{E}(t)$ is the envelope function for a single pulse, τ the time between pulses, ω_c the center frequency, φ the pulse-to-pulse CE phase shift and φ_0 a phase offset. The Fourier transform yields

$$\begin{aligned} E(\omega) &= \int E(t) \cdot e^{-i\omega t} dt = \\ &= \sum_n \exp(i(-n\omega_c \tau + n\Delta\varphi + \varphi_0)) \cdot \int \hat{E}(t - n\tau) \cdot \exp(i(\omega_c - \omega)t) dt \end{aligned} \quad \text{Eq. 48}$$

By substituting variables and letting

$$\tilde{E}(\omega) = \int \hat{E}(t) e^{-i\omega t} dt, \quad \text{Eq. 49}$$

one obtains

$$E(\omega) = e^{i\varphi_0} \tilde{E}(\omega - \omega_c) \sum_n \exp(-in\omega\tau + in\Delta\varphi). \quad \text{Eq. 50}$$

Using the Poisson sum formula along with the fact that the Fourier transform of a constant is the delta function $\delta(t)$ yields

$$E(\omega) = e^{i\varphi_0} \tilde{E}(\omega - \omega_c) 2\pi \sum_n \delta(-\omega\tau + \Delta\varphi - 2\pi n), \quad \text{Eq. 51}$$

which is a spectrum with discrete lines at frequencies

$$\omega_n = \frac{2\pi n}{\tau} - \frac{\Delta\varphi}{\tau} \quad \text{or} \quad f_n = n f_{rep} + f_{CEO} \quad \text{Eq. 52}$$

for

$$f_{CEO} = (-) \frac{\Delta\phi f_{rep}}{2\pi}. \quad \text{Eq. 53}$$

Appendix A.2

The frequencies of the longitudinal modes that are resonant in a Fabry-Perot laser cavity obey

$$\omega_m = \frac{2\pi c}{n(\omega)L}, \quad \text{Eq. 54}$$

where $n(\omega)$ is the index of refraction averaged over the resonator and L the cavity length. In general n depends on ω , i.e. dispersion is present. However, in a mode-locked laser cavity effectively the dispersion vanishes due to compensation effects from nonlinearities. Neglecting dispersion of higher than second order, this implies for the wavevector $k(\omega)$

$$\frac{\partial k}{\partial \omega} = \frac{1}{v_g} = \text{const} \quad \text{and} \quad \frac{\partial^m k}{\partial \omega^m} = 0 \quad \text{for } m > 1, \quad \text{Eq. 55}$$

where v_g is the averaged group velocity in the cavity. Therefore $k(\omega)$ takes the form $k(\omega) = k_0 + \omega/v_g$. Combined with the general dispersion equation ($k = \omega n/c$) this yields

$$n(\omega) = c \left(\frac{1}{v_g} + \frac{k_0}{\omega} \right), \quad \text{Eq. 56}$$

which does in fact depend on ω . Inserting this into eq. 54 one obtains

$$\omega_m = \frac{2\pi v_g}{L} m - k_0 v_g. \quad \text{Eq. 57}$$

As $v_g/L = f_{rep}$, the spacing of the comb lines is again the repetition frequency. The condition for the phase velocity v_p , $\omega/k(\omega) = v_p$, requires

$$k_0 = \omega \left(\frac{1}{v_p} - \frac{1}{v_g} \right). \quad \text{Eq. 58}$$

Inserting eq. 58 into eq. 57, converting from angular frequencies and using $f_m = m f_{rep} + f_{CEO}$ yields

$$f_{CEO} = \frac{\omega_c v_g}{2\pi} \left(\frac{1}{v_g} - \frac{1}{v_p} \right). \quad \text{Eq. 59}$$

Bibliography

1. T. Fuji, J. Rauschenberger, A. Apolonski, V. S. Yakovlev, G. Tempea *et al.* Monolithic carrier-envelope phase-stabilization scheme. *Opt. Lett.* **30**, 332-334 (2005).
2. T. Fuji, J. Rauschenberger, C. Gohle, A. Apolonski, T. Udem *et al.* Attosecond control of optical waveforms. *New J. Phys.* **7**, 116 (2005).
3. J. Rauschenberger, T. Fuji, M. Hentschel, A.-J. Verhoef, T. Udem *et al.* Carrier-envelope phase-stabilized amplifier system. *Laser Phys. Lett.* **3**, 37-42 (2006).
4. C. Gohle, J. Rauschenberger, T. Fuji, T. Udem, A. Apolonski *et al.* Carrier envelope phase noise in stabilized amplifier systems. *Opt. Lett.* **30**, 2487-2489 (2005).
5. M. F. Kling, C. Siedschlag, A.-J. Verhoef, J. I. Khan, M. Schultze *et al.* Control of Electron Localization in Molecular Dissociation. *Science* **312**, 246-248 (2006).
6. M. Uiberacker, T. Uphues, M. Schultze, A.-J. Verhoef, V. S. Yakovlev *et al.* Attosecond real-time observation of electron tunnelling in atoms. *Nature* **446**, 627-632 (2007).
7. C. Gohle, T. Udem, M. Herrmann, J. Rauschenberger, R. Holzwarth *et al.* A frequency comb in the extreme ultraviolet. *Nature* **436**, 234-237 (2005).
8. A. Zewail. Femtochemistry: Atomic-Scale Dynamics of the Chemical bond using ultrafast lasers - (Nobel lecture). *Angew. Chem. - Int. Ed.* **39**, 2587-2631 (2000).
9. M. Drescher, M. Hentschel, R. Kienberger, G. Tempea, C. Spielmann *et al.* X-ray Pulses Approaching the Attosecond Frontier. *Science* **291**, 1923-1927 (2001).
10. R. Kienberger, M. Uiberacker, E. Goulielmakis, A. Baltuška, M. Drescher *et al.* Single sub-fs soft-X-ray pulses: generation and measurement with the atomic transient recorder. *J. Mod. Opt.* **52**, 261-275 (2005).
11. A. Baltuška, T. Udem, M. Uiberacker, M. Hentschel, E. Goulielmakis *et al.* Attosecond control of electronic processes by intense light fields. *Nature* **421**, 611-615 (2003).
12. J. Reichert, M. Niering, R. Holzwarth, M. Weitz, T. Udem *et al.* Phase Coherent Vacuum-Ultraviolet to Radio Frequency Comparison with a Mode-Locked Laser. *Phys. Rev. Lett.* **84**, 3232-3235 (2000).
13. D. J. Jones, S. A. Diddams, J. K. Ranka, A. Stentz, R. S. Windeler *et al.* Carrier-Envelope Phase Control of Femtosecond Mode-Locked Lasers and Direct Optical Frequency Synthesis. *Science* **288**, 635-639 (2000).
14. A. Baltuška, M. Uiberacker, E. Goulielmakis, R. Kienberger, V. S. Yakovlev *et al.* Phase-controlled amplification of few-cycle laser pulses. *IEEE J. Sel. Top. Quantum Electron.* **9**, 972-989 (2003).
15. R. Kienberger, E. Goulielmakis, M. Uiberacker, A. Baltuška, V. S. Yakovlev *et al.* Atomic transient recorder. *Nature* **427**, 817-821 (2004).
16. G. Sansone, E. Benedetti, F. Calegari, C. Vozzi, L. Avaldi *et al.* Isolated Single-Cycle Attosecond Pulses. *Science* **314**, 443-446 (2006).

17. S. Adachi, T. Kobayashi. Carrier-Envelope Phase-Controlled Quantum Interference in Optical Poling. *Phys. Rev. Lett.* **94**, 153903 (2005).
18. Y. S. Lee, J. Sung, C. Nam, T. Yu, K.-H. Hong. Novel method for carrier-envelope-phase stabilization of femtosecond laser pulses. *Opt. Express* **13**, 2969-2976 (2005).
19. A. Apolonski, P. Dombi, G. G. Paulus, M. Kakehata, R. Holzwarth *et al.* Observation of Light-Phase-Sensitive Photoemission from a Metal. *Phys. Rev. Lett.* **92**, 073902 (2004).
20. T. M. Fortier, P. A. Roos, D. J. Jones, S. T. Cundiff, R. D. R. Bhat *et al.* Carrier-Envelope Phase-Controlled Quantum Interference of Injected Photocurrents in Semiconductors. *Phys. Rev. Lett.* **92**, 147403 (2004).
21. M. Kakehata, H. Takada, Y. Kobayashi, K. Torizuka. Carrier-envelope-phase stabilized chirped-pulse amplification system scalable to higher pulse energies. *Opt. Express* **12**, 2070-2080 (2004).
22. M. G. Schätzel, F. Lindner, G. G. Paulus, H. Walther, E. Goulielmakis *et al.* Long-term stabilization of the carrier-envelope phase of few-cycle laser pulses. *Appl. Phys. B* **79**, 1021-1025 (2004).
23. A.-J. Verhoef, A. Fernández, M. Lezius, K. O'Keeffe, M. Uiberacker *et al.* Few-cycle carrier envelope phase-dependent stereo detection of electrons. *Opt. Lett.* **31**, 3520-3522 (2006).
24. A. L. Cavalieri, N. Müller, T. Uphues, V. S. Yakovlev, R. Kienberger *et al.* Attosecond time-resolved photoemission from solids. *in preparation* (2007).
25. B. Piraux, J. Bauer, S. Laulan, H. Bachau. Probing electron-electron correlation with attosecond pulses. *Eur. Phys. J. D* **26**, 7-13 (2003).
26. T. W. Hänsch. Einstein Lecture - Passion for precision. *Ann. Phys.* **15**, 627-652 (2006).
27. J. L. Hall. Nobel Lecture: Defining and measuring optical frequencies. *Rev. Mod. Phys.* **78**, 1279-1295 (2006).
28. V. A. Dzuba, V. V. Flambaum, J. K. Webb. Space-Time Variation of Physical Constants and Relativistic Corrections in Atoms. *Phys. Rev. Lett.* **82**, 888-891 (1999).
29. M. Fischer, N. Kolachevsky, M. Zimmermann, R. Holzwarth, T. Udem *et al.* New limits on the drift of fundamental constants from laboratory measurements. *Phys. Rev. Lett.* **92**, 230802 (2004).
30. T. M. Fortier, N. Ashby, J. C. Bergquist, M. J. Delaney, S. A. Diddams *et al.* Precision atomic spectroscopy for improved limits on variation of the fine structure constant and local position invariance. *Phys. Rev. Lett.* **98**, 070801 (2007).
31. M. Niering, R. Holzwarth, J. Reichert, P. Pokasov, T. Udem *et al.* Measurement of the Hydrogen 1S-2S Transition Frequency by Phase Coherent Comparison with a Microwave Cesium Fountain Clock. *Phys. Rev. Lett.* **84**, 5496-5499 (2000).
32. T. W. Hänsch, *The Hydrogen Atom*. G. F. Bassani, M. Inguscio, T. W. Hänsch, Eds. (Springer Verlag, New York, 1989).
33. L. Xu, C. Spielmann, A. Poppe, T. Brabec, F. Krausz *et al.* Route to phase control of ultrashort pulses. *Opt. Lett.* **21**, 2008-2010 (1996).

-
34. J. Rauschenberger, T. M. Fortier, D. J. Jones, J. Ye, S. T. Cundiff. Control of the frequency comb from a modelocked Erbium-doped fiber laser. *Opt. Express* **10**, 1404-1410 (2002).
 35. I. Hartl, G. Imeshev, M. E. Fermann, C. Langrock, M. M. Fejer. Integrated self-referenced frequency-comb laser based on a combination of fiber and waveguide technology. *Opt. Express* **13**, 6490-6496 (2005).
 36. B. R. Washburn, S. A. Diddams, N. R. Newbury, J. W. Nicholson, M. F. Yan *et al.* Phase-locked, erbium-fiber-laser-based frequency comb in the near infrared. *Opt. Lett.* **29**, 250-253 (2004).
 37. R. J. Jones, K. D. Moll, M. J. Thorpe, J. Ye. Phase-Coherent Frequency Combs in the Vacuum Ultraviolet via High-Harmonic Generation inside a Femtosecond Enhancement Cavity. *Phys. Rev. Lett.* **94**, 193201 (2005).
 38. R. Zerne, C. Altucci, M. B. Gaarde, A. L'Huillier, C. Lynga *et al.* Phase-Locked High-Order Harmonic Sources. *Phys. Rev. Lett.* **79**, 1006-1009 (1997).
 39. M. Kovacev, S. V. Fomichev, E. Priori, Y. Mairesse, H. Merdji *et al.* Extreme Ultraviolet Fourier-Transform Spectroscopy with High Order Harmonics. *Phys. Rev. Lett.* **95**, 223903 (2005).
 40. T. H. Maiman. Stimulated Optical Radiation in Ruby. *Nature* **187**, 493-493 (1960).
 41. A. J. De Maria, D. A. Stetser, H. Heynau. Self mode-locking of lasers with saturable absorbers. *Appl. Phys. Lett.* **8**, 174-176 (1966).
 42. G. Steinmeyer, D. H. Sutter, L. Gallmann, N. Matuschek, U. Keller. Frontiers in Ultrashort Pulse Generation: Pushing the Limits in Linear and Nonlinear Optics. *Science* **286**, 1507-1512 (1999).
 43. U. Keller. Recent developments in compact ultrafast lasers. *Nature* **424**, 831-838 (2003).
 44. R. L. Fork, C. H. B. Cruz, P. C. Becker, C. V. Shank. Compression of optical pulses to six femtoseconds by using cubic phase compensation. *Opt. Lett.* **12**, 483-485 (1987).
 45. R. Ell, U. Morgner, F. X. Kärtner, J. G. Fujimoto, E. P. Ippen *et al.* Generation of 5-fs pulses and octave-spanning spectra directly from a Ti:sapphire laser. *Opt. Lett.* **26**, 373-375 (2001).
 46. D. H. Sutter, G. Steinmeyer, L. Gallmann, N. Matuschek, F. Morier-Genoud *et al.* Semiconductor saturable-absorber mirror-assisted Kerr-lens mode-locked Ti:sapphire laser producing pulses in the two-cycle regime. *Opt. Lett.* **24**, 631-633 (1999).
 47. B. Schenkel, J. Biegert, U. Keller, C. Vozzi, M. Nisoli *et al.* Generation of 3.8-fs pulses from adaptive compression of a cascaded hollow fiber supercontinuum. *Opt. Lett.* **28**, 1987-1989 (2003).
 48. M. Yamashita, K. Yamane, R. Morita. Quasi-automatic phase-control technique for chirp compensation of pulses with over-one-octave bandwidth-generation of few- to mono-cycle optical pulses. *IEEE J. Sel. Top. Quantum Electron.* **12**, 213-222 (2006).
 49. F. J. McClung, R. W. Hellwarth. Giant optical pulsations from ruby. *J. Appl. Phys.* **33**, 828-829 (1962).

50. U. Keller, K. J. Weingarten, F. X. Kärtner, D. Kopf, B. Braun *et al.* Semiconductor saturable absorber mirrors (SESAM's) for femtosecond to nanosecond pulse generation in solid-state lasers. *IEEE J. Sel. Top. Quantum Electron.* **2**, 435-453 (1996).
51. D. E. Spence, P. N. Kean, W. Sibbett. 60-fsec pulse generation from a self-mode-locked Ti:sapphire laser. *Opt. Lett.* **16**, 42-44 (1991).
52. F. Salin, J. Squier, M. Piché. Modelocking of Ti:Sapphire lasers and self-focusing: a Gaussian approximation. *Opt. Lett.* **16**, 1674-1676 (1991).
53. D. X. Hammer, R. J. Thomas, G. D. Noojin, B. A. Rockwell, P. K. Kennedy *et al.* Experimental investigation of ultrashort pulse laser induced breakdown thresholds in aqueous media. *IEEE J. Quantum Electron.* **32**, 670-678 (1996).
54. K. Koenig, O. Krauss, I. Riemann. Intratissue surgery with 80 MHz nanojoule femtosecond laser pulses in the near infrared. *Opt. Express* **10**, 171-176 (2002).
55. F. H. Loesel, M. H. Niemz, J. F. Bille, T. Juhasz. Laser-induced optical breakdown on hard and soft tissues and its dependence on the pulse duration: experiment and model. *IEEE J. Quantum Electron.* **32**, 1717-1722 (1996).
56. R. Osellame, N. Chiodo, G. D. Valle, S. Taccheo, R. Ramponi *et al.* Optical waveguide writing with a diode-pumped femtosecond oscillator. *Opt. Lett.* **29**, 1900-1902 (2004).
57. A. M. Kowalevich, V. Sharma, E. P. Ippen, J. G. Fujimoto, K. Minoshima. Three-dimensional photonic devices fabricated in glass by use of a femtosecond laser oscillator. *Opt. Lett.* **30**, 1060-1062 (2005).
58. D. Huang, E. A. Swanson, C. P. Lin, J. S. Schuman, W. G. Stinson *et al.* Optical Coherence Tomography. *Science* **254**, 1178-1181 (1991).
59. A. Stingl, M. Lenzner, C. Spielmann, F. Krausz, R. Szipöcs. Sub-10-fs mirror-dispersion-controlled Ti:sapphire laser. *Opt. Lett.* **20**, 602-604 (1995).
60. H. Kogelnik. Review of dye lasers. *J. Opt. Soc. Am.* **61**, 1561- (1971).
61. Y. Chen, F. X. Kärtner, U. Morgner, S. H. Cho, H. A. Haus *et al.* Dispersion-managed mode locking. *J. Opt. Soc. Am. B* **16**, 1999-2004 (1999).
62. R. L. Fork, O. E. Martinez, J. P. Gordon. Negative dispersion using pairs of prisms. *Opt. Lett.* **9**, 150-152 (1984).
63. U. Morgner, R. Ell, G. Metzler, T. R. Schibli, F. X. Kärtner *et al.* Nonlinear Optics with Phase-Controlled Pulses in the Sub-Two-Cycle Regime. *Phys. Rev. Lett.* **86**, 5462-5465 (2001).
64. A. Bartels, H. Kurz. Generation of a broadband continuum by a Ti:sapphire femtosecond oscillator with a 1-GHz repetition rate. *Opt. Lett.* **27**, 1839-1841 (2002).
65. T. M. Fortier, D. J. Jones, S. T. Cundiff. Phase stabilization of an octave-spanning Ti:sapphire laser. *Opt. Lett.* **28**, 2198-2200 (2003).
66. L. Matos, D. Kleppner, O. Kuzucu, T. R. Schibli, J. Kim *et al.* Direct frequency comb generation from an octave-spanning, prismless Ti:sapphire laser. *Opt. Lett.* **29**, 1683-1685 (2004).

-
67. T. Fuji, A. Unterhuber, V. S. Yakovlev, G. Tempea, A. Stingl *et al.* Generation of smooth, ultra-broadband spectra directly from a prism-less Ti:sapphire laser. *Appl. Phys. B* **77**, 125-128 (2003).
 68. C. Iaconis, I. A. Walmsley. Spectral phase interferometry for direct electric-field reconstruction of ultrashort optical pulses. *Opt. Lett.* **23**, 792-794 (1998).
 69. D. Kane, R. Trebino. Characterization of arbitrary femtosecond pulses using frequency-resolved optical gating. *IEEE J. Quantum Electron.* **29**, 571-579 (1993).
 70. S. T. Cundiff, W. H. Knox, E. P. Ippen, H. A. Haus. Frequency-dependent mode size in broadband Kerr-lens mode locking. *Opt. Lett.* **21**, 662-664 (1996).
 71. L. Gallmann, G. Steinmeyer, D. H. Sutter, T. Rupp, C. Iaconis *et al.* Spatially resolved amplitude and phase characterization of femtosecond optical pulses. *Opt. Lett.* **26**, 96-98 (2001).
 72. R. Szipöcs, K. Ferencz, C. Spielmann, F. Krausz. Chirped multilayer coatings for broadband dispersion control in femtosecond lasers. *Opt. Lett.* **19**, 201-203 (1994).
 73. V. Pervak, A. V. Tikhonravov, M. K. Trubetskov, S. Naumov, F. Krausz *et al.* 1.5-octave chirped mirror for pulse compression down to sub-3 fs. *Appl. Phys. B* **87**, 5-12 (2007).
 74. A. P. Kovács, K. Osvay, Z. Bor, R. Szipöcs. Group-delay measurement on laser mirrors by spectrally resolved white-light interferometry. *Opt. Lett.* **20**, 788-790 (1995).
 75. A. Schliesser, C. Gohle, T. Udem, T. W. Hänsch. Complete characterization of a broadband high-finesse cavity using an optical frequency comb. *Opt. Express* **14**, 5975-5983 (2006).
 76. M. J. Thorpe, R. J. Jones, J. Ye, K. D. Moll, R. Lalezari. Precise measurements of optical cavity dispersion and mirror coating properties via femtosecond combs. *Opt. Express* **13**, 882-888 (2005).
 77. I. D. Jung, F. X. Kärtner, N. Matuschek, D. H. Sutter, F. Morier-Genoud *et al.* Self-starting 6.5-fs pulses from a Ti:sapphire laser. *Opt. Lett.* **22**, 1009-1011 (1997).
 78. R. Paschotta, U. Keller. Passive mode locking with slow saturable absorbers. *Appl. Phys. B* **73**, 653-662 (2001).
 79. N. Haverkamp, H. Hundertmark, C. Fallnich, H. R. Telle. Frequency stabilization of mode-locked Erbium fiber lasers using pump power control. *Appl. Phys. B* **78**, 321-324 (2004).
 80. D. R. Walker, T. Udem, C. Gohle, B. Stein, T. W. Hänsch. Frequency dependence of the stable point in a fluctuating frequency comb. *in preparation* (2007).
 81. T. Udem, J. Reichert, R. Holzwarth, T. W. Hänsch. Accurate measurement of large optical frequency differences with a mode-locked laser. *Opt. Lett.* **24**, 881-883 (1999).
 82. K. W. Holman, R. J. Jones, A. Marian, S. T. Cundiff, J. Ye. Intensity-related dynamics of femtosecond frequency combs. *Opt. Lett.* **28**, 851-853 (2003).
 83. R. K. Shelton, L.-S. Ma, H. C. Kapteyn, M. M. Murnane, J. L. Hall *et al.* Phase-Coherent Optical Pulse Synthesis from Separate Femtosecond Lasers. *Science* **293**, 1286-1289 (2001).

84. J. K. Ranka, R. S. Windeler, A. Stentz. Visible continuum generation in air silica microstructure optical fibers with anomalous dispersion at 800nm. *Opt. Lett.* **25**, 25-27 (2000).
85. J. K. Ranka, R. S. Windeler, A. Stentz. Optical properties of high-delta air silica microstructure optical fibers. *Opt. Lett.* **25**, 796-798 (2000).
86. J. Herrmann, U. Griebner, N. Zhavoronkov, A. Husakou, D. Nickel *et al.* Experimental Evidence for Supercontinuum Generation by Fission of Higher-Order Solitons in Photonic Fibers. *Phys. Rev. Lett.* **88**, 173901 (2002).
87. Z. Várallyay, J. Fekete, Á. Bányász, S. Lakó, R. Szipöcs, Sub-nanojoule pulse compression down to 6 fs in photonic crystal fibers, in *Conference on Lasers and Electro-Optics, Technical Digest, paper JThE21*. (Baltimore, MD, USA, 2005).
88. T. M. Ramond, S. A. Diddams, L. Hollberg, A. Bartels. Phase-coherent link from optical to microwave frequencies by means of the broadband continuum from a 1-GHz Ti:sapphire femtosecond oscillator. *Opt. Lett.* **27**, 1842-1844 (2002).
89. J. Reichert, R. Holzwarth, T. Udem, T. W. Hänsch. Measuring the frequency of light with mode-locked lasers. *Opt. Commun.* **172**, 59-68 (1999).
90. H. R. Telle, G. Steinmeyer, A. E. Dunlop, J. Stenger, D. H. Sutter *et al.* Carrier-envelope offset phase control: A novel concept for absolute optical frequency control and ultrashort pulse generation. *Appl. Phys. B* **69**, 327-332 (1999).
91. A. Apolonski, A. Poppe, G. Tempea, C. Spielmann, T. Udem *et al.* Controlling the Phase Evolution of Few-Cycle Light Pulses. *Phys. Rev. Lett.* **85**, 740-743 (2000).
92. T. M. Fortier, J. Ye, S. T. Cundiff, R. S. Windeler. Nonlinear phase noise generated in air-silica microstructure fiber and its effect on carrier-envelope phase. *Opt. Lett.* **27**, 445-447 (2002).
93. O. D. Mücke, T. Tritschler, M. Wegener, U. Morgner, F. X. Kärtner. Determining the carrier-envelope offset frequency of 5-fs pulses with extreme nonlinear optics in ZnO. *Opt. Lett.* **27**, 2127-2129 (2002).
94. M. Zimmermann, C. Gohle, R. Holzwarth, T. Udem, T. W. Hänsch. Optical clockwork with an offset-free difference-frequency comb: accuracy of sum- and difference-frequency generation. *Opt. Lett.* **29**, 310-312 (2004).
95. T. Fuji, A. Apolonski, F. Krausz. Self-stabilization of carrier-envelope offset phase by use of difference-frequency generation. *Opt. Lett.* **29**, 632-634 (2004).
96. K. Wu. Personal communication (HC Photonics Corp., Hsinchu, Taiwan, May 3, 2005).
97. T. M. Fortier, D. J. Jones, J. Ye, S. T. Cundiff, R. S. Windeler. Long-term carrier-envelope phase coherence. *Opt. Lett.* **27**, 1436-1438 (2002).
98. S. Witte, R. T. Zinkstok, W. Hogervorst, K. S. E. Eikema. Control and precise measurement of carrier-envelope phase dynamics. *Appl. Phys. B* **78**, 5-12 (2004).
99. T. Pliska, N. Matuschek, S. Mohrdiek, A. Hardy, C. Harder. External feedback optimization by means of polarization control in fiber Bragg grating stabilized 980-nm pump lasers. *IEEE Phot. Tech. Lett.* **13**, 1061-1063 (2001).
100. R. Adler. A Study of Locking Phenomena in Oscillators. *Proc. IRE* **34**, 351-357 (1946).

-
101. A. E. Siegman, *Lasers* (University Science Books, Mill Valley, CA, 1986).
 102. D. W. Allan. Statistics of Atomic Frequency Standards. *Proc. IEEE* **54**, 221-231 (1966).
 103. F. W. Helbing, G. Steinmeyer, U. Keller. Carrier-Envelope Offset Phase-Locking With Attosecond Timing Jitter. *IEEE J. Sel. Top. Quantum Electron.* **9**, 1030-1040 (2003).
 104. F. W. Helbing, G. Steinmeyer, J. Stenger, H. R. Telle, U. Keller. Carrier-envelope-offset dynamics and stabilization of femtosecond pulses. *Appl. Phys. B* **74**, S35-S42 (2002).
 105. T. M. Fortier, D. J. Jones, J. Ye, S. T. Cundiff. Highly Phase Stable Mode-Locked Lasers. *IEEE J. Sel. Top. Quantum Electron.* **9**, 1002-1010 (2003).
 106. A. Sennaroglu, J. G. Fujimoto. Design criteria for Herriott-type multi-pass cavities for ultrashort pulse lasers. *Opt. Express* **11**, 1106-1113 (2003).
 107. A. M. Kowalewicz, A. T. Zare, F. X. Kärtner, J. G. Fujimoto, S. Dewald *et al.* Generation of 150-nJ pulses from a multiple-pass cavity Kerr-lens mode-locked Ti:Al₂O₃ oscillator. *Opt. Lett.* **28**, 1597-1599 (2003).
 108. S. H. Cho, F. X. Kärtner, U. Morgner, E. P. Ippen, J. G. Fujimoto *et al.* Generation of 90-nJ pulses with a 4-MHz repetition-rate Kerr-lens mode-locked Ti:Al₂O₃ laser operating with net positive and negative intracavity dispersion. *Opt. Lett.* **26**, 560-562 (2001).
 109. A. Fernández, T. Fuji, A. Poppe, A. Fürbach, F. Krausz *et al.* Chirped-pulse oscillators: a route to high-power femtosecond pulses without external amplification. *Opt. Lett.* **29**, 1366-1368 (2004).
 110. S. Naumov, A. Fernández, R. Graf, P. Dombi, A. Apolonski. Approaching the microjoule frontier with femtosecond laser oscillators. *New J. Phys.* **7**, 216 (2005).
 111. V. L. Kalashnikov, E. Podivilov, A. Chernykh, S. Naumov, A. Fernández *et al.* Approaching the microjoule frontier with femtosecond laser oscillators: theory and comparison with experiment. *New J. Phys.* **7**, 217 (2005).
 112. S. Dewald, T. Lang, C. D. Schröter, R. Moshhammer, J. Ullrich *et al.* Ionization of noble gases with pulses directly from a laser oscillator. *Opt. Lett.* **31**, 2072-2074 (2006).
 113. B. Ripley. Personal communication (Crystal Systems Inc., Salem, MA, USA, Jan 20, 2006).
 114. M. Zavelani-Rossi, F. Lindner, C. Le Blanc, G. Chériaux, J.-P. Chambaret. Control of thermal effects for high-intensity Ti:sapphire laser chains. *Appl. Phys. B* **70**, S193-S196 (2000).
 115. M. G. Holland. Thermal Conductivity of Several Optical Maser Materials. *J. Appl. Phys.* **33**, 2910-2911 (1962).
 116. A. C. Defranzo, B. G. Pazol. Index of refraction measurements on sapphire at low temperatures and visible wavelengths. *Appl. Opt.* **32**, 2224-2234 (1993).
 117. R. Huber, F. Adler, A. Leitenstorfer, M. Beutter, P. Baum *et al.* 12-fs pulses from a continuous-wave-pumped 200-nJ Ti:sapphire amplifier at a variable repetition rate as high as 4 MHz. *Opt. Lett.* **28**, 2118-2120 (2003).

118. E. Fill, L. Veisz, A. Apolonski, F. Krausz. Sub-fs electron pulses for ultrafast electron diffraction. *New J. Phys.* **8**, 272 (2006).
119. R. Graf, A. Fernández, M. Dubov, H. J. Brückner, B. N. Chichkov *et al.* Pearl-chain waveguides written at megahertz repetition rate. *Appl. Phys. B* **87**, 21-27 (2007).
120. A. Dubietis, G. Jonušauskas, A. Piskarskas. Powerful femtosecond pulse generation by chirped and stretched pulse parametric amplification in BBO crystal. *Opt. Commun.* **88**, 437-440 (1992).
121. N. Ishii, L. Turi, V. S. Yakovlev, T. Fuji, F. Krausz *et al.* Multimillijoule chirped parametric amplification of few-cycle pulses. *Opt. Lett.* **30**, 567-569 (2005).
122. D. Strickland, G. Mourou. Compression of amplified chirped optical pulses. *Opt. Commun.* **56**, 219-221 (1985).
123. M. Hentschel, R. Kienberger, C. Spielmann, G. A. Reider, N. Milosevic *et al.* Attosecond metrology. *Nature* **414**, 509-513 (2001).
124. M. Hentschel, Z. Cheng, F. Krausz, C. Spielmann. Generation of 0.1-TW optical pulses with a single-stage Ti:sapphire amplifier at a 1-kHz repetition rate. *Appl. Phys. B* **70**, S161-S164 (2000).
125. S. Sartania, Z. Cheng, M. Lenzner, G. Tempea, C. Spielmann *et al.* Generation of 0.1-TW 5-fs optical pulses at a 1-kHz repetition rate. *Opt. Lett.* **22**, 1562-1564 (1997).
126. M. Nisoli, S. Stagira, S. De Silvestri, O. Svelto, S. Sartania *et al.* A novel-high energy pulse compression system: generation of multigigawatt sub-5-fs pulses. *Appl. Phys. B* **65**, 189-196 (1997).
127. M. Mohebbi, R. Fedosejevs, V. Gopal, J. A. Harrington. Silver-coated hollow-glass waveguide for applications at 800 nm. *Appl. Opt.* **41**, 7031-7035 (2002).
128. M. Mohebbi. Personal communication (University of Alberta, Calgary, Canada, Apr 9, 2004).
129. Y. Abe, Y.-W. Shi, Y. Matsuura, M. Miyagi. Flexible small-bore hollow fibers with an inner polymer coating. *Opt. Lett.* **25**, 150-152 (2000).
130. Y. Matsuura, M. Miyagi, K. Shihoyama, M. Kawachi. Delivery of femtosecond pulses by flexible hollow fibers. *J. Appl. Phys.* **91**, 887-889 (2002).
131. Y. Matsuura. Personal communication (Tohoku University, Sendai, Japan, Jan 25, 2006).
132. M. Takeda, H. Ina, S. Kobayashi. Fourier-transform method of fringe-pattern analysis for computer-based topography and interferometry. *J. Opt. Soc. Am.* **72**, 156- (1982).
133. R. T. Zinkstok, S. Witte, W. Hogervorst, K. S. E. Eikema. High-power parametric amplification of 11.8-fs laser pulses with carrier-envelope phase control. *Opt. Lett.* **30**, 78-80 (2005).
134. C. Corsi, M. Bellini. Robustness of phase coherence against amplification in a flashlamp-pumped multi-pass femtosecond laser. *Appl. Phys. B* **78**, 31-34 (2004).
135. A. Ishizawa, H. Nakano, Carrier-envelope phase fluctuations of amplified laser pulses transmitted through neon-filled hollow fiber for pulse compression, in *Ultrafast Phenomena XIV, Proceedings of the 14th International Conference, Niigata, Japan, July 25-30, 2004* T. Kobayashi, T. Okada, T. Kobayashi, K. A. Nelson, S. De Silvestri, Eds. (Springer Verlag, 2005).
136. E. Goulielmakis, M. Uiberacker, R. Kienberger, A. Baltuška, V. S. Yakovlev *et al.* Direct Measurement of Light Waves. *Science* **305**, 1267-1269 (2004).
137. E. S. Polzik, H. J. Kimble. Frequency doubling with KNbO₃ in an external cavity. *Opt. Lett.* **16**, 1400-1402 (1991).

-
138. V. P. Yanovsky, F. W. Wise. Frequency doubling of 100-fs pulses with 50% efficiency by using a resonant enhancement cavity. *Opt. Lett.* **19**, 1952-1954 (1994).
139. M. Watanabe, R. Ohmukai, K. Hayasaka, H. Imajo, S. Urabe. High-power second-harmonic generation with picosecond and hundreds-of-picosecond pulses of a cw mode-locked Ti:sapphire laser. *Opt. Lett.* **19**, 637-639 (1994).
140. M. A. Persaud, J. M. Tolchard, A. I. Ferguson. Efficient generation of picosecond pulses at 243 nm. *IEEE J. Quantum Electron.* **27**, 1253-1258 (1990).
141. T.-M. Liu, C.-T. Yu, C.-K. Sun. 2 GHz repetition-rate femtosecond blue sources by second harmonic generation in a resonantly enhanced cavity. *Appl. Phys. Lett.* **86**, 061112 (2005).
142. G. McConnell, A. I. Ferguson, N. Langford. Cavity-augmented frequency tripling of a continuous wave mode-locked laser. *J. Phys. D* **34**, 2408-2413 (2001).
143. G. P. Agrawal, *Nonlinear Fiber Optics* (Academic Press, Boston, MA, USA, 2001).
144. V. L. Kalashnikov, C. Gohle, T. Udem. Femtosecond pulse enhancement in a passive external resonator. *in preparation* (2006).
145. J. Petersen, A. Luiten. Short pulses in optical resonators. *Opt. Express* **11**, 2975 (2003).
146. I. H. Malitson. Refraction and dispersion of synthetic sapphire. *J. Opt. Soc. Am.* **52**, 1377-1379 (1962).
147. A. O'Keefe, D. A. G. Deacon. Cavity ring-down optical spectrometer for absorption measurements using pulsed laser sources. *Rev. Sci. Instr.* **59**, 2544-2551 (1988).
148. K. An, C. Yang, R. R. Dasari, M. S. Feld. Cavity ring-down technique and its application to the measurement of ultraslow velocities. *Opt. Lett.* **20**, 1068-1070 (1995).
149. T. W. Hänsch, B. Couillaud. Laser Frequency Stabilization by Polarization Spectroscopy of a Reference Cavity. *Opt. Commun.* **35**, 441-444 (1980).
150. R. W. P. Drever, J. L. Hall, F. V. Kowalski. Laser Phase and Frequency Stabilization Using an Optical Resonator. *Appl. Phys. B* **31**, 97-105 (1983).
151. H. Kogelnik, T. Li. Laser beams and resonators. *Proc. IEEE* **54**, 1312 (1966).
152. V. L. Kalashnikov, C. Gohle, T. Udem, Maximization of Ultrashort Pulse Power Stored in a Passive Resonator Synchronously Pumped by a Femtosecond Oscillator, in *Advanced Solid-State Photonics, Technical Digest, paper MB2*. (Optical Society of America, Washington, DC, USA, 2005).
153. F. Ouellette, M. Piché. Ultrashort pulse reshaping with a nonlinear Fabry-Perot cavity matched to a train of short pulses. *J. Opt. Soc. Am. B* **5**, 1228-1236 (1988).
154. T. W. Hänsch. Einstein Lecture - Passion for precision. *Ann. Phys.* **15**, 627-652 (2006).
155. H. Schnatz, B. Lipphardt, J. Helmcke, F. Riehle, G. Zinner. First phase-coherent frequency measurement of visible radiation. *Phys. Rev. Lett.* **76**, 18-21 (1996).
156. T. Udem, S. A. Diddams, K. R. Vogel, C. W. Oates, E. A. Curtis *et al.* Absolute Frequency Measurements of the Hg⁺ and Ca Optical Clock Transitions with a Femtosecond Laser. *Phys. Rev. Lett.* **86**, 4996-4999 (2001).
157. J. Von Zanthier, T. Becker, M. Eichenseer, A. M. Nevsky, C. Schwedes *et al.* Absolute frequency measurement of the In⁺ clock transition with a mode-locked laser. *Opt. Lett.* **25**, 1729-1731 (2000).
158. A. Marian, M. C. Stowe, J. R. Lawall, D. Felinto, J. Ye. United Time-Frequency Spectroscopy for Dynamics and Global Structure. *Science* **306**, 2063-2068 (2004).

159. P. Fendel, S. D. Bergeson, T. Udem, T. W. Hänsch. Two-photon frequency comb spectroscopy of the 6s-8s transition in cesium. *Opt. Lett.* **32**, 701-703 (2007).
160. S. A. Diddams, J. C. Bergquist, S. R. Jefferts, C. W. Oates. Standards of Time and Frequency at the Outset of the 21st Century. *Science* **306**, 1318-1324 (2004).
161. P. Corkum. Plasma perspective on strong-field multiphoton ionization. *Phys. Rev. Lett.* **71**, 1994-1997 (1993).
162. M. Lewenstein, P. Balcou, M. Y. Ivanov, A. L'Huillier, P. Corkum. Theory of high-harmonic generation by low-frequency laser fields. *Phys. Rev. A* **49**, 2117-2132 (1994).
163. L. V. Keldysh. Ionization in field of a strong electromagnetic wave. *Soviet Physics JETP* **20**, 1307-1314 (1965).
164. L. G. Gouy. Sur une propriété nouvelle des ondes lumineuses. *Compt. Rendus Acad. Sci. Paris* **110**, 1251 (1890).
165. C. G. Durfee, A. R. Rundquist, S. Backus, C. Herne, M. M. Murnane *et al.* Phase matching of high-order harmonics in hollow waveguides. *Phys. Rev. Lett.* **83**, 2187-2190 (1999).
166. P. A. Hawley. Personal communication (Paonia, CO, USA, Feb 18, 2003).
167. A. Tarasevitch, A. Orisch, D. Von Der Linde, P. Balcou, G. Rey *et al.* Generation of high-order spatially coherent harmonics from solid targets by femtosecond laser pulses. *Phys. Rev. A* **62**, 023816 (2000).
168. R. Lichters, J. Meyer-Ter-Vehn, A. Pukhov. Short-pulse laser harmonics from oscillating plasma surfaces driven at relativistic intensity. *Phys. Plasmas* **3**, 3425-3437 (1996).
169. A. N. Belsky, H. Bachau, J. Gaudin, G. Geoffroy, S. Guizard *et al.* Observation of high energy photoelectrons from solids at moderate laser intensity. *Appl. Phys. B* **78**, 989-994 (2004).
170. E. Saczuk, J. Z. Kaminski. High-Order Harmonic Generation from Solid Surfaces in Intense Laser Fields. *Las. Phys.* **17**, 113-116 (2007).
171. F. H. M. Faisal, J. Z. Kaminski, E. Saczuk. Photoemission and high-order harmonic generation from solid surfaces in intense laser fields. *Phys. Rev. A* **72**, 023412 (2005).
172. R. B. Laughlin. Optical absorption edge of SiO₂. *Phys. Rev. B* **22**, 3021-3029 (1980).
173. S. Frank, N. Malinowski, F. Tast, M. Heinebrodt, I. M. L. Billas *et al.* Photoabsorption and ionization energies of nonstoichiometric CsI clusters: Metallization of a salt. *J. Chem. Phys.* **106**, 6217-6221 (1997).
174. The Center for X-Ray Optics at the Lawrence Berkeley National Laboratory; <http://www-cxro.lbl.gov/>
175. D. Von Der Linde, H. Schüler. Breakdown threshold and plasma formation in femtosecond laser–solid interaction. *J. Opt. Soc. Am. B* **13**, 216-222 (1996).
176. M. Lenzner, J. Krüger, S. Sartania, Z. Cheng, C. Spielmann *et al.* Femtosecond Optical Breakdown in Dielectrics. *Phys. Rev. Lett.* **80**, 4076-4079 (1998).
177. K. Z. Hatsagortsyan, C. H. Keitel. Phase-matched high-harmonic generation from laser-driven crystals. *Journal of Physics B* **35**, L175-L180 (2002).
178. K. D. Moll, R. J. Jones, J. Ye. Output coupling methods for cavity-based high-harmonic generation. *Opt. Express* **14**, 8189-8197 (2006).
179. P. Jaeglé, *Coherent Sources of XUV Radiation* (Springer Verlag, Berlin, 2005).
180. P. Agostini, F. Fabre, G. Mainfray, G. Petite, N. K. Rahman. Free-Free Transitions Following Six-Photon Ionization of Xenon Atoms. *Phys. Rev. Lett.* **42**, 1127-1130 (1979).

-
181. D. B. Milošević, G. G. Paulus, D. Bauer, W. Becker. Above-threshold ionization by few-cycle pulses. *J. Phys. B* **39**, R203-R262 (2006).
 182. G. G. Paulus, W. Becker, H. Walther. Classical rescattering effects in two-color above-threshold ionization. *Phys. Rev. A* **52**, 4043-4053 (1995).
 183. F. Lindner, M. G. Schätzel, H. Walther, A. Baltuška, E. Goulielmakis *et al.* Attosecond Double-Slit Experiment. *Phys. Rev. Lett.* **95**, 040401 (2005).
 184. D. B. Milošević, G. G. Paulus, W. Becker. High-order above-threshold ionization with few-cycle pulse: a meter of the absolute phase. *Opt. Express* **11**, 1418-1429 (2003).
 185. G. G. Paulus, F. Lindner, H. Walther, A. Baltuška, E. Goulielmakis *et al.* Measurement of the Phase of Few-Cycle Laser Pulses. *Phys. Rev. Lett.* **91**, 253004 (2003).
 186. C. A. Haworth, L. E. Chipperfield, J. S. Robinson, P. L. Knight, J. P. Marangos *et al.* Half-cycle cutoffs in harmonic spectra and robust carrier-envelope phase retrieval. *Nature Physics* **3**, 52-57 (2007).
 187. M. Wickenhauser, X. M. Tong, C. D. Lin. Laser-induced substructures in above-threshold-ionization spectra from intense few-cycle laser pulses. *Phys. Rev. A* **73**, 011401 (2006).
 188. A. T. J. B. Eppink, D. H. Parker. Velocity map imaging of ions and electrons using electrostatic lenses: Application in photoelectron and photofragment ion imaging of molecular oxygen. *Rev. Sci. Instr.* **68**, 3477-3484 (1997).
 189. K. Nicklaus, D. Hoffmann, M. Hofer, J. Luttmann, R. Poprawe, MOPA with kW Average Power and Multi MW Pulse Power, in *Advanced Solid-State Photonics, Technical Digest, paper MA2*. (Optical Society of America, Washington, DC, USA, 2005).
 190. F. Röser, J. Rothhardt, C. Bruchmann, T. Schreiber, A. Liem *et al.*, 60-fs Pulses with 1 μ J Pulse Energy Generated by Nonlinear Compression of a Short-Pulse Fiber Laser, in *Advanced Solid-State Photonics, Technical Digest, paper ME5*. (Optical Society of America, Washington, DC, USA, 2006).
 191. F. Röser, J. Rothhardt, T. Schreiber, J. Limpert, A. Tünnermann, 50W, 50fs pulses from a fiber laser system using nonlinear fiber compression, in *Proceedings of Photonics West*. (SPIE Press, San Jose, CA, USA, 2006).
 192. M. Herrmann, T. Udem, C. Gohle, N. Kolachevsky, T. W. Hänsch *et al.* The 1S–2S transition in singly ionized helium: Feasibility of high precision spectroscopy in the XUV. *in preparation* (2007).
 193. T. Weber, H. Giessen, M. Weckenbrock, G. Urbasch, A. Staudte *et al.* Correlated electron emission in multiphoton double ionization. *Nature* **405**, 658-661 (2000).

Acknowledgements

Although being almost the last page, this is probably the one most often read. My apologies go to those whose names were left out unintentionally.

First of all, I would like to thank Prof. Ferenc Krausz for giving me the marvelous chance to work in his group. He manages to pair a constant flow of new ideas with the liberty to pursue research in an independent manner. Not to be forgotten the excellent surrounding conditions.

Likewise, I am thankful to Prof. Theodor Hänsch for enabling the many great collaborations between the two groups, for continuous support of the enhancement cavity project and for accepting to be the second reviewer of this thesis.

A big thank-you goes to the members of the two groups for the cooperative attitude and the excellent working atmosphere, in particular to:

Sasha Apolonski, Peter Fendel, Takao Fuji, Christoph Gohle, Eleftherios Goulielmakis, Roswitha Graf, Max Herrmann, Reinhard Kienberger, Matthias Kling, Karl Linner, Tom Metzger, Sergei Naumov, Akira Ozawa, Karl Schmid, Martin Schultze (“für die erste Hälfte”), Wolfgang Simon, Franz Tavella, Thomas Udem, ...

I owe an extra thank-you to Christoph Gohle who continues to baffle me on a regular basis with his kindness and his knowledge of the most far-flung aspects of physics.

For the kind reception during the weeks I spent at their labs in 2004 and in general for the great collaboration I am grateful to the team at Femtolasers:

Harald Frei, Mike Hentschel, Andreas Iseman, Tuan Le, Andreas Stingl, Gabriel Tempea, Alfred Tomasch, Christian Warmuth.

A stipend of the FULMINA project in the framework of the FEMTONIK initiative of the Federal Ministry of Economics and Technology (BMWi) is gratefully acknowledged.

Last but not least, I would like to thank my family for always having provided appropriate nature and nurture.

Curriculum Vitæ

Graduate student in the group of Prof. F. Krausz at Max-Planck-Institute of Quantum Optics, Garching, Germany and Photonics Institute, Vienna University of Technology, Vienna, Austria	June 2003 – present
Diploma thesis in the group of Prof. S. T. Cundiff at JILA, University of Colorado, Boulder, USA Subject: “ <i>Phase-locking of an Erbium-doped fiber laser to a femtosecond Ti:Sapphire laser</i> ”	March – Aug. 2002
Working student at Nortel Networks GmbH, R&D – Advanced Applications, Zurich, Switzerland Subject: “ <i>Characterization of Fiber Bragg Gratings for the stabilization of 980nm pump lasers</i> ”	Feb. – July 2001
Internship at Bosch Telecom GmbH, R&D – Optical Terminals, Backnang, Germany Subject: “ <i>Investigation of the noise properties of a monolithic Nd:YAG ring-laser</i> ”	July 2000
Internship at SITA S.A., Technical Management, Paris, France Subject: “ <i>Analysis of the cost and reliability of the existing machines in the company</i> ”	July 1999
Undergraduate studies in physics at Swiss Federal Institute of Technology (ETH), Zurich, Switzerland	Oct. 1998 – March 2003
Social Service obligation at Institute for Aquatic Environmental Engineering, University of Karlsruhe, Germany	July 1997 – July 1998
High school in Mannheim, Germany	Aug. 1989 – June 1997
Date of Birth	1. Dec. 1977

Publications

M. Uiberacker, T. Uphues, M. Schultze, A.-J. Verhoef, V. S. Yakovlev, M. F. Kling, J. Rauschenberger, N. M. Kabachnik, H. Schröder, M. Lezius, K. L. Kompa, H.-G. Muller, M. J. J. Vrakking, S. Hendel, U. Kleineberg, U. Heinzmann, M. Drescher, F. Krausz. Attosecond real-time observation of electron tunnelling in atoms. *Nature* **446**, 627-632 (2007).

J. Rauschenberger, T. Fuji, M. Hentschel, A.-J. Verhoef, T. Udem, C. Gohle, T. W. Hänsch, F. Krausz. Carrier-envelope phase-stabilized amplifier system. *Laser Phys. Lett.* **3**, 37-42 (2006).

T. Metzger, J. Rauschenberger, A. Apolonski, K. Schmid, A. Baltuška, F. Krausz. Ultrakurze Laserpulse. *Laser Technik Journal* **4**, 27-33 (2005).

C. Gohle, J. Rauschenberger, T. Fuji, T. Udem, A. Apolonski, F. Krausz, T. W. Hänsch. Carrier envelope phase noise in stabilized amplifier systems. *Opt. Lett.* **30**, 2487-2489 (2005).

C. Gohle, T. Udem, M. Herrmann, J. Rauschenberger, R. Holzwarth, H. A. Schuessler, F. Krausz, T. W. Hänsch. A frequency comb in the extreme ultraviolet. *Nature* **436**, 234-237 (2005).

T. Fuji, J. Rauschenberger, C. Gohle, A. Apolonski, T. Udem, V. S. Yakovlev, G. Tempea, T. W. Hänsch, F. Krausz. Attosecond control of optical waveforms. *New J. Phys.* **7**, 116 (2005) (selected New J. Phys. Highlights of 2005).

T. Fuji, J. Rauschenberger, A. Apolonski, V. S. Yakovlev, G. Tempea, T. Udem, C. Gohle, T. W. Hänsch, W. Lehnert, M. Scherer, F. Krausz. Monolithic carrier-envelope phase-stabilization scheme. *Opt. Lett.* **30**, 332-334 (2005).

J. Rauschenberger, T. M. Fortier, D. J. Jones, J. Ye, and S. T. Cundiff. Control of the frequency comb from a modelocked Erbium-doped fiber laser. *Opt. Express* **10**, 1404-1410 (2002) (echoed in: Fiber Laser Shows Promise for Metrology. *Photonics Spectra*, Feb. 2003, p. 102).

Conference contributions

J. Rauschenberger, C. Gohle, A. Ozawa, T. Fuji, T. Udem, A. Apolonski, R. Graf, A. Fernández, B. Stein, V. Pervak, F. Krausz, T. W. Hänsch. Frequency combs and enhancement cavities. Winter Colloquium on the Physics of Quantum Electronics, Snowbird, USA, 2007 (plenary).

J. Rauschenberger, A. Ozawa, C. Gohle, B. Stein, R. Graf, A. Fernández, A. Apolonski, T. Udem, F. Krausz, T. W. Hänsch. Enhancement resonators for frequency combs. IEEE Lasers & Electro-Optics Society Annual Meeting, Montréal, Canada, 2006.

J. Rauschenberger, T. Fuji, T. Udem, C. Gohle, T. W. Hänsch, F. Krausz. Monolithic device for carrier-envelope phase stabilization. Laser Physics Workshop, Kyoto, Japan, 2005 (invited).

J. Rauschenberger, T. Fuji, A. J. Verhoef, T. Udem, C. Gohle, V. S. Yakovlev, G. Tempea, C. Warmuth, T. W. Hänsch, F. Krausz. Carrier-envelope phase-stabilized high-power amplifier system. Conference on Lasers and Electro-Optics, Munich, Germany, 2005.

J. Rauschenberger, T. Fuji, A. Apolonski, T. Udem, C. Gohle, V. S. Yakovlev, G. Tempea, C. Warmuth, T. W. Hänsch, F. Krausz. Compact phase-stabilization scheme for chirped-pulse amplifiers. International Conference on Ultrahigh Intensity Lasers, Tahoe City, USA, 2004.

J. Rauschenberger, D. J. Jones, T. M. Fortier, S. T. Cundiff, R. S. Windeler. Absolute frequency comb spanning 1530 to 1570 nanometers. DPG Spring Meeting, Hanover, Germany, 2003.

J. Rauschenberger, D. J. Jones, T. M. Fortier, S. T. Cundiff, R. S. Windeler. Absolute frequency comb spanning 1530 to 1570 nanometers. OSA Annual Meeting, Orlando, USA, 2002.